

การขึ้นรูปวัสดุอิเล็กทรอนิกส์สำหรับเซลล์เชื้อเพลิงออกไซด์ของแข็งโดยเทคนิคการหล่อแผ่นบาง



นางสาวปัทมาภรณ์ ธิมากุล

สถาบันวิทยบริการ

วิทยานิพนธ์นี้เป็นส่วนหนึ่งของการศึกษาตามหลักสูตรปริญญาวิทยาศาสตรมหาบัณฑิต

สาขาวิชาเทคโนโลยีเซรามิก ภาควิชาวัสดุศาสตร์

คณะวิทยาศาสตร์ จุฬาลงกรณ์มหาวิทยาลัย

ปีการศึกษา 2547

ISBN 974-17-6223-2

ลิขสิทธิ์ของจุฬาลงกรณ์มหาวิทยาลัย

FABRICATION OF ELECTROLYTE MATERIALS FOR SOLID OXIDE FUEL CELLS  
BY TAPE-CASTING TECHNIQUE

Miss Patthamaporn Timakul

A Thesis Submitted in Partial Fulfillment of the Requirements  
for the Degree of Master of Science in Ceramic Technology  
Department of Materials Science

Faculty of Science

Chulalongkorn University

Academic Year 2004

ISBN 974-17-6223-2



ปัตมาภรณ์ ธิมากุล : การขึ้นรูปวัสดุอิเล็กโทรไลต์สำหรับเซลล์เชื้อเพลิงออกไซด์ของแข็งโดยเทคนิคการหล่อแผ่นบาง. (FABRICATION OF ELECTROLYTE MATERIALS FOR SOLID OXIDE FUEL CELLS BY TAPE-CASTING TECHNIQUE) อ. ที่ปรึกษา : รศ.ดร.สุพัตรา จินาวัดณ์, อ. ที่ปรึกษาร่วม : ดร.ภาวดี อังค์วัฒนะ, 100 หน้า. ISBN 974-17-6223-2.

งานวิจัยนี้มุ่งเน้นศึกษาและพัฒนาวัสดุอิเล็กโทรไลต์สำหรับเซลล์เชื้อเพลิงออกไซด์ของแข็ง โดยสนใจวัสดุ YSZ ที่มีปริมาณของ  $Y_2O_3$  3, 8 และ 10 โมลเปอร์เซ็นต์ใน  $ZrO_2$  และศึกษาหาวัสดุอิเล็กโทรไลต์องค์ประกอบอื่น ๆ เช่น doped- $CeO_2$  ซึ่งมีแนวโน้มที่จะให้สมบัติที่ดีขึ้นโดยเฉพาะสมบัติทางการนำไฟฟ้าแบบไอออนิก (ionic conductivity) โดยใช้เทคนิคการขึ้นรูปแบบการหล่อแผ่นบาง จุดมุ่งหมายที่สำคัญอีกประการหนึ่งในงานวิจัยนี้คือการเตรียม slurry ของผงอิเล็กโทรไลต์โดยใช้น้ำเป็นตัวทำละลายซึ่งไม่เป็นพิษกับสิ่งแวดล้อม หลังจากทำการขึ้นรูปเทปอิเล็กโทรไลต์ได้แล้ว จะศึกษาคุณสมบัติและเวลาในการเผาผนึกที่เหมาะสม และการตรวจสอบลักษณะเฉพาะของอิเล็กโทรไลต์ รวมถึงการศึกษาสมบัติทางไฟฟ้าและสมบัติเชิงกลของเทปเพื่อนำไปเป็นต้นแบบวัสดุอิเล็กโทรไลต์สำหรับผลิตเซลล์เชื้อเพลิงของแข็งและนำไปประกอบกับขั้วอิเล็กโทรดเป็นเซลล์สแตคสำหรับผลิตกระแสไฟฟ้าต่อไป จากการทดลองพบว่าวัสดุอิเล็กโทรไลต์ที่มีคุณสมบัติที่ดีที่สุดคืออิเล็กโทรไลต์ที่ขึ้นรูปจากผง  $ZrO_2$  ที่มีปริมาณการเติม  $Y_2O_3$  ที่ 8 โมลเปอร์เซ็นต์ โดยได้เทปอิเล็กโทรไลต์ ที่มีขนาดของเกรน  $0.5-1 \mu m$  และมีลักษณะโครงสร้างผลึกแบบลูกบาศก์ฟลูออไรท์ มีความหนาแน่น 98-99 เปอร์เซ็นต์ของความหนาแน่นทางทฤษฎี ค่าการนำไอออน  $30.11 \times 10^{-3} S/cm$  โดยค่าความแข็งแรงดัด (flexural strength) ของ 8-10 โมลเปอร์เซ็นต์ YSZ มีค่าตั้งแต่ 100-180 MPa และของ 3 โมลเปอร์เซ็นต์ YSZ มีค่าตั้งแต่ 400-680 MPa

ภาควิชาวัสดุศาสตร์  
สาขาวิชา เทคโนโลยีเซรามิก  
ปีการศึกษา 2547

ลายมือชื่อผู้ผลิต.....  
ลายมือชื่ออาจารย์ที่ปรึกษา.....  
ลายมือชื่ออาจารย์ที่ปรึกษาร่วม.....



## 4572631423 : MAJOR CERAMIC TECHNOLOGY

KEY WORD : ELECTROLYTE/ SOLID OXIDE FUEL CELL/ AQUEOUS TAPE-CASTING/  
IONIC CONDUCTIVITY

PATTHAMAPORN TIMAKUL : FABRICATION OF ELECTROLYTE MATERIALS FOR  
SOLID OXIDE FUEL CELLS BY TAPE-CASTING TECHNIQUE. THESIS ADVISOR :  
ASSOCIATE PROFESSOR SUPATRA JINAWATH, Ph.D., THEESIS CO-ADVISOR :  
PAVADEE AUNGKAVATTANA, Ph.D. 100 pp. ISBN 974-17-6223-2

In this research, solid oxide fuel cell electrolytes were fabricated by aqueous tape casting technique. The basic compositions for SOFC electrolyte systems were focussed on yttria-stabilized zirconia (YSZ) system and the preliminary investigations on the ceria-based system with  $Gd_2O_3$  addition was also performed. The powders used in this study were from different sources.  $ZrO_2$ -based system doped with 3, 8, and 10 mol% of  $Y_2O_3$  were used in this research work, and 8YSZ electrolyte tape illustrated the desirable properties. The grain size of the sintered electrolyte tapes was in the range of 0.5-1  $\mu m$  with 98-99% of theoretical density. Phase and crystal structure showed the pure cubic fluorite structure for 8-10 mol%  $Y_2O_3$  doped  $ZrO_2$  and tetragonal phase for 3 mol% doped. The electrolyte tapes sintered at 1450°C for 4 hours had the highest ionic conductivity of  $30.11 \times 10^{-3}$  S/cm. The flexural strengths were in the range of 100-180 MPa for 8-10 mol% YSZ, and 400-680 MPa for 3 mol% YSZ.

สถาบันวิทยบริการ  
จุฬาลงกรณ์มหาวิทยาลัย

Department of Materials Science  
Field of Study Ceramic Technology  
Academic year 2004

Student's signature.....  
Advisor's signature.....  
Co-advisor's signature.....

## Acknowledgements

I would like to express my sincere gratitude and appreciation to my advisor, Assoc. Prof. Dr. Supatra Jinawath, for her time, and invaluable advices. Special thanks are extended to my co-advisor Dr. Pavadee Aungkavattana, the senior researcher at National Metal and Materials Center (MTEC) for all of her precious contributions and suggestions as well as her patience in training me throughout the entire study. Moreover, I would like to express my thanks to all of my teachers at Chulalongkorn University.

I wish to thank each of my committee members, Assoc. Prof. Soawaroj Chuayjuljit, Prof. Dr. Shigetaka Wada, and Dr. Sirithan Jiemsirilers, for their valuable contributions and edit this manuscript. My appreciation also goes to MTEC for providing the financial support in research for the entire study. Furthermore, I would like to acknowledge the MTEC staffs for their sustained backing and helps.

Finally, I would like to express my loves and appreciation to my father, my mother and my family back in Surathani for their loves and encouragement. My loving appreciation is also to my late grandfather and grandmother.

สถาบันวิทยบริการ  
จุฬาลงกรณ์มหาวิทยาลัย

# Contents

	Page
Abstract (Thai).....	iv
Abstract (English).....	v
Acknowledgements.....	vi
Contents.....	vii
List of tables.....	x
List of figures.....	xi
Chapter 1 Introduction.....	1
Chapter 2 Literature Review.....	3
2.1 Introduction to fuel cells.....	3
2.2 Types of fuel cells.....	4
2.3 Fuel cell applications.....	7
2.4 Solid oxide fuel cells.....	7
2.4.1 Advantages of SOFCs.....	8
2.4.2 Basic principles govern SOFC design and operation.....	9
2.4.2.1 Electrolyte.....	10
2.4.2.2 Electrode.....	10
2.4.2.3 Interconnect.....	11
2.4.2.4 Materials for SOFC electrolyte component.....	12
2.5 Operating regimes and typical SOFC components.....	16
2.5.1 High temperature operating regime (>900°C).....	18
2.5.2 Intermediate temperature operating regime (700-900°C).....	19
2.5.3 Low temperature operating regime (450-700°C).....	19
2.6 Tape casting technique.....	20
2.6.1 Water-based tape casting.....	22
2.6.2 Slurry formation.....	22
2.6.2.1 Solvent.....	23
2.6.2.2 Ceramic powder.....	23
2.6.2.3 Polymer binder.....	24

## Contents (contd.)

	Page
2.6.2.4 Plasticizer.....	24
2.6.2.5 Dispersant.....	25
2.6.3 Rheology of tape casting slurries.....	25
2.7 Electrical conductivity.....	26
2.8 Thermal expansion coefficient.....	28
2.9 Mechanical property.....	28
2.10 Previous Research up-to-date (1997-2004).....	29
<b>Chapter 3 Experimental Work.....</b>	<b>31</b>
3.1 Powder preparation and characterization.....	31
3.2 Slurry preparation.....	32
3.3 Rheology of electrolyte slurry.....	34
3.4 Tape casting.....	35
3.5 De-binding and sintering conditions.....	36
3.6 Characterization techniques.....	37
3.6.1 Phase and crystal structure.....	37
3.6.2 Microstructural evaluation.....	37
3.6.3 Electrical measurement.....	37
3.6.4 Thermal expansion measurement.....	38
3.6.5 Mechanical property measurement.....	40
<b>Chapter 4 Results and Discussion.....</b>	<b>41</b>
4.1 Electrolyte powder characterizations.....	41
4.1.1 Particle size and particle size distribution.....	41
4.1.2 X-ray diffraction study.....	42
4.1.3 SEM study.....	46
4.2 Rheology of electrolyte slurry.....	48
4.3 Physical property of electrolyte green tape.....	51
4.4 Property and characterization of sintered electrolyte.....	52
4.4.1 Phase and crystal structure study by XRD.....	52

## Contents (contd.)

	Page
4.4.2 Microstructure evaluation.....	56
4.4.3 Electrical property measurement.....	70
4.4.3.1 Effect of dopants to electrical conductivity.....	75
4.4.3.2 Effect of sintering conditions to electrical conductivity.....	76
4.4.4 Mechanical property measurement.....	79
4.4.5 Thermal expansion measurement.....	81
<b>Chapter 5 Conclusions.....</b>	<b>84</b>
<b>Chapter 6 Future work.....</b>	<b>86</b>
<b>References.....</b>	<b>87</b>
<b>Appendices.....</b>	<b>90</b>
Appendix A.....	91
Appendix B.....	98
<b>Biography.....</b>	<b>100</b>

สถาบันวิทยบริการ  
จุฬาลงกรณ์มหาวิทยาลัย

## List of Tables

	Page
Table 2.1 Types of fuel cells and their features.....	5
Table 2.2 Conductivity data for Stabilized ZrO <sub>2</sub> doped with rare-earth oxides.....	15
Table 2.3. Ionic conductivity of doped CeO <sub>2</sub> .....	16
Table 2.4 Potential SOFC components at different operating temperatures.....	18
Table 2.5 Common plasticizers used in aqueous tape casting.....	24
Table 2.6 Selected dispersants for tape casting slurries.....	25
Table 2.7 Thermal expansion data for YSZ materials.....	28
Table 3.1 Types of powder and sources.....	31
Table 4.1 Particle size and size distribution of the starting powder.....	42
Table 4.2. Measurement of viscosity of electrolyte slurries by Brookfield viscometer.....	49
Table 4.3. Batches and physical appearance of the green tape.....	51
Table 4.4 The density and the relative density measured by Archimedes method.....	69
Table 4.5 Thermal expansion coefficients of the electrolyte samples at 1000°C.....	73
Table 4.6 The flexural strength of electrolyte sample at different sintering temperature.....	80
Table 4.7 Thermal expansion coefficients of the electrolyte samples at 1000°C.....	82

## List of Figures

	Page
Fig. 2.1 Schematic image of fuel cell principle.....	4
Fig. 2.2 Potential applications of the SOFC technology.....	9
Fig. 2.3 Solid oxide fuel cell designs.....	9
Fig. 2.4 Crystal structure of conducting oxides : fluorite structure, illustrated by stabilized zirconia by ceria.....	13
Fig. 2.5 Variation of dopant concentration on the ionic conductivity of stabilized $ZrO_2$ at Temperature of $807^\circ C$ .....	14
Fig. 2.6 Composition dependence of the electrical conductivity at $1000^\circ C$ for $ZrO_2-Ln_2O_3$ (Ln=lanthanide).....	14
Fig. 2.7 Perovskite structure, illustrated by oxygen ion conducting $LaGaO_3$ .....	17
Fig. 2.8 Diagrammatic view of a slurry layer is doctor bladed onto a substrate.....	20
Fig. 2.9 A flow chart illustrating the general production process of ceramic tape-based Components.....	21
Fig. 2.10 Equivalent circuit ( a ) and schematic complex impedance plot of polycrystalline ( b ).....	27
Fig. 3.1 The diagram of GDC powder preparation.....	34
Fig. 3.2 The step of electrolyte slurry preparation.....	36
Fig. 3.3 Tape caster head.....	37
Fig. 3.4 Tape casting machine with the electrolyte slurry casting.....	37
Fig. 3.5 A schematic diagram of de-binder and sintering programme.....	38
Fig. 3.6 A schematic diagram of control an measurement apparatus for the AC impedance Spectroscopy.....	39
Fig. 3.7 Preparation specimen for electrical measurement.....	40
Fig. 3.8 A flow chart of the repeat loop of electrolyte tape investigation.....	41
Fig. 4.1 XRD patterns of as-received 3YSZ powder (Tetragonal).....	43
Fig. 4.2 XRD patterns of as-received 8YSZ powder from various sources (cubic fluorite).....	43
Fig. 4.3 XRD patterns of as-received 10YSZ powders from various sources(cubic fluorite).....	44
Fig. 4.4 XRD pattern of as-received Ceria powders from Alfa Aesar (cubic fluorite).....	44
Fig. 4.5 XRD pattern of as-received GDC (10 mol%) powders from mixed-oxide route (cubic fluorite).....	45

## List of Figures (condt.)

	Page
Fig. 4.6 XRD pattern of as-received GDC (20 mol%)powders from mixed-oxide route (cubic fluorite).....	45
Fig. 4.7 SEM micrographs of as-received commercial powder ( a ) 3 mol%Y <sub>2</sub> O <sub>3</sub> doped Zr <sub>2</sub> O <sub>3</sub> from MEL, (b) 8 mol% Y <sub>2</sub> O <sub>3</sub> doped ZrO <sub>2</sub> from MEL, (c) 8 mol%Y <sub>2</sub> O <sub>3</sub> doped ZrO <sub>2</sub> from Tosoh, (d) 8 mol%Y <sub>2</sub> O <sub>3</sub> doped ZrO <sub>2</sub> from Daiichi, Japan.....	46
Fig. 4.8 SEM micrographs of as-received commercial powders for 10YSZ and Ceria and GDC 10-20 mol% (a) 10 mol%Y <sub>2</sub> O <sub>3</sub> doped ZrO <sub>2</sub> from MEL, (b) 10 mol%Y <sub>2</sub> O <sub>3</sub> doped ZrO <sub>2</sub> from Daiichi, (c) Ceria powder from Aesar, (d) GDC 10 mol% doped from mixed oxide route, (e) GDC 20 mol% doped from mixed-oxide route.....	47
Fig. 4.9 Rheology behaviors of the electrolyte slurries.....	49
Fig. 4.10 Flow characteristics of electrolyte slurries.....	50
Fig. 4.11 XRD pattern of 3YSZ (MEL) sintered electrolyte tape at 1400°C for 2 hrs.....	52
Fig.4.12 XRD patterns of 8YSZ and 10YSZ (MEL) sintered electrolyte tape at 1400°C for 2 hrs.....	53
Fig. 4.13 XRD pattern of ceria-based electrolyte pellets sintered at 1450°C for 1 hour.....	53
Fig. 4.14 XRD patterns of sintered electrolyte Po (obtained com.Tape) at 1400 and 1450°C for 2 hrs and 1450°C for 4 hrs.....	54
Fig. 4.15 XRD patterns of sintered electrolyte P13R (3YSZ, MEL) at 1400 and 1450°C for 2 hrs and 1450°C for 4 hrs.....	54
Fig. 4.16 XRD patterns of sintered electrolyte P19R (8YSZ, MEL) at 1400 and 1450°C for 2 hrs and 1450°C for 4 hrs.....	55
Fig. 4.17 XRD patterns of sintered electrolyte P29 (8YSZ + 3YSZ, MEL) at 1400 and 1450°C for 2 hrs and 1450°C for 4 hrs.....	55
Fig. 4.18 SEM micrographs of sintered tape of 3YSZ, MEL (P13) sintered at 1400°C, 2h; (a) at the surface, (b) fractured surface.....	56
Fig. 4.19 8YSZ, MEL (P19) compared with 8YSZ, Tosoh (P21); ( a ) and ( b ) are surface and fractured surface of 8YSZ, MEL; ( c ) and ( d ) are surface and fractured surface of 8YSZ, Tosoh.....	57



## List of Figures (condt.)

	Page
Fig. 4.20 10YSZ, MEL (P20) compared with 10YSZ, Daiichi (P9); ( a ) and ( b ) are surface and fractured surface of 10YSZ, MEL; ( c ) and ( d ) are surface and fractured surface of 10YSZ, Daiichi.....	58
Fig. 4.21 Ceria and GDC with 10 and 20 mol% doped pressed specimens sintered at 1450°C for 1 hour.....	59
Fig.4.22 SEM micrograph of P13R; 3YSZ (MEL) electrolyte tape (a) surface, (b) fractured surface sintered at 1400 °C for 2 hrs ;(c) surface, (d) fractured surface sintered at 1450 °C for 2 hrs ; (e) surface, (f) fractured surface sintered at 1450 °C for 4 hrs .....	62
Fig.4.23 SEM micrograph of Po(obtain.commercial.Tape) ; electrolyte tape (a) surface, (b) fractured surface sintered at 1400 °C for 2 hrs ;(c) surface, (d) fractured surface sintered at 1450 °C for 2 hrs ; (e) surface, (f) fractured surface sintered at 1450 °C for 4 hrs .....	63
Fig.4.24 SEM micrograph of P19R; 8YSZ (MEL) electrolyte tape (a) surface, (e) fractured surface sintered at 1400 °C for 2 hrs ;(c) surface, (f) fractured surface sintered at 1450 °C for 2 hrs ; (e) surface, (f) fractured surface sintered at 1450 °C for 4 hrs.....	64
Fig.4.25 SEM micrograph of P20R; 10YSZ (MEL) electrolyte tape (a) surface, (b) fractured surface sintered at 1400 °C for 2 hrs ;(c) surface, (g) fractured surface sintered at 1450 °C for 2 hrs ; (e) surface, (f) fractured surface sintered at 1450 °C for 4 hrs.....	65
Fig.4.26 SEM micrograph of P9R; 10YSZ (Daiichi) electrolyte tape (a) surface, (b) fractured surface sintered at 1400 °C for 2 hrs ;(c) surface, (c) fractured surface sintered at 1450 °C for 2 hrs ; (e) surface, (f) fractured surface sintered at 1450 °C for 4 hrs.....	66

## List of Figures (cond.)

	Page
Fig.4.27 SEM micrograph of P21R, 8YSZ (Tosoh) electrolyte tape (a) surface, (b) fractured surface sintered at $1400^{\circ}\text{C}$ for 2 hrs ;(c) surface, (d) fractured surface sintered at $1450^{\circ}\text{C}$ for 2 hrs ; (e) surface, (f) fractured surface sintered at $1450^{\circ}\text{C}$ for 4 hrs.....	67
Fig.4.28 SEM micrograph of P29 ( 3Y+ 8YSZ), MEL electrolyte tape (a) surface, (b) fractured surface sintered at $1400^{\circ}\text{C}$ for 2 hrs ;(c) surface, (c) fractured surface sintered at $1450^{\circ}\text{C}$ for 2 hrs ; (e) surface, (f) fractured surface sintered at $1450^{\circ}\text{C}$ for 4 hrs.....	68
Fig. 4.29 Examples of impedance spectra plots of P12 (10YSZ) electrolyte sintered at $1450^{\circ}\text{C}$ for 2 hr, recorded at $275^{\circ}$ , $400^{\circ}$ , and $600^{\circ}\text{C}$ in air.....	71
Fig.4.30 The Arrhenius plots of YSZ based electrolyte tapes after sintering at $1400^{\circ}\text{C}$ for 2 hrs.....	72
Fig.4.31 The Arrhenius plots of the 4 best formulations of YSZ based electrolyte tapes after sintering at $1400^{\circ}\text{C}$ for 2 hrs, comparing to the obtained commercial tape.....	74
Fig. 4.32 Arrhenius plots of YSZ electrolytes with various mol% of dopants.....	75
Fig. 4.33 Arrhenius plots of various ceria-based electrolytes in the function of effect of doping.....	76
Fig. 4.34 Arrhenius plots of the ionic conductivity for Po(obtain commercial tape) as the function of different sintering temperatures.....	77
Fig. 4.35 Arrhenius plots of the ionic conductivity for P19R (8Y, MEL) as the function of different sintering time.....	77
Fig. 4.36 Arrhenius plots of the ionic conductivity for P20R (10Y, MEL) as the function of different sintering temperature and time.....	78
Fig. 4.37 Arrhenius plots of the ionic conductivity for P9R (10Y, Daiichi) as the function of different sintering temperatures.....	78
Fig. 4.38 Arrhenius plots of the ionic conductivity for P21R (8YSZ, Tosoh) as the function of different sintering temperature.....	79

## List of Figures (condt.)

	Page
Fig. 4.39 The plot of the flexural strength of the sintered tapes at different temperature.....	81
Fig. 4.40 Thermal expansion coefficients of SOFC electrolyte materials at the temperature range of 50-1000°C (from various sources).....	82



สถาบันวิทยบริการ  
จุฬาลงกรณ์มหาวิทยาลัย

# Chapter 1

## Introduction

Each year, the total worldwide and per capita energy consumption increases. It has become essential to satisfy this demand, in a way that reduces environmental impact, uses fewer non renewable resources. For a growing number of power generators and users, fuel cells are the key to the nation's tomorrow power, offers the solution to some future power generating needs. For instance, fuel cells operate as stand alone units, produce clean power without excessive CO<sub>2</sub> emissions and minimal pollution.<sup>[1]</sup>

Fuel cell technology is being investigated for its potential use in transport and power generation applications in many countries in the world. Fuel cells have the capacity to supplant various conventional technologies with cleaner and more efficient systems.<sup>[1]</sup> They are categorized by their electrolytes, the alkaline, phosphoric acid and solid polymer types are all past the fundamental development stage and are being tested or used in commercial applications, though not necessarily on a fully cost-competitive basis.

The high temperature molten carbonate fuel cells (MCFCs) and solid oxide fuel cells (SOFCs) types seem better suited to power generation in a hydrocarbon fuel economy. However, at present, the costs of MCFCs and SOFCs are too high to compete directly with contemporary power generation plant.<sup>[1,2]</sup> In addition, previous investigations<sup>[1]</sup> stated clearly that MCFC experienced serious problems on major corrosion due to the corrosive molten salts when operated at high temperature for a long period of time. In the case of SOFC, the electrolyte consists of a solid ceramic oxide. The two-phase system characterizing SOFCs gives it a series of advantages, particularly compared to the three-phase high temperature MCFC and the phosphoric acid fuel cells (PAFC) which have a liquid electrolyte and solid electrodes. The solid electrolyte in SOFC eliminates most corrosion and liquid electrolyte management problem results in more compact cell design. The electrolyte is generally composed of yttria-stabilized zirconia (YSZ). Small amount of yttria was introduced to zirconia in order to transform the pure zirconia, an insulator, into an ion conductor. Oxygen ions move across this solid oxide electrolyte from

cathode to anode at high temperature, in contrast to the hydrogen and hydroxide ions as the charge carriers in the alkaline fuel cell (AFC), phosphoric acid fuel cell (PAFC), and proton-exchange membrane fuel cell (PEMFC) which moving from anode to cathode.

Conventionally, SOFCs operate at temperatures about 1000°C at which zirconia-based electrolyte configurations used are sufficiently conductive to oxide ions while remaining non-conductive to electrons.<sup>[2,3]</sup> Such this high operating temperature may enable fuels to be reformed directly inside the cells and simultaneously, allows fuels that contain relatively high levels of impurities to be used, such as natural gas, diesel oils, coal gas, biogas and other hydrocarbon-contained fuels (though these will require some pre-reforming).

The commercialization of fuel cells is being fostered by various trends currently impacting the marketplace, such as the deregulation of the electric utility industry, and the increasing desire on the part of utilities to avoid costly transmission, maintenance and distribution expenditures. Fuel cell system adoption will also be encouraged by the need for clean power generation.

Two main issues in SOFC development can be identified as driving forces during recent years: cost reduction with respect to low-cost materials and simpler processing techniques, as well as the improvement of durability in long-term operation.<sup>[4]</sup> For the environmental impact, and the lowering the manufacturing cost, the significance of this study is to be able to fabricate the SOFC electrolyte by water-based tape casting technique.

**The objectives of this thesis are as follows:**

1. To synthesize and fabricate various materials for electrolyte system in SOFC in order to obtain high electrical conductivity property.
2. To study the fabrication conditions, i.e. amount of binder, wetting ability of electrolyte materials by doctor-blade tape casting technique focusing on water-based system.
3. To optimize sintering conditions including temperature and time in order to obtain high density and high conductivity tapes and to characterize them.

## Chapter 2

### Literature Review

This chapter will outline the basic principle of fuel cell, particularly will focus on solid oxide fuel cell. More details will be on types of fuel cell, applications and benefits of fuel cells, fabrication technique to manufacture fuel cell components, i.e. tape casting method. At last, the chapter will summarize the previous studies on SOFCs fabrication and properties.

#### 2.1. Introduction to Fuel cells

The principle of fuel cell was first discovered in 1839 by Sir William R. Grove used a dilute sulfuric acid electrolyte, a hydrogen anode and oxygen cathode operated at room temperature.<sup>[5]</sup> A fuel cell is the energy conversion device that generates directly the electricity, utilizing an electrochemical reaction instead of a combustion process. Fuel cells are basically composed of two porous electrodes, one positive and one negative, so called the cathode and anode, sandwiched around an ion conducting electrolyte.<sup>[2,5]</sup>

The operating principles of fuel cells are similar to those of batteries. However, unlike a battery, a fuel cell does not run down or require recharging.<sup>[6]</sup> The reaction begins with the oxygen or air on the cathode side being ionized and generating negatively charged oxygen ions that flow through the cathode and across the electrolyte. At the anode side, the oxygen ion combines with a positively charged hydrogen ion that comes from a hydrocarbon fuel like hydrogen, natural gas, methanol or gasoline and releases an electron to the external circuit and back to the cathode. Fuel cell has no moving parts, therefore it produces little noise, and when fueled by pure hydrogen, there will be only heat and water as by-products.

Additionally, a single fuel cell generates a tiny amount of direct current electricity. In practice, many fuel cells are usually assembled into a stack will continue to produce electricity as long as there is a supply of fuel and air to the cells.

จุฬาลงกรณ์มหาวิทยาลัย

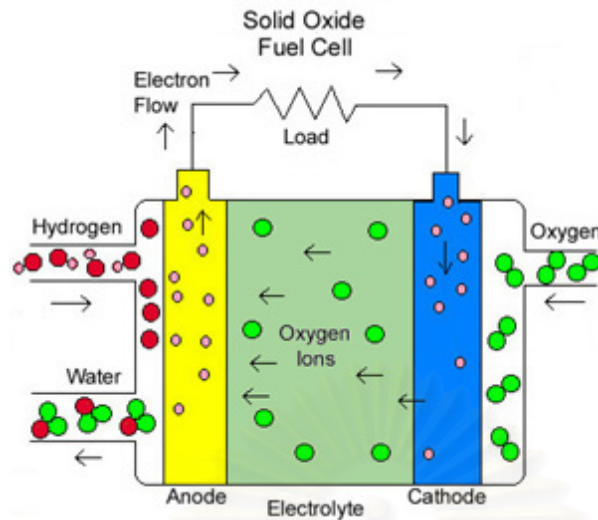
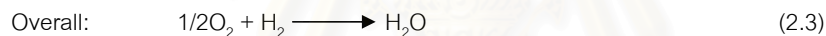
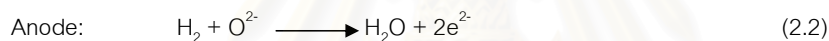
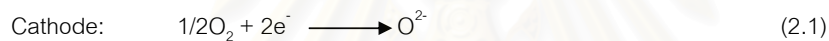


Fig. 2.1 Schematic image of fuel cell principle (after <http://www.iit.edu/>)

Fig. 2.1 shows the schematic of a fuel cell, comprised of an electrolyte, an anode and a cathode. The reactions in fuel cell system are:



## 2.2. Types of Fuel cells

Several different types of fuel cell have been developed after the invention of “gas battery” by Sir William R. Grove in 1839. There are five types of fuel cells, named for their electrolyte which defines the key properties, particularly operating temperature, so each type of fuel cell requires appropriate materials and is suitable for specific applications.<sup>[7]</sup> They are alkaline fuel cells (AFC), phosphoric acid fuel cells (PAFC), proton-exchange membrane fuel cells (PEMFC), molten carbonate fuel cells (MCFC), and solid oxide fuel cells (SOFC). Table 2.1 listed the important features of the four main types of fuel cells.<sup>[5]</sup>



Table 2.1 Types of fuel cells and their features <sup>[5]</sup>

Features	Fuel cell type			
Name	Polymer electrolyte	Phosphoric acid	Molten carbonate	Solid oxide
Electrolyte	Ion exchange membrane	Phosphoric acid	Alkali carbonate mixture	Yttria-stabilized zirconia
Operating temperature (°C)	70-90	180-220	650-700	800-1000
Charge carrier	H <sup>+</sup>	H <sup>+</sup>	CO <sub>3</sub> <sup>2-</sup>	O <sup>2-</sup>
Electrolyte state	Solid	Immobilized liquid	Immobilized liquid	Solid
Cell hardware	Carbon-or metal-based	Graphite-based	Stainless steel	Ceramic
Catalyst, anode	Platinum (Pt)	Platinum (Pt)	Nickel (Ni)	Nickel (Ni)
Fuels for cell	H <sub>2</sub>	H <sub>2</sub>	Reformate or CO/H <sub>2</sub>	Reformate or CO/H <sub>2</sub> or CH <sub>4</sub>
Reforming	External or direct MeOH	External	External or internal	
Feed for fuel processor	MeOH, natural gas, LPG, Gasoline, diesel	Natural gas, MeOH gasoline, diesel	Gas from coal or biomass, natural gas, gasoline	Gas from coal or biomass, natural gas, gasoline
Oxidant for cell	O <sub>2</sub> / air	O <sub>2</sub> / air	Co <sub>2</sub> / O <sub>2</sub> / air	O <sub>2</sub> / air
Co-generation heat	None	Low quality	High	High
Cell efficiency (%)	40-50	40-50	50-60	50-65
Electrical power	up to 250 kW	> 50 kW	> 1MW	up to 1 MW
Possible application	cars, buses, residential, energy supply	power stations	power stations	power stations

The various types of fuel cells, which were categorized by their electrolyte, represent quite different technologies with no clear winner yet. The alkaline phosphoric acid and polymer electrolyte types are now past the basic development stage and are being used in commercial applications, even though not necessarily on a fully cost-competitive basis. The remaining two principal types of fuel cell, the high temperature molten carbonate fuel cell (MCFC) and solid oxide fuel cell (SOFC) still require some stage of basic research and testing before the main problems will be resolved. However, a few of major MCFC test facility has already demonstrated and operated for some period of times in the U.S. and Europe.<sup>[8]</sup>

The high temperature MCFC and SOFC types seem better suited to power generation in a hydrocarbon fuel economy. However, at present, the costs of MCFCs and SOFCs are too high to compete directly with contemporary power generation plant.<sup>[8]</sup> In addition, previous investigations<sup>[9]</sup> stated clearly that MCFC experienced serious problems on major corrosion due to the corrosive molten salts when operated at high temperature for a long period of time.



In the case of SOFC, the electrolyte consists of a solid ceramic oxide. The solid electrolyte in SOFC eliminates most corrosion and liquid electrolyte management problem results in more compact cell design.<sup>[3,6]</sup> The electrolyte is generally composed of yttria-stabilized zirconia (YSZ). Small amount of yttria was introduced to zirconia in order to transform the pure zirconia, an insulator, into an ionic conductor. Oxygen ions move across this solid oxide electrolyte from cathode to anode at high temperature which is in contrast to the hydrogen and hydroxide ions acting as the charge carriers in the AFC, PAFC, and PEMFC and moving from anode to cathode. Conventionally, SOFCs operate at temperatures about 1000°C at which zirconia-based electrolyte configurations used are sufficiently conductive to oxide ions while remaining non-conductive to electrons.<sup>[10,11]</sup> Such this high operating temperature may enable fuel to be reformed directly inside the cells and simultaneously, allows fuels that contain relatively high levels of impurities to be used, such as natural gas, diesel oils, coal gas, biogas and other hydrocarbon-contained fuels (though these will require some pre-reforming).

The SOFC produces high-grade waste heat for co-generation and topping cycles, however, its high operating temperature also brings the disadvantages. At 1000°C, the standard materials selected for fuel cell system such as stainless steels can not be used for current collector, not only does the high temperature, but also the environment associated with impure fuels can be corrosive. Therefore, expensive materials maybe required within the fuel cell and the associated equipment in the balance of plant.<sup>[1,6]</sup> The high temperature also reduce the negative free energy of formation of water, lowering the open circuit potential of the SOFC by the amount of 100 mV when comparing with the MCFC running at about 650°C. The SOFC is therefore could be less efficient, though the addition of a turbine cycle or co-generation application may redress the balance. The combination of SOFCs with gas and steam turbines could increase the overall efficiency of conversion of natural gas into electricity to about 70%.

Present interests in SOFCs seemed to be shifting towards lower operating temperatures because the advantages regarding to materials for making fuel cell stack and balance of plant will easily be found. Material costs, and reduction of structural problems, possibly enhanced lifetime and new markets. More recently, other oxides such as ceria

(CeO<sub>2</sub>) and lanthanum gallate (LaGaO<sub>3</sub>) have gained interest as new electrolyte system for SOFCs operating at lower temperatures.

### 2.3. Fuel cell applications

Fuel cells have many advantages compared to conventional electric power generation systems, such as high conversion efficiency and environmental compatibility. The successful practical applications of fuel cells were for space program in the 1960s, to supply electricity and drinking water for the astronaut.<sup>[12]</sup> Fuel cells have been widely investigated for their potential uses in transport and power generation applications in many countries in the world.<sup>[9]</sup> The prospect for exploiting fossil fuels more efficiently made fuel cell more promising than other alternatives. Fuel cells can power virtually anything that run on electricity, for terrestrial applications can be classified into categories of portable, stationary, or transportation power uses.<sup>[5,6]</sup>

### 2.4. Solid oxide fuel cells

Solid oxide fuel cell (SOFC) has been considered as one kind of green energy in the 21<sup>st</sup> century, because it has high energy conversion efficiency and ultra-low emissions of air pollution.<sup>[13]</sup> The solid oxide fuel cell (SOFC) is a milestone demonstration of new technology at the dawn of a new millennium. It opens up new possibilities for sustainability and efficiency in environmental protection. Not only will it assist in the development of the necessary technologies, but also further open up the debate on what is possible and what is desirable in the employment of clean power generation.

SOFCs have recently emerged as a high temperature fuel cell technology. A fuel cell system usually utilizes a solid ceramic as the electrolyte and operates at extremely high temperature (600-1000°C).<sup>[1,10]</sup> This high operating temperature allows internal reforming performance, promotes rapid electrolysis with metal, be able to use a wide variety of fuels, and produces high quality by-product heat for co-generation.<sup>[1]</sup>

### 2.4.1 Advantages of SOFCs

Solid oxide fuel cells (SOFCs) offer a clean, pollution-free technology to electrochemically generate electricity at high efficiency. These fuel cells present a number of advantages over other types of fuel cells and distributed power generation systems, in particular, the advantages are:

(i) Greater efficiency; SOFCs operate at high temperature which enables their integration with other new energy technologies such as micro-turbines or PEM fuel cells to create electricity generation products with over 60 percent efficiency cannot be obtained by any other combination of technologies.

(ii) Solid state devices; all components of SOFCs are made from ceramic materials, there are no moving parts or corrosive liquid. These features allow for the development of electricity generation systems that are rugged, highly reliable and require low maintenance.<sup>[8]</sup>

(iii) Flexibility of fuels; one of the main attractions of SOFC over other fuel cells is their ability to handle more convenient hydrocarbon fuels—other types of fuel cell have to rely on a clean supply of hydrogen for their operation. High operating temperature SOFCs allow them to reform hydrocarbons within the system either in a reformer or directly on the anode side of the cell. High system efficiency could be achievable with various hydrocarbon fuels such as diesel, biogas, propane, butane, methanol and liquefied petroleum.

(iv) Low noise and air emission; SOFCs allow for superior flexibility in locations for social community because they do not produce any emissions that are toxic to health, with practically no emission of  $\text{NO}_x$  and  $\text{SO}_x$ .

(v) Broad product range capability; SOFC technology can support distributed generation products such as generators and combined heat and power units in the capacity ranges from small residential to large industrial sizes, as well as automotive applications. The high operating temperature also results in high-grade exhaust heat, which can be utilized in a wide range of co-generation applications.

For solid oxide fuel cells application, there has not yet been a commercial for the large scale power generation. Fig. 2.2 showed the potential applications of SOFCs at the low power levels, 1-10 Watts,<sup>[9]</sup> for the small SOFC devices such as a battery replacements on the distance areas, rather higher power level, 100W-1 kW, for military applications. A key application of SOFC at the 1-10 kW in order to provide power to residential building and as

auxiliary power units in vehicles. The distributed power generation and co-generation (combined heat and power, CHP), at present is served by combustion engines like diesels or small turbines, with the outputs of 10 kW to a few MW<sup>[9]</sup>.

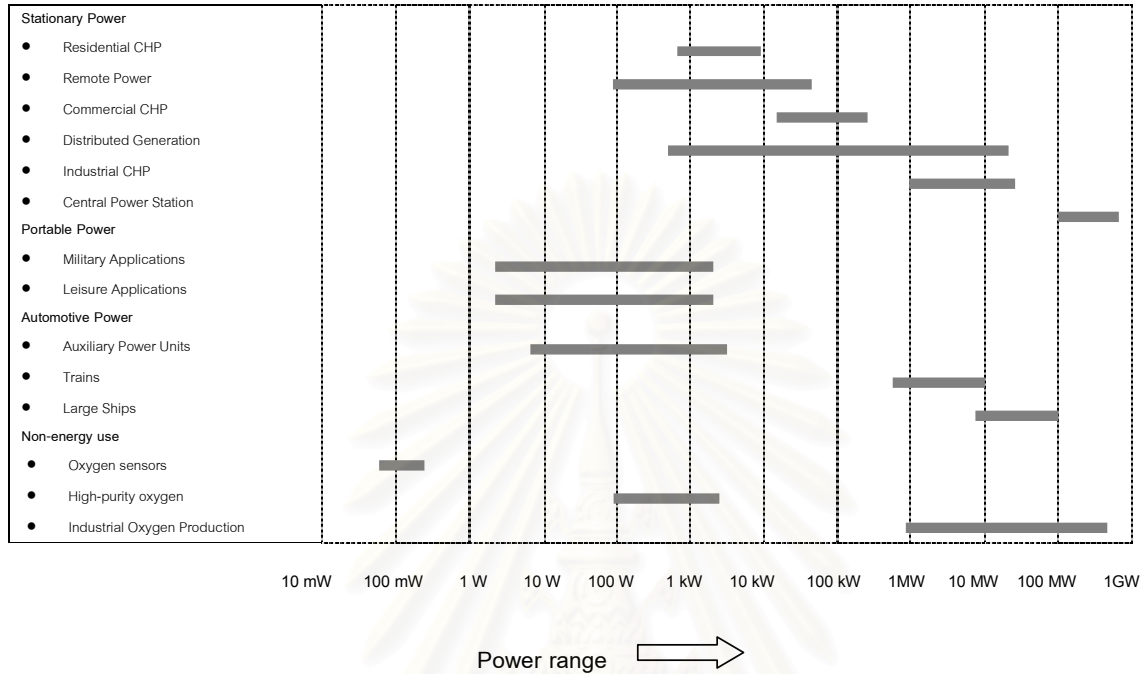


Fig. 2.2 Potential applications of the SOFC technology

#### 2.4.2. Basic principles governing SOFC design and operation

About cell design, solid oxide fuel cell can be categorized into tubular and planar or flat-plate designs, which may consist of one or several single cell per stack unit..<sup>[4,12]</sup>

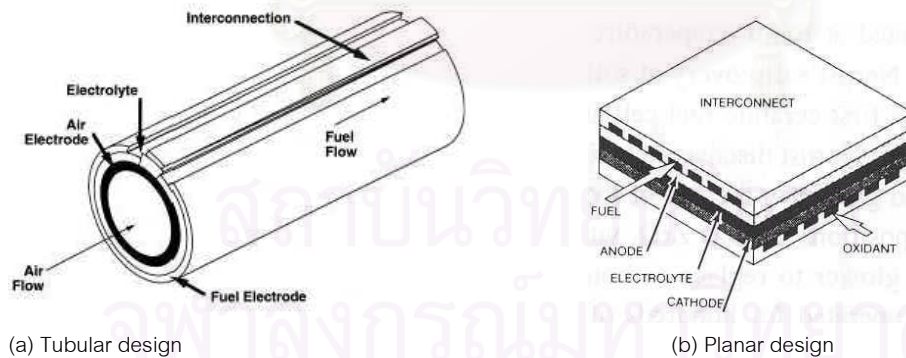


Fig. 2.3 Solid oxide fuel cell designs

#### 2.4.2.1. Electrolyte

The current transfer in solid electrolyte involves the movement of oxygen ions ( $O^{2-}$ ) vacancies. A criteria to select an electrolyte is its ionic conductivity, which is temperature dependent. Ceramic ion conducting electrolytes are available for operating over a wide range of temperatures from 450 to 1000°C. Basic requirements for a solid oxide electrolyte are:<sup>[1,2,16]</sup>

- high oxygen ion conductivity
- low electronic conductivity
- phase stability
- mechanical strength
- gas tightness
- thermal shock resistance
- chemical resistant to reaction gases (i.e. to oxidizing and reducing atmospheres)
- compatibility with electrode and interconnect materials
- moderate materials and fabrication costs

The thickness of electrolyte is most likely to be dictated by a series of electrochemical and thermo-mechanical properties as well as fabrication constraints. It will influence the electrolyte's electric resistance and consequently the fuel cell operating temperature. There are two possibilities to reduce fuel cell operating temperature, one is to reduce electrolyte thickness, and another is to use electrolytes with lower thermal activation energy. Cross-plane internal resistance losses also affect electrolyte performance.

#### 2.4.2.2. Electrodes

The cathode acts in oxidation atmosphere where oxygen molecules are reduced to oxygen ions. At high temperatures, it is particularly strong oxidizing environment, which made it not possible to use lower cost metals but favor the use of noble metals, semi-conducting oxides, or conducting metal oxides. The anode acts in the reducing environment of the fuel gas and it allows for the use of a range of metals, of which porous nickel has been the most widely employed. SOFC electrodes must meet the following requirement:<sup>[1,2,6]</sup>

- good electronic conductivity
- high electrochemical activity
- good adherence to other cell components

- thermodynamic stability
- chemical inertness
- minimal inter-diffusion with adjacent materials
- low volatility
- compatible thermal expansion with other cell components
- a superficial resistivity  $\leq 0.2 \text{ ohm/cm}^2$
- ease of fabrication into thin porous layers that resist excessive sintering
- good mechanical strength
- moderate materials and fabrication costs

The polarization loss occurring at the electrodes are the main cause of voltage drop as operating temperature is lowered.<sup>[3]</sup> Watanabe et al. (1994) have shown that the electrode polarization resistance can be strongly reduced by utilizing highly dispersed noble metal catalysts on the electrode surface. However, it is desirable to avoid the use of expensive noble metal catalysts and alternative electro-catalytic solutions are sought.

#### 2.4.2.3. Interconnect

The interconnect material is used to electrically connect the anodes and cathode of stacked cells in series. The requirements of interconnect materials:<sup>[1,6]</sup>

- high electronic conductivity
- low ionic conductivity (especially towards cations)
- chemical and mechanical stability (including low volatility and non-reactivity with adjoining cell components in both air and fuel gas)
- mechanical compatibility (adherence and thermal expansion) with the electrodes and electrolyte
- absence of mass transport effects in the presence of chemical gradients that may lead to the formation of voids or high contact resistances
- no time-dependent phase changes or re-crystallization between  $25^\circ$  and  $1000^\circ\text{C}$
- low materials and fabrication costs

Interconnect materials range from high cost ceramic materials to low cost stainless steel depending mainly on the SOFC operating temperature.<sup>[14]</sup>

#### 2.4.2.4. Materials for SOFC electrolyte component

The most important property of a candidate electrolyte material is the ionic conductivity; which must develop sufficient oxygen ion ( $O^{2-}$ ) conductivity ( $> 0.05 \text{ S cm}^{-1}$ )<sup>[12]</sup>. The classic oxygen ion conductors for SOFC are stabilized cubic zirconia and ceria, based on fluorite structure.<sup>[8]</sup>

(i) Stabilized zirconia-based materials offer the best possibility choice of high oxygen ion conductivity at the operating temperature and sustain ionic conductors in both oxidizing and reducing atmosphere. Especially, yttria-stabilized zirconia ( $Y_2O_3$ -stabilized  $ZrO_2$ ) or YSZ, which has been extensively used to date electrolyte in SOFCs because the material possesses an adequate level of oxygen-ions conductivity which exhibits desirable stability as well as its good mechanical properties.<sup>[1,2,6,15]</sup>

In its pure form,  $ZrO_2$ , does not serve as a good electrolyte primarily because it has too low ionic conductivity. At room temperature,  $ZrO_2$  has a monoclinic (m) crystal structure. The monoclinic structure changed to a tetragonal (t) form above  $1170^\circ\text{C}$  and to a cubic fluorite structure above  $2370^\circ\text{C}$ . The cubic phase existed up to the melting point of  $2680^\circ\text{C}$ . The addition of some aliovalent oxide stabilized the cubic fluorite structure of  $ZrO_2$  from room temperature to the melting point, as well as increasing in oxygen vacancy concentrations. This enhanced the ionic conductivity and led to an extended oxygen partial pressure range of ionic conduction, making stabilized  $ZrO_2$  suitable for use as a SOFCs electrolyte. The most commonly used stabilizing oxides or dopants are CaO, MgO,  $Y_2O_3$ ,  $Sc_2O_3$ , and certain rare-earth oxides. These oxides exhibited a relatively high solubility in  $ZrO_2$  and were able to form the fluorite structure with  $ZrO_2$  which is stable over wide ranges of composition and temperature.<sup>[2,12]</sup>

Stabilization of  $ZrO_2$  with appropriate size of divalent or trivalent cations, for example doping  $ZrO_2$  with  $Y_2O_3$  results in the substitution of  $Y^{3+}$  on the  $Zr^{4+}$  cation sublattice with the formation of oxygen vacancies as charge compensation flaws. The defect formation reaction in  $Y_2O_3$  doped  $ZrO_2$  can be written in Kröger Vink notation as equation (2.4)



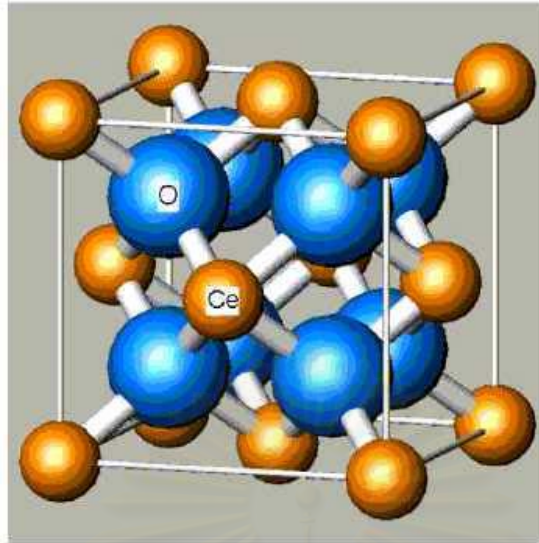


Fig. 2.4 Crystal structure of conducting oxides : fluorite structure, illustrated by stabilized zirconia by Ceria;



Oxygen-ion conduction takes place in stabilized zirconia by movement of oxygen ions via vacancies. The high oxygen vacancy concentration provided the high oxygen-ion mobility. The conductivity in  $\text{ZrO}_2\text{-M}_2\text{O}_3$  system depends on the dopant concentration and dopant ionic radius. Fig.2.4 demonstrates the variety of dopant concentration for the various doped  $\text{ZrO}_2$ .

From Fig.2.5, at the maximum conductivity dopant concentration, the conductivity decreases with increasing in dopant content. These decrease conductivity at higher dopant concentration is believed to be due to defect ordering, vacancy clustering, or electrostatic interaction.<sup>[2,3]</sup> Fig. 2.6 showed the influence of the dopant radii to the conductivity. The dopant,  $\text{Sc}^{3+}$  which has the nearest size of ionic radius to the host ion,  $\text{Zr}^{4+}$ , exhibited the highest conductivity.<sup>[12]</sup>

คำอธิบาย:



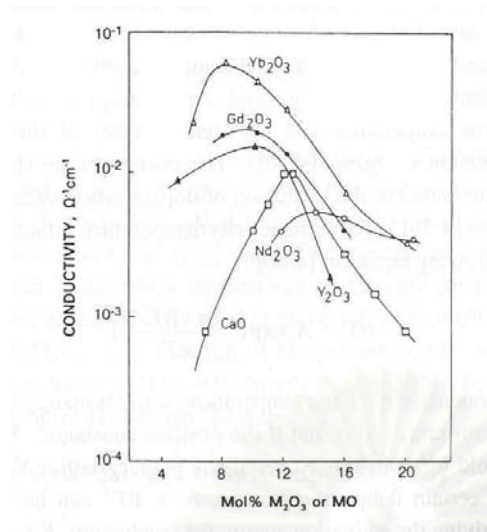


Fig. 2.5 Variation of dopant concentration on the ionic conductivity of stabilized  $ZrO_2$  at Temperature of  $807^\circ C$  [2]

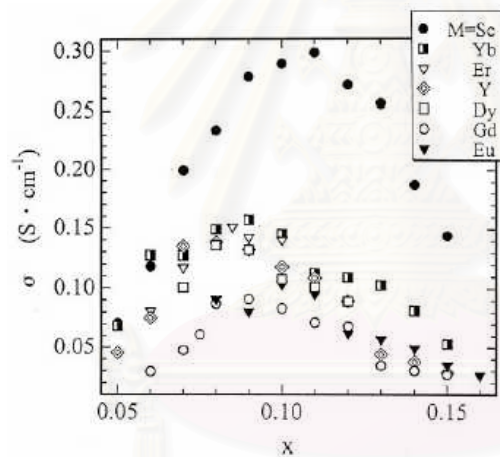


Fig. 2.6 Composition dependence of the electrical conductivity at  $1000^\circ C$  for  $ZrO_2-Ln_2O_3$  (Ln=lanthanide)

Generally, fully stabilized  $ZrO_2$  is preferred as SOFC electrolyte material in order to reach the maximum conductivity. The use of fully stabilized  $ZrO_2$  also avoids the problems of phase transition<sup>[2,3]</sup> associated with partially stabilized materials during cell operation. The conductivity of fully stabilized  $ZrO_2$  as a function of temperature followed Arrhenius-type

behavior. Table 2.2 listed the conductivity data for stabilized  $ZrO_2$  doped with various rare-earth oxides. Although stabilization  $ZrO_2$  with  $Y_2O_3$  does not yield the highest conductivity,  $Y_2O_3$  – stabilized  $ZrO_2$  (YSZ) is the most frequently used as SOFC electrolyte because of their availability and cost.

Table 2.2 The conductivity data for Stabilized  $ZrO_2$  doped with rare-earth oxides<sup>[2]</sup>

Dopant ( $M_2O_3$ )	Composition (mol% $M_2O_3$ )	Conductivity (1000°C) ( $\times 10^{-6}$ S. $cm^{-1}$ )	Activation energy (kJ/mol)
$Y_2O_3$	8	10.0	96
$Nd_2O_3$	15	1.4	104
$Sm_2O_3$	10	5.8	92
$Yb_2O_3$	10	11.0	82
$Sc_2O_3$	10	25.0	62

(ii) Ceria based material, unlike zirconia, pure ceria has the cubic fluorite structure up to the melting point so ceria does not need any stabilization.<sup>[3]</sup> Therefore, Ceria-based solid solutions have been regarded as the most promising electrolyte for intermediate temperature (500-750°C)<sup>[16]</sup> SOFC systems because it has higher ionic conductivity and lower activation energy than that of YSZ. The ionic conductivity of ceria has been extensively investigated with respect to different dopants and dopant concentration. Although, its favorable ionic conductivity is approximately an order of magnitude greater than that of stabilized zirconia, ceria had not, until quite recently, been considered a realistic candidate for fuel cell applications, due to its high electronic conductivity, particularly at increased temperatures in a reducing atmosphere<sup>[8]</sup>,  $CeO_2$  has tendency to undergo reduction  $Ce^{4+}$  ion to  $Ce^{3+}$  ion with the consequent introduction to electronic defects.<sup>[3]</sup>

A dopant concept has been attempted to elevate the ionic domain of  $CeO_2$ . It is generally accepted that  $Gd^{3+}$  - or  $Sm^{3+}$  -doped ceria gives the highest values of conductivity and optimal concentrations are 10-20 mol%. The strong dependence of ionic conductivity due to the small association enthalpy between dopant cation and oxygen vacancy in the fluorite lattice.<sup>[8,15]</sup> Table 2.3 showed the conductivity data for various doped  $CeO_2$  materials.

Table 2.3. The ionic conductivity of doped CeO<sub>2</sub>

Dopant	Content (mol%)	Ionic conductivity at 800°C (10 <sup>-2</sup> S cm <sup>-1</sup> )	Activation energy (kJ/mol)
La <sub>2</sub> O <sub>3</sub>	10	2.0	--
Y <sub>2</sub> O <sub>3</sub>	20	5.5	26
Gd <sub>2</sub> O <sub>3</sub>	20	8.3	44
Sm <sub>2</sub> O <sub>3</sub>	20	11.7	49
CaO	10	3.5	88
SrO	10	5.0	77

From the same dopant concentration, the ionic conductivity of M<sub>2</sub>O<sub>3</sub>-doped CeO<sub>2</sub>, M is a rare-earth, increased with increasing ionic radii.

Another approach to suppress the ionic conductivity reduction of CeO<sub>2</sub> under reducing atmospheres is coating YSZ onto CeO<sub>2</sub>-based electrolytes has been studied by various researchers.<sup>[3,7]</sup> For example, (CeO<sub>2</sub>)<sub>0.8</sub>(Sm<sub>2</sub>O<sub>3</sub>)<sub>0.2</sub> has been coated with an YSZ thin layer (2 μm) on the fuel side to produce a stable SOFC electrolyte.

(iii) The development of other materials for SOFC electrolyte, particularly those possess adequate ionic conductivity at intermediate operating temperature (650-800°C)<sup>[2,17]</sup> has received much interests. Several doped perovskite (ABO<sub>3</sub>) solid electrolytes have been investigated. The perovskite oxides are very interesting because there are two cations, leading to a much wider range of possible oxygen ion conducting materials. Of the perovskites investigated to date, only the lanthanum gallate (LaGaO<sub>3</sub>), shown in Fig. 2.7 based material has been found to be suitable for ionic application.<sup>[17]</sup>

## 2.5. Operating regimes and typical SOFC components

Based on the behavior of ceramic electrolyte material and properties of the interconnect material, three operating temperature regimes can be distinguished as shown in Table 2.4.

- High temperature: > 800°C
- Intermediate temperature: 600-800°C
- Low temperature: 400-600°C

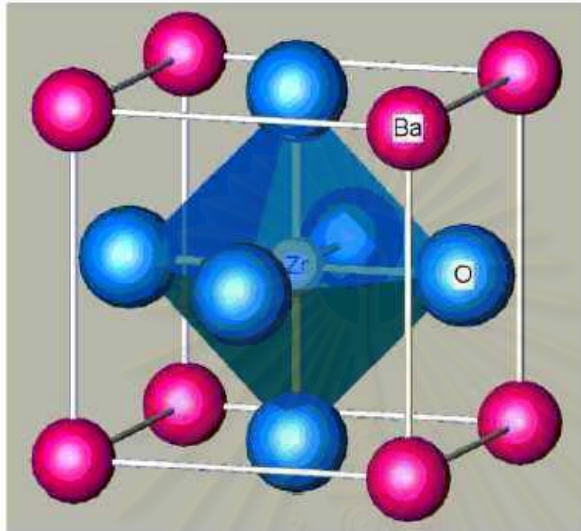


Fig. 2.7 Perovskite structure illustrated the oxygen ion conductor<sup>[8]</sup>

The operating temperature ranges, which are distinguished based on fuel cell component characteristics, will also be characterized by features such as possibility of internal fuel reforming, the possibility in operating in conjunction with gas and steam turbines and the type of balance of plant equipment required.

สถาบันวิทยบริการ  
จุฬาลงกรณ์มหาวิทยาลัย

Table 2.4 Potential SOFC components at different operating temperatures

Operating temperature	Electrolyte	Cathode	Anode	Interconnect
>800°C	Y doped ZrO <sub>2</sub>	La <sub>1-x</sub> Sr <sub>x</sub> MnO <sub>3</sub> (LSM)	Ni-ZrO <sub>2</sub> (-Y <sub>2</sub> O <sub>3</sub> )	Ca or Mg doped LaCrO <sub>3</sub>
500-800°C	- Y or Sm doped ZrO <sub>2</sub> - Ceria-based	La <sub>1-x</sub> Sr <sub>x</sub> Mn <sub>1-y</sub> Co <sub>y</sub> O <sub>3</sub> (LSMC) (diffusion barrier required between cathode and YSZ electrolyte)	Ni-ZrO <sub>2</sub> (-Y <sub>2</sub> O <sub>3</sub> )	Special metallic or cermet bipolar plate; stainless steel (700°C) bipolar plate
400-600°C	Gd, or Y or Sm doped CeO <sub>2</sub> ; Sr or Mg doped LaGaO <sub>3</sub> ; Composite electrolytes (ceria- and zirconia-based layers)	La <sub>1-x</sub> Sr <sub>x</sub> Co <sub>1-y</sub> Fe <sub>y</sub> O <sub>3</sub> (LSCF) used with CeO <sub>2</sub> ; La <sub>1-x</sub> Ca <sub>x</sub> Co <sub>1-y</sub> Fe <sub>y</sub> O <sub>3</sub> (LCCF) used with CeO <sub>2</sub> ; Sm <sub>1-x</sub> Sr <sub>x</sub> CoO <sub>3</sub> (SSC) used with LaGaO <sub>3</sub>	Ni-ZrO <sub>2</sub> (-Y <sub>2</sub> O <sub>3</sub> ) Oxide materials (e.g La <sub>1-x</sub> Ca <sub>x</sub> CrO <sub>3</sub> ); Stainless steel mesh and powder for use with methanol	Stainless steel bi-polar plate

### 2.5.1. High-temperature operating regime (>800°C)

Most research efforts up to date have investigated the high temperature SOFCs and a number of stack systems have been developed and are at different stages of testing and demonstration. An advantage of the high temperature operating regimes is that internal reforming can occur spontaneously. Operation temperature above 800°C require costly materials (e.g LaCrO<sub>3</sub>-based bipolar plate). Common problems are voltage degradation due to electrode sintering and interfacial reactions, and mechanical stress due to differential shrinkage and internal expansion. Also, high temperature sealing is a challenging problem in planar SOFCs. Materials suitable for high temperature operation are YSZ system for electrolyte, strontium doped lanthanum manganate (LSM) cathodes and Ni-cermet anode.<sup>[6,12]</sup>

### 2.5.2. Intermediate-temperature operating regime (600-800°C)

SOFCS operating at intermediate and low temperature regimes are at less developed stage than the high temperature one, however, much interests in lower operating temperatures have gained importance more recently mainly as a means to reduce costs. Cell and system costs at these operating temperature can be greatly reduced compared to high temperature operation because of the use of low cost materials (e.g. stainless steel bipolar plate instead of ceramic interconnects).<sup>[18,19]</sup> Lower temperatures may possibly lead to longer lifetimes and less complicated and costly designs. In addition, the temperature range considered is suitable for operation in combination with steam turbines.

In term of material selection for operating temperatures between 600-800°C, the conventional 8 mol%  $Y_2O_3$ - $ZrO_2$  electrolytes is replaced by either  $Ce_{0.9}Gd_{0.1}O_{1.95}$  (GDC 10mol%) or  $La_{0.9}Sr_{0.1}Ga_{0.8}Mg_{0.2}O_3$  (LSGM).<sup>[19]</sup> Ceria-based solid solution have been regarded as the most promising electrolytes in the intermediate temperature fuel cell system<sup>[20]</sup> due to the ionic conductivity of ceria-based is higher than that of yttria-stabilized zirconia at this temperature range. The ceria-based materials have ionic conductivity at 0.1-1.0 S/cm.<sup>[21]</sup> Strontium and manganese doped lanthanum-cobaltate (LSMC) showed a thermal expansion compatible with that of YSZ electrolyte, and Ni-cermet appears as the most likely choice for the anode as it offers suitable electrochemical and thermo-mechanical properties and has a moderate cost.

### 2.5.3. Low-temperature operating regime (400-600°C)

Operation further reductions at lower temperatures (400-600°C) give rise to further reductions in materials and design costs and creates opportunities for markets other than stationary power generation (e.g. transport). Low cost metals and metal fabrication techniques can be employed and gas sealing problems are easier to overcome.<sup>[21]</sup> Also, cheaper materials can be used for the balance of plant equipment including heat exchangers, pumps, etc. Longer lifetimes are likely to result from lower operating temperatures and contributing to the economic viability of the fuel cell stack. The upper temperature ranges of 600-700°C are also suitable for indirect internal reforming of methane although direct internal reforming will take place at 600°C.

Candidate materials suitable for electrolyte at lower operating temperature, including  $\text{CeO}_2$  and  $\text{LaGaO}_3$ -based materials. Previous investigations showed  $\text{CeO}_2$ -based electrolyte had power densities comparable to those of zirconia-based systems<sup>[1]</sup> towards the upper end of the temperature range ( $700^\circ\text{C}$ ) and a good thermal expansion match with ferritic stainless steels. For electrode materials, strontium and cobalt doped lanthanum ferrate (LSCF) is a suitable cathode material for use with ceria-based electrolytes for operation at high temperatures close to  $700^\circ\text{C}$ . Other interesting candidate for cathode is strontium doped samarium-cobaltate (SSC).<sup>[10,11]</sup> Ni-cermet has been the most commonly used as anode material so far, however, its use in this temperature range may cause problems such as the formation of carbon deposits and NiO formation which may reduce the cell performance.<sup>[22]</sup>

## 2.6. Tape casting technique

Tape casting process was first described by Glenn Howatt 50 years ago. It is also known as doctor blading and knife coating. The process is well known in many industries, including plastic, paper and paint manufacturing.<sup>[22]</sup>

One of the major advantages of tape casting process is that it is the best way to form large-area, thin flat ceramic or metallic parts. Which are virtually impossible to press and extrude.

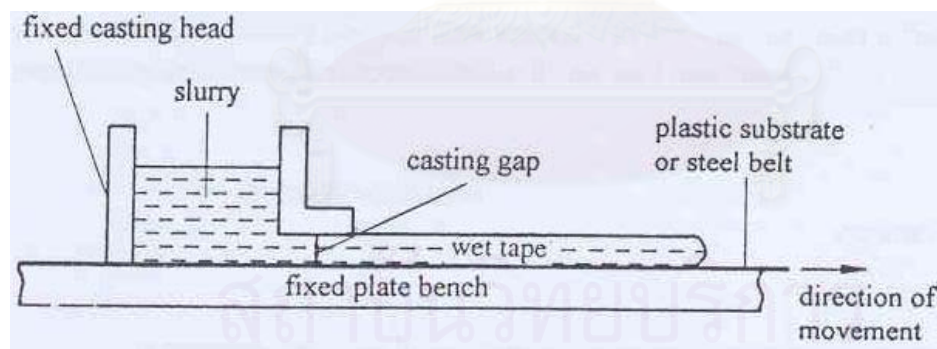


Fig. 2.8 A diagrammatic view of a slurry layer is doctor bladed onto a substrate<sup>[23]</sup>

Fig. 2.8 illustrated the principle of the tape casting process. The equipment usually consists of a stationary doctor blade, a moving carrier and a drying zone.<sup>[23]</sup> In the typically tape casting



process, the ceramic powder slurry is poured into a reservoir or cavity behind the doctor blade, and the carrier to be cast upon is set in motion. The doctor blade gap between the blade and carrier defines the wet thickness of the tape being cast. This process can be depicted by a flow chart according to Fig. 2.9.

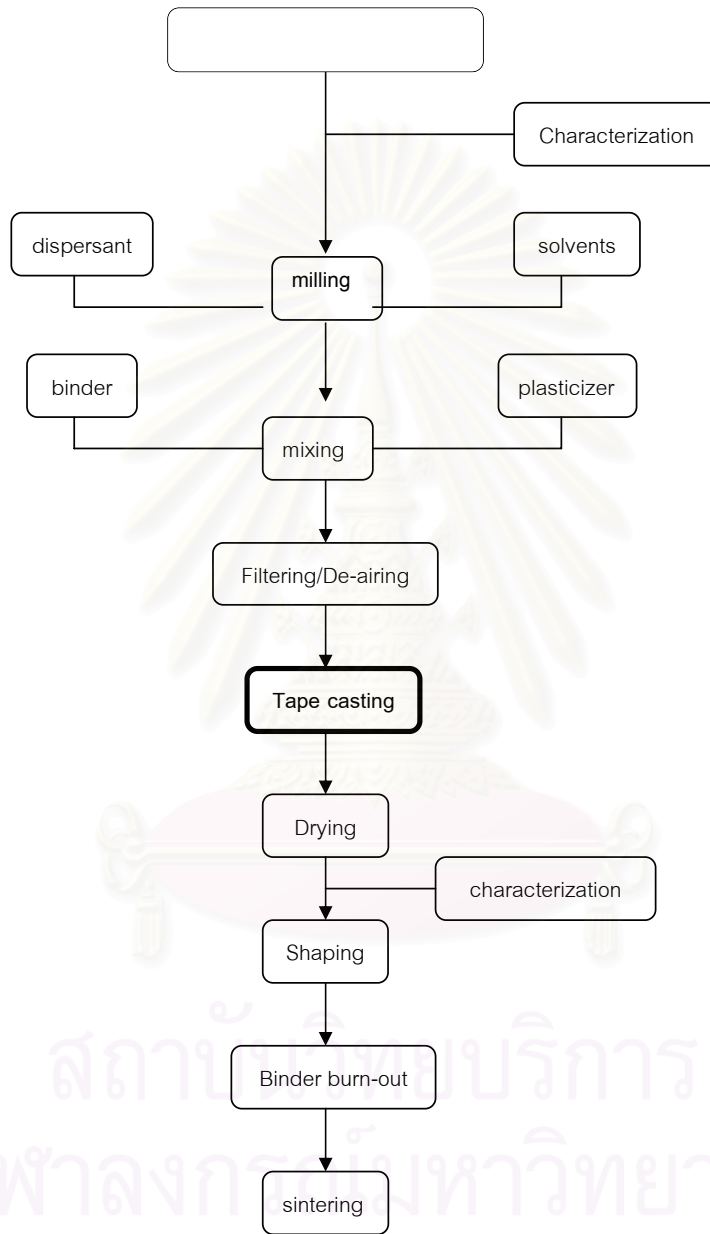


Fig. 2.9 Flow chart illustrating the general production process of ceramic tape-based components<sup>[24]</sup>



### 2.6.1 Water-based tape casting

The technology for water-based tape casting has existed for many years, improving in both expertise and component capability as time progress, but is still not economically practical for many tape producers and manufacturers. Comparison between organic solvent-based tapes and water-based tapes, organic solvents are easier to process and make higher-quality tapes with superior performance. For the water-based slurry, water had an extremely high surface tension compared to organic solvent such as ethanol, methyl, ethyl ketone, acetone, or toluene. This factor tend to make water-based processing quite a bit more challenging than processing in organic liquids.<sup>[23]</sup>

In the recent years, the environmental and health issues for manufacturing process including the tape casting have received special attention. Non-aqueous solvents have lower boiling points but require special precautions concerning toxicity and inflammability. Typically, organic solvent recovery systems are needed to control emissions of compounds into atmosphere. On the other hand, an aqueous system has advantages of non-toxicity and low cost, regarding cleaning process.<sup>[25]</sup>

### 2.6.2 Slurry formation

In the slurry preparation process, it can be divided into two important parts. During the first stage, the slurry should contain only the powder, the solvents, and the dispersing agents. To avoid the damage of the long molecular chains of the polymer, the binders should not be added in this stage.

The second stage of the process should be devoted to mixing this slurry with the more viscous plasticizers, and any additional functional additives. Times for milling and mixing should be long enough to achieve stable conditions and a high homogeneity. Finally, immediately before casting, organic or inorganic residues such as binder lumps or small debris of grinding medium must be removed from the slurry by passing it through a fine-meshed sieve (5-30  $\mu\text{m}$  openings).<sup>[25]</sup>

Compared with non-aqueous solvents, the variety of water-soluble binders, plasticizers and dispersing agent is restricted to a few systems.<sup>[23]</sup> Some general rules can be inferred for the preparation of tape casting slurry:

- (i) The ratio between organic components and ceramic powder must be low as possible.
- (ii) The amount of solvent must be fixed at minimum to maintain a homogeneous slurry.
- (iii) The amount of dispersant must be minimum necessary to ensure the stability of the slurry.
- (iv) The plasticizer to binder ratio must be adjusted to make the tape flexible, resistant and easy to release.

The minimal amount in water and organic additives to prepare a slurry with satisfactory properties should be used. The ceramic powder charges vary from about 25-80 wt.%. The organic additives are always above 18 wt%, while the water content ranges from less than 20 upto 70 wt.%.

#### 2.6.2.1 Solvent

In the ceramic slurry, the solvent dissolves the organic materials and distributes them uniformly, in this vehicle which carries the ceramic particles in a suspension until it evaporates and leaves a dense tape on the carrier.

A non-aqueous suspension dries quickly and produces green sheets having a high density and fine surface appearance. A water-based system has the disadvantages of high evaporation latent heat and inferior drying characteristics.<sup>[25]</sup>

#### 2.6.2.2 Ceramic powder

In any materials fabrication process, the most important ingredient in batch formulation is the solid part, which can be ceramic, metallic, or composite powders. After binder removal and final consolidation, the powders are the only portion of the batch left, and they define the properties of the produced. The other ingredients in the batch formulation such as the solvents, plasticizers, binder, and surfactants, are there simply to facilitate the fabrication of the desired shape. Essentially, the tape casting process is used to obtain and

hold the powder particles in the needed configuration so that, after sintering, the final part has the required size, shape, and properties.<sup>[23]</sup> A well-characterized a starting powder is necessary to increase reliability in processing and particular in aqueous tape casting.<sup>[25]</sup>

### 2.6.2.3 Polymer binder

The binder provides strength to green tapes after solvent evaporation. The tape can then be easily manipulated and retained in the desired shapes before sintering. Organic binders are either dissolved or dispersed in water as an emulsion. Most soluble binders are long chain polymer molecules.

Binders strongly affected the rheology of the suspension, it changed the characteristics from Newtonian (for pure water) to pseudo-plastic in most cases. A pseudo-plastic behavior is characterized by decreasing viscosity with increasing shear rate. The viscosity of aqueous slurry is much less compared to organic solvent slurry. Typical values are in the range of  $\sim 0.1$  to  $\sim 20$  Pa s for a shear rate of  $50 \text{ s}^{-1}$  at room temperature.<sup>[25]</sup>

### 2.6.2.4 Plasticizer

Plasticizers are organic substances with molecular weight in comparable with binders and are soluble in the same liquid. They are additives, which soften the binder in the dry or semidry stage. The plasticizer tends to reduce the strength. Binders and plasticizers are intimately mixed after drying. The plasticizer increases the flexibility and work ability by breaking the close alignment and bonding of the binder molecules. Table 2.5 listed the water-soluble plasticizer used in tape casting.

Table 2.5 Common plasticizers used in aqueous tape casting<sup>[24]</sup>

<i>Compound</i>	<i>Formula</i>
Glycerol	$\text{HOCH}_2\text{CH}(\text{OH})\text{CH}_2\text{OH}$
Poly(ethylene glycol)	PEG $\text{HO}-(\text{CH}_2\text{CH}_2)_n-\text{H}$
Poly(propylene glycol)	PPG $\text{HO}-(\text{CH}_2\text{CH}_2\text{CH}_2\text{O})_n-\text{H}$
Dibutyl phthalate	DBP $\text{C}_{16}\text{H}_{22}\text{O}_4$
Benzyl butyl phthalate	BBP $\text{C}_{15}\text{H}_{20}\text{O}_4$

### 2.6.2.5 Dispersant

A dispersant is also called deflocculant, wetting agent or surfactant, which coated the ceramic particles and kept them away from each other in a stable suspension.<sup>[23]</sup> The most frequently used dispersants for water-based tape casting are polyelectrolytes.<sup>[25]</sup> The important role of dispersant in the tape casting slurry are: (i) to separate the ceramic particles and also hold them in suspension in order for the binder to coat them individually, (ii) to increase solid loading in suspension and maintain the viscosity after binder addition, (iii) to decrease the amount of solvent in ceramic slurry in order to obtain faster tape drying with less shrinkage, (iv) in order to have cleanly burn out.<sup>[25]</sup>

Table 2.6 Selected dispersants for tape casting slurries<sup>[23]</sup>

<i>Aqueous systems</i>	<i>Non-aqueous systems</i>
Sodium silicates	Chloroform
Sodium carbonates	Methylene chloride
Sodium polyphosphates	Ketones, ethers
Ammonium polyphosphates	Methyl ethyl ketone + methyl alcohol

### 2.6.3 Rheology of tape casting slurry

The tape casting technique is a potential method to fabricate thin, flat ceramic parts such as capacitors, substrates, piezoelectric actuators, etc. For a variety of these products, different tape casting slurries are used. The slip rheology controls the quality of final product, and their rheological behavior depends on the type and powder content, binder, and solvent as well as organic additives.<sup>[26]</sup>

In comparable to organic solvents, aqueous based system has the advantage of low toxicity and environmental safety, however, water media has a strongly effect to the slurry rheology. Water gives a higher surface tension than organic solvents and the solubility of binders in water is also limited. Therefore, this study used water-based acrylic binder to prepare the casting slurry. It is designed to act like solvent based binders in term of slurry processing. The binder concentrate contains mild defoamers to minimize foam, plasticizers to

adjust flexibility, wetting agent to lower surface tension, de-ionized water, and resins to produce basic tapes.

In addition, the slurry should exhibit pseudo-plastic behavior that is characterized as having a shear-thinning behavior. The viscosity of a pseudo-plastic slip depends on the shear stress applied at the time. This behavior is beneficial in the tape casting process: during passing the blade, the viscosity is decreased due to shear forces, and immediately after the blade the viscosity increases rapidly to suppress uncontrolled flow and to prevent sedimentation of the ceramic particles. Thixotropy and any other time-dependent behavior are not desirable.<sup>[27]</sup>

## 2.7. Electrical conductivity of SOFC electrolyte

The ionic conductivity of stabilized  $ZrO_2$  has been extensively investigated. The behavior of the ionic conductivity of material is influenced by many factors such as dopant and concentration<sup>[12]</sup> of dopants, temperature, atmosphere, and grain boundary. For conductivity measurement, the ionic conductivity of ceramics including stabilized  $ZrO_2$  is determined by the complex impedance measurements, which depends on the microstructures, especially grain boundaries of the material and the migration of vacant oxygen sites. The ionic conductivity can be expressed as the product of the volume concentration  $n$ , the mobility  $m$  and the electric charge  $q = 2e$  of mobile oxygen vacancies; as shown in equation (2.5) below,

$$\sigma = n \cdot m \cdot q \quad (2.5)$$

where  $\sigma$  is the total conductivity, in this equation both charge carrier concentration  $n$  and mobility  $m$  are included. The ionic conductivity increases exponentially with increasing temperature.<sup>[27]</sup>

$$\sigma = \sigma_0 \exp(-\Delta E_\sigma / kT) \quad (2.6)$$

where  $\Delta E_\sigma$  is the activation energy of conductivity,

$k$  is the Boltzmann constant.

$T$  is the temperature (K)

In cubic zirconia, the ionic conductivity decreases with increasing the amounts of dopant as explained by Hohnke<sup>[27]</sup> that the formation of immobile associated complexes between oxygen vacancies and cation defects which reduces the amount of free charge carriers with increasing amount of dopants.

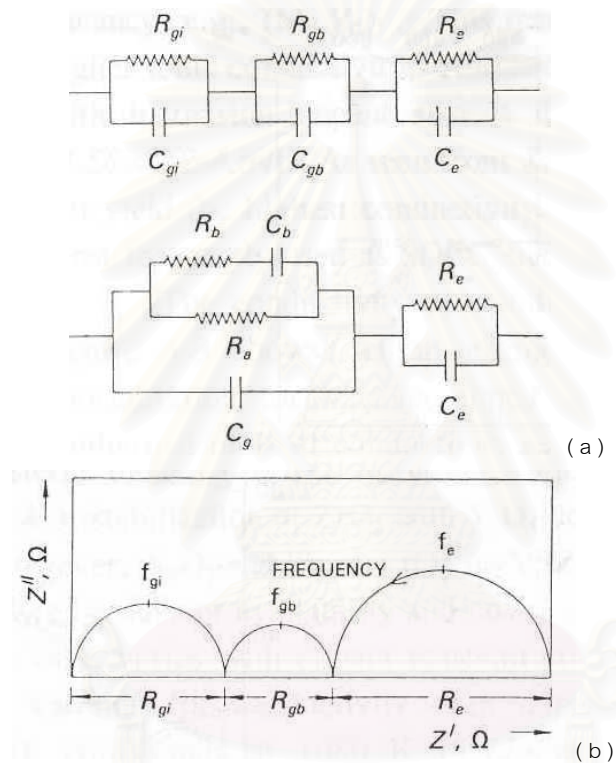


Fig. 2.10 Equivalent circuit ( a ) and schematic complex impedance plot of polycrystalline ( b )<sup>[3]</sup>

Complex impedance measurement is generally used to investigate the ionic conductivity of the electrolytes (and ceramic in general), which depends on the microstructures, especially the grain boundaries. From Fig.2.10 (a) the individual components of the equivalent circuit are related to the resistivity of the materials. Fig 2.10 (b) is a schematic plot of AC impedance, which showed 3 semi-circles. The first semicircle represents the bulk

(or lattice) conductivity, where the 2<sup>nd</sup> semi-circle represents the grain boundary conductivity. The third semicircle plays the electrode role of conductivity. [28]

## 2.8. Thermal expansion

The thermal expansion coefficient of undoped ZrO<sub>2</sub> single crystals is about  $8.12 \times 10^{-6}$  cm/cm.K in the temperature range of 20° to 1180°C, whereas doped ZrO<sub>2</sub> materials typically have higher thermal expansion coefficients. For instance, the thermal expansion coefficient of ZrO<sub>2</sub> crystals doped with 4 wt.% CaO is about  $10.08 \times 10^{-6}$  cm/cm.K. Many previous studies reported the values of thermal expansion of Ytria stabilized zirconia at various temperatures as the following table. [3,29]

Table 2.7 Thermal expansion data for YSZ materials

Dopant Content	Temperature (°C)	Thermal expansion coefficient ( $10^{-6}$ cm/cm.K)
3 mol% Y <sub>2</sub> O <sub>3</sub>	1000	10.5
6 mol% Y <sub>2</sub> O <sub>3</sub>	1000	10.2
7.5 mol% Y <sub>2</sub> O <sub>3</sub>	25-1000	10.0
8 mol% Y <sub>2</sub> O <sub>3</sub>	100-1000	10.8
9 mol% Y <sub>2</sub> O <sub>3</sub>	960	9.8

It is obvious that the thermal expansion of electrolyte materials has to be in a good match with the values for electrodes, regarding the thermal compatible during heating up and cooling down procedure. The basic composition used for anode (30vol% NiO-YSZ) has the thermal expansion  $\sim 10.5 \times 10^{-6}$  cm/cm.K, which the value depends on the amount of Ni. [2] The cathode (LSM) component with 20mol% of Sr has the thermal expansion value of about  $12.4 \times 10^{-6}$  cm/cm.K.

## 2.9. Mechanical Property

The mechanical properties of a YSZ electrolyte fabricated by tape-casting generally vary depending on the characteristics of the starting powders used in the fabrication such as particle size, size distribution, agglomeration strength, fabrication route and conditions. For



instance, YSZ sheet produced by tape calendaring have superior mechanical properties with a mean strength about 15% higher than the same material made by tape casting technique.<sup>[3]</sup> The mechanical property of this study's interest was the bending strength, and from previous studies, the bending strength of 8 mol% YSZ (bulk) is about 300-400 MPa<sup>[30]</sup> at room temperature. At present, few data reported the mechanical property at elevated temperature. Research works<sup>[3]</sup> showed the mean strength of YSZ was about 368 MPa, at room temperature, compared to 280 MPa at high temperature (900°C).

#### 2.10. Previous Research up-to-date (1997-2004)

T.-L. Wen et al.<sup>[13]</sup> worked on the SOFC material for electrolyte, anode, cathode, interconnect and sealant for planar SOFC stack. In the detail of research, the team used alumina fiber to reinforce the YSZ electrolyte by tape casting technique combined with isostatic pressing. The  $(Pr, Nd, Sm)_{1-x}Sr_xMnO_3$  cathode film was prepared on YSZ membrane by spin coating technique and sintered at 1400°C.

Ni-YSZ cermet was used as the anode material in this study. It was found that 60 wt% NiO in the cermet is the optimum composition for the conductivity and the adherence to YSZ by screen printing method. The 30-40  $\mu\text{m}$  thick film of anode was formed after firing at 1350-1400°C. Material used for the interconnect was the chromium-based alloy as the substrate and coated with  $La_{0.7}Sr_{0.3}CrO_3$  (LSC) by plasma flame sprayed technique with thickness of 50  $\mu\text{m}$  on both sides.

To separate the fuel gas and oxidation gas, sealing constituent was the important part. The glass-ceramic system of  $SiO_2$ -CaO- $Al_2O_3$  was used as a sealant. The 10-cell stack with the dimension of 40x40  $\text{mm}^2$  was constructed and tested at 1000°C. It showed an output power of 10W and a power density of 110  $\text{mW}/\text{cm}^2$ .

J. Ma et al.<sup>[15]</sup> studied the system of  $Ce_{0.8}Gd_{0.2}O_{2-\delta}$  ceramics derived from commercial sub-micron size of  $CeO_2$  and  $Gd_2O_3$  powders for using as electrolytes in solid oxide fuel cells. The research started with 20 mol% of  $Gd_2O_3$ -doped ceria prepared as an electrolyte by the conventional mixed-oxide method. It was found that the dissolution of  $Gd_2O_3$  in  $CeO_2$  was completed at 1600°C for 5h of sintering profile. The results suggested that  $Gd_2O_3$  doping

increased the sintering temperature and retarded densification, and also suppressed grain growth as compared to un-doped  $\text{CeO}_2$ . The sample sintered at  $1600^\circ\text{C}$  for 5h exhibited the maximum conductivity at above  $500^\circ\text{C}$ , while the sample sintered at  $1550^\circ\text{C}$  for 5h gave the maximum conductivity at below  $500^\circ\text{C}$ .

Snijker et al. <sup>[31]</sup> studied the aqueous tape casting of yttria (8 mol%) stabilized zirconia for SOFC electrolyte, using natural product binder. The method was environmentally friendly since it was water-based and used a natural compound as a binder. The gelatin binder readily reduces the surface tension; yet the addition of a surfactant as required in order to figure that apply to non-aqueous systems. In addition the suspension formulation allowed a solid content as high as 66 wt%. The microstructure of the sintered tape showed the size of grains were in the range of 2-10  $\mu\text{m}$ . The cross-section of sintered tapes found a fairly dense layer with only little closed pores.

J. Liu et al. <sup>[32]</sup> investigated the properties of YSZ (8 mol%) electrolyte made by plaster casting method for the applications in SOFCs. The obtained density of the samples increased as the sintering temperature increased. The relative density sintered at  $1550^\circ\text{C}$  for 12 h was about 93% with the thickness of 0.2 mm. Cubic fluorite structure appeared in the specimens sintered above  $1300^\circ\text{C}$ . The activation energy for the samples sintered for 12 h at 1300, 1400 and  $1550^\circ\text{C}$  are 0.66, 0.86, and 0.98 eV, respectively.

## Chapter 3

### Experimental work

This chapter will detail the experimental procedure of the electrolyte powder synthesis and characterization, slurry preparation using water-based system fabrication by tape casting technique, de-binding and firing conditions including the sintered tape characterizations.

#### 3.1 Powder preparation and characterization

In this study, the basic compositions for SOFC electrolyte systems are 1) yttria-stabilized zirconia (YSZ) and 2) ceria-based system with  $Gd_2O_3$  -addition. The followings were the powders used in this study which were from different sources as shown in Table 3.1.

Table 3.1 Types of powder and sources

Powder	Purity (%)	Source
3YSZ	99.9	Magnesium Elektron Inc., UK (MEL)
8YSZ	99.9	Magnesium Elektron Inc., UK (MEL) Tosoh Corporation, Japan
10YSZ	99.9	Magnesium Elektron Inc, UK (MEL) Daiichi, Japan
$CeO_2$	99.9	Alfa Aesar, USA
GDC (10 mol%)	-	Mixed oxide route
GDC2 (20 mol%)	-	Mixed oxide route

Particle size and size distribution of all electrolyte systems were characterized by a laser particle-sized analyzer, (MALVERN instruments: mastersizer-S). This equipment used for testing and analyzing the particle size range from 5 nm to 900  $\mu m$  with the light scattering technique. High purity commercial powders of  $CeO_2$  (99.9%) and  $Gd_2O_3$  (99.9%) were used as the starting materials for mixed oxide GDC (gadolinia doped ceria) synthesis.

For gadolinia doped ceria (GDC) powder, 10 and 20 mol% of  $Gd_2O_3$  were doped into ceria in order to obtain the solid solution and prepare for an electrolyte for SOFC via the conventional mixed-oxide route from high purity commercial  $CeO_2$  and  $Gd_2O_3$ . The mixtures of  $Ce_{0.9}Gd_{0.1}O_{1.95}$  and  $Ce_{0.8}Gd_{0.2}O_{1.90}$  were ground in de-ionized (D.I.) water with zirconia media balls for 13-15 hrs. Then, the precursor was dried at  $100^\circ C$  overnight to evaporate dissolving water and GDC powders were calcined at  $1050^\circ C$  for an hour. A flow chart of the GDC powder preparation was shown in Fig. 3.1.

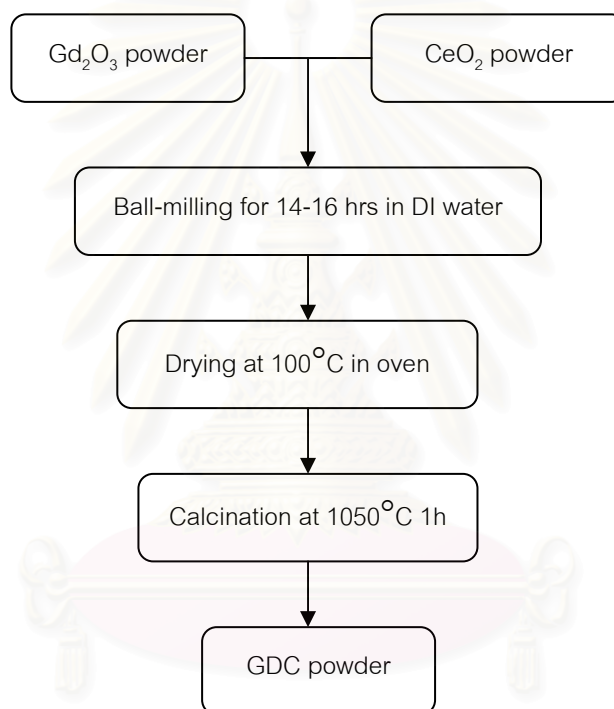


Fig 3.1 The diagram of GDC powder preparation

### 3.2 Slurry preparation

To prepare electrolyte slurry for tape casting, ceramic powder was mixed with other polymer additives to make the proper viscosity of slurry. In this study, water-based system was used in order to avoid the toxic of organic solvents.

Aqueous tape casting is an environmentally friendly method to fabricate a thin flat ceramic sheet such as a SOFC electrolyte.<sup>[15]</sup> In general, the starting suspension for tape casting, fundamentally contained the ceramic powder or powder mixture as the functional phase, solvent (either organic or water), binder, plasticizer and additives such as defoamer and dispersant.<sup>[18]</sup> Powders were mixed in a ball-mill with de-ionized water as the solvent with ammonium salt as a dispersant. The mixing time was 12-16 hours before discharging the slurry. More aqueous binders, plasticizers and de-foamers were added into slurry to adjust viscosity. The slurry composition prepared in this study based on this following formulation.

Ceramic powder	62	wt. %
De-ionized water	20	wt. %
Water based acrylic binder + Plasticizer	17.6	wt. %
De-foamer	0.4	wt. %
Dispersant (ammonium salt)	0.2	wt. %

The step of electrolyte slurry preparation is shown in the diagram below (Fig. 3.2). First stage, the electrolyte powder was mixed with de-ionized water in a ball-mill with a small amount of water based acrylic binder, dispersants, plasticizer, and defoamers for 12-16 hrs or overnight. After discharging, the second stage of adding another half of binder into the slurry was done and small amount of defoamers and then only stirring by magnetic stirrer for 4 hrs. The slurry was then ready for tape casting in the next step.

สถาบันวิทยบริการ  
จุฬาลงกรณ์มหาวิทยาลัย

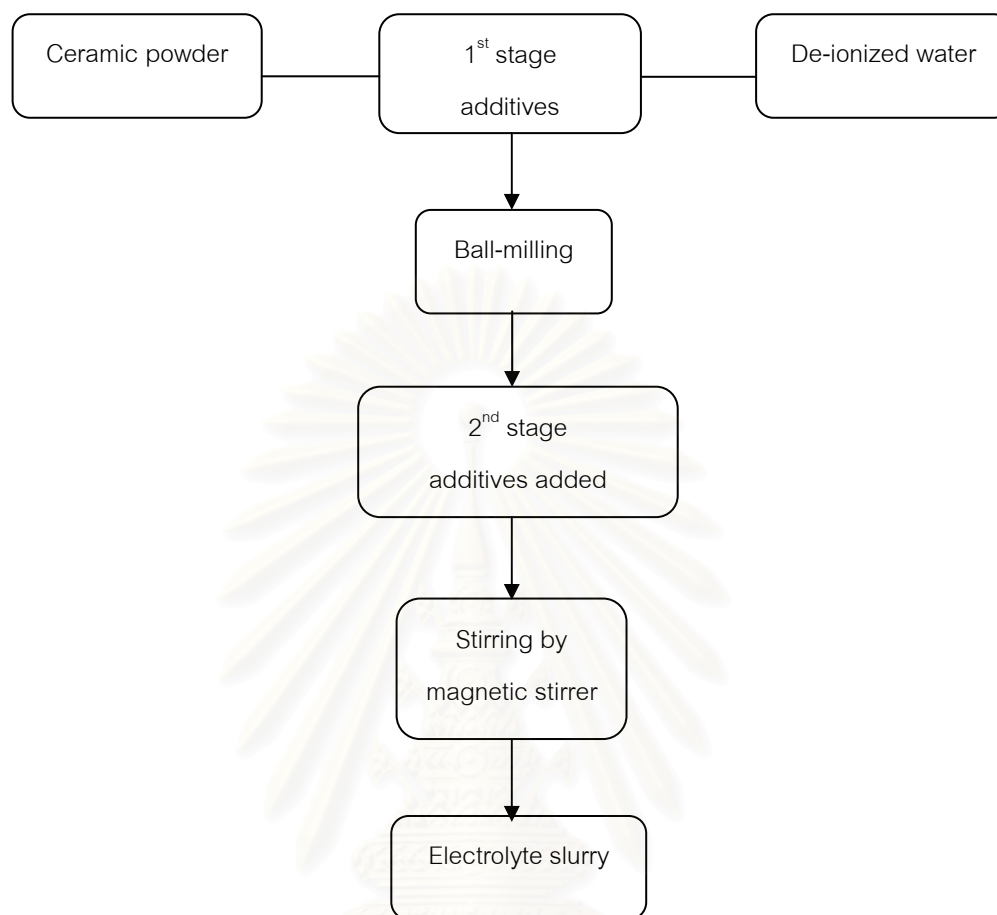


Fig. 3.2 The step of electrolyte slurry preparation

### 3.3 Rheology of electrolyte slurry

Rheological properties of aqueous tape casting slurries are strongly affect the tape casting process and the quality of the final product. To determine the rheology behavior of the slurry, the Brookfield viscometer, DY II<sup>+</sup> was used to measure the slurry viscosity by using the rotational method and results will be shown later in chapter 4.

### 3.4 Tape casting

After stirring, the slurry was tape cast by a doctor blade tape casting machine (Iwatani International Corporation, D-150) using silicone-treated polyester tape (siPET) as a carrier film. The prepared electrolyte slurry was poured into the caster cavity as shown in Fig. 3.3 then, the machine was turned on and the slurry moved along the carrier film as in Fig. 3.4. The moving speed can adjust between 0 to 80 cm/min, and the speed used in this study was 40 cm/min.

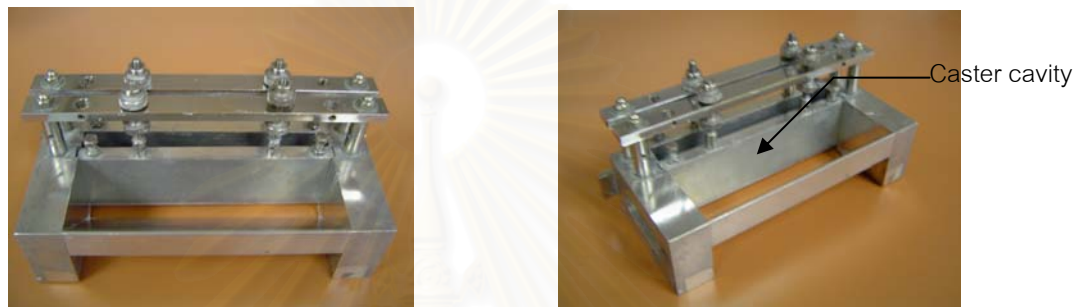


Fig. 3.3 Tape caster head

The thickness of green tape can be adjusted by the 4-dial gauges attached to the casting head (Fig. 3.4). After slurry was cast, the green tape was left on the machine to dry at ambient atmosphere for 6-12 hours or overnight. Then, the green tapes were peeled off from the carrier film and cut to the required dimensions and further proceed to de-binding and sintering process.

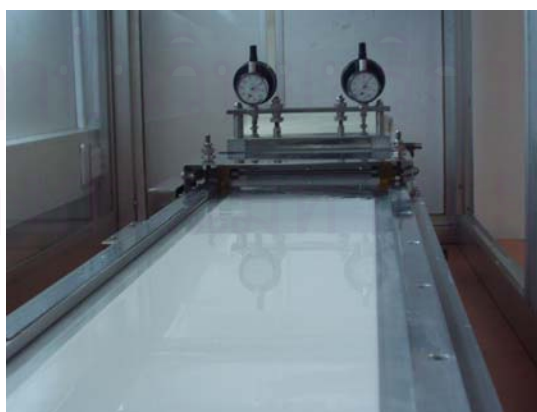


Fig. 3.4 Tape casting machine with the electrolyte slurry casting



### 3.5 De-binding and sintering conditions

Since the compositions of green tapes were typically contained high volume percent of polymers, i.e. binder, plasticizers, i.e. (~40%), therefore the process of getting rid of the binders or debinding shall be considered as critical factors for sintering process.

The electrolyte green tapes were initially heating up at a slow ramp rate of  $100^{\circ}\text{C}/\text{h}$  and soaking at  $270^{\circ}\text{C}$  for 30 minutes. This should allow all organic polymer to evaporate slowly before burning away at  $600^{\circ}\text{C}$ . Then, the program was set to sinter in air at heating rate of  $150^{\circ}\text{C}/\text{hr}$  and finally, the samples were cooled down at the rate of  $300^{\circ}\text{C}/\text{hr}$ . The sintering temperature was at  $1400^{\circ}\text{C}$  for 2 hrs,  $1450^{\circ}\text{C}$  for 2 hrs and  $1450^{\circ}\text{C}$  for 4 hrs in order to study the influence of the sintering conditions to the microstructure and the ionic conductivity of the electrolyte tape.

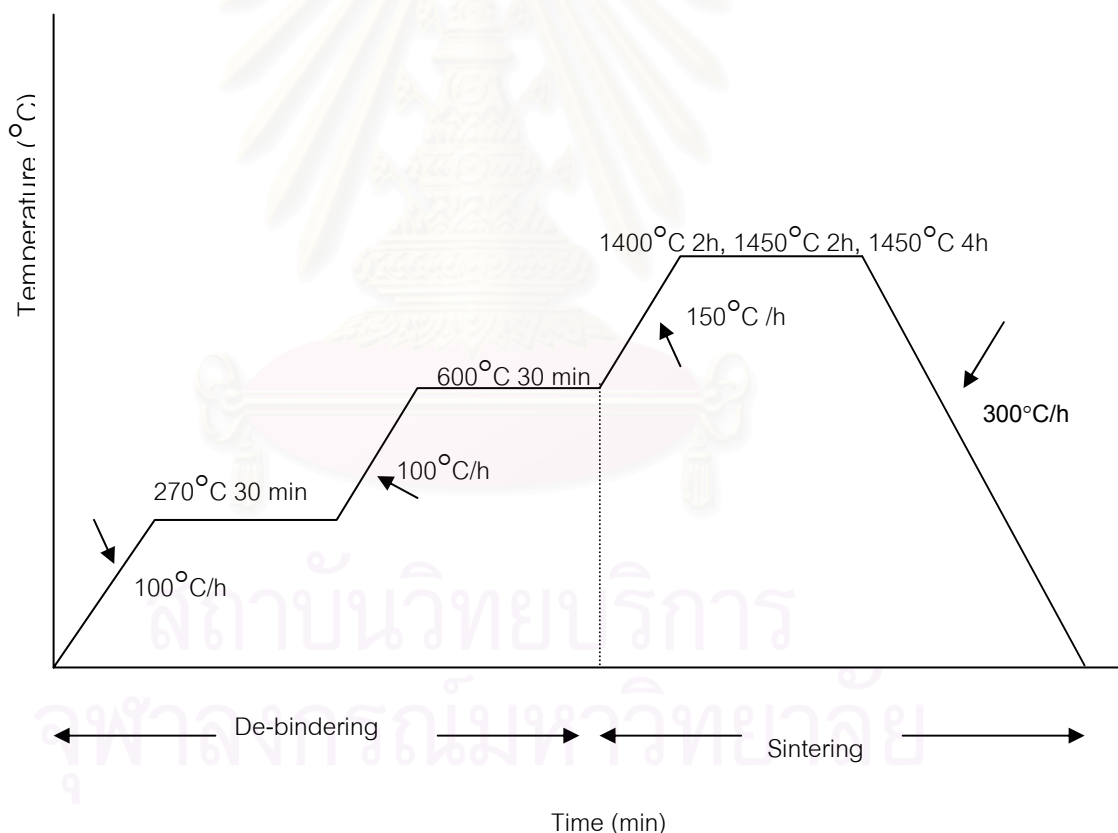


Fig. 3.5 A schematic diagram of de-binding and sintering programme

### 3.6 Characterization techniques

#### 3.6.1 Phase and crystal structure

The phases and crystal structures of electrolyte tapes as well as sintered powders were investigated by X-ray diffractometer which used  $\text{CuK}\alpha$  radiation ( $\text{CuK}\alpha$ ; JEOL: JDX-3530). The samples were scanned using  $2\theta$  range of  $5\text{-}100^\circ$  with  $0.04$  degree for step angle, and  $0.5$  second/step for count time; similar conditions were used for the sintered tapes.

#### 3.6.2 Microstructural evaluation

Before the microstructure investigation, the sintered specimens were gold coated for 120 seconds using current  $15$  mA by sputtering instrument (JEOL:JFC-1200). Then, the microstructure were examined by scanning electron microscopy (JEOL:JSM-6301F) for  $5,000\times$  and  $15,000\times$  magnifications.

#### 3.6.3 Electrical Measurement

Electrolyte material for SOFC component needs to have high ionic conductivity since it involves the movement of oxygen ions ( $\text{O}^{2-}$ ) vacancies, and it is temperature dependent. The ionic conductivity of the sintered tapes and pellets were measured from  $275$  to  $600^\circ\text{C}$  in air by means of two-probe impedance spectroscopy. AC impedance measurements were performed with a computer controlled Solartron 1260 Impedance /Gain-Phase Analyzer over the initial frequency of  $10$  MHz to the final frequency of  $0.05$  Hz with an applied signal of  $30$  mV illustrated in Fig. 3.6.

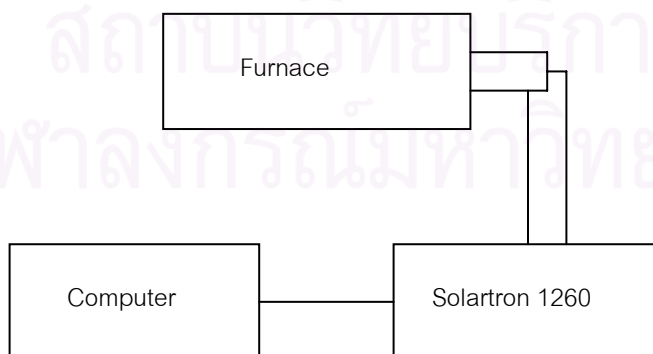


Fig. 3.6 A schematic diagram of control an measurement apparatus for the AC impedance spectroscopy

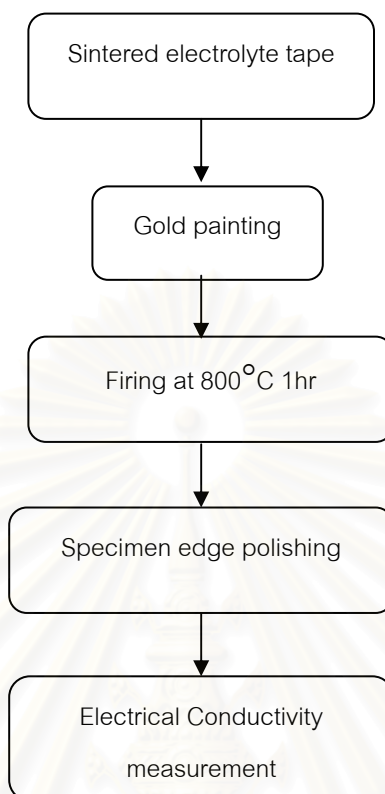


Fig. 3.7 Preparation specimen for electrical measurement

Two platinum meshes were used as the terminal electrodes applied to both sides of the samples before putting into the furnace. The flow chart of specimen preparation for electrical conductivity measurement is shown in Fig. 3.7.

After the ionic conductivity measurement, the specimens that had good value will be repeated in order to investigate influence of the sintering to the ionic conductivity. The reproduced batches started at the ceramic slurry preparation through the electrical property measurement as the flow chart in Fig. 3.8.

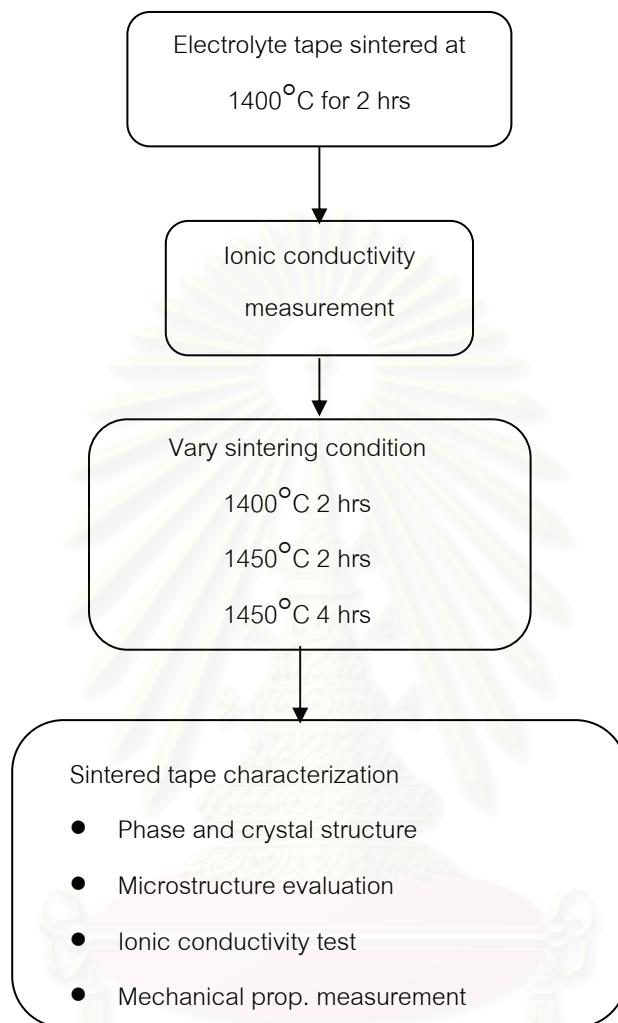


Fig. 3.8 A flow chart of the repeat loop of electrolyte tape investigation

### 3.6.4 Thermal expansion Measurement

Since the electrolyte material for SOFC components will later be integrated into a cell structure with other electrodes, therefore, the thermal expansion behavior is also critical to get the value matching with both anode (NiO/YSZ) and cathode (LSM-based) materials.

A dilatometer, Anter Unitherm Model 1161 (from the Department of Science Service, Ministry of Science and Technology) was used to determine the thermal expansion coefficient of

the sintered specimens. The sample were prepared in rectangular bars by uniaxially press at 1000 psi with the dimension of 5x30x5 mm and then sintered at 1400°C for 2 hr. The principle of dilatometer is to measure the changing of sample length compared to the changing of increased temperature. In this evaluation used heating rate of 3°C/ min and measured at temperature range from 50°C to 1000°C.

### 3.6.5 Mechanical property Measurement

The electrolyte is a critical component of the stack, particularly in the planar designs with self-supporting electrolyte membranes. Then the mechanical properties were measured on the samples whose ionic conductivity had been favorable. A Universal Testing Mechine, Instron 4502 was used to measure the three-point bending strength at room temperature with a cross-head speed of 0.5 mm/min on a rectangular sample of dimension 50x10x 0.15 mm<sup>3</sup>.



สถาบันวิทยบริการ  
จุฬาลงกรณ์มหาวิทยาลัย

## Chapter 4

### Results and Discussion

This chapter will be divided into four main sections. The first section will be the results on electrolyte powder characterizations, including particle size and size distribution, XRD and SEM study followed by the rheology of the electrolyte slurry and, the physical property of the electrolyte green tape. The last section will address the characterizations of the sintered electrolyte including phase and crystal structure study by XRD, and microstructure evolution by SEM. The mechanical property and thermal expansion measurement are also reported in this section.

#### 4.1 Electrolyte powders Characterization

##### 4.1.1 Particle size and size distribution

Ceramic powders are always produced synthetically in order to control the chemical composition and microstructure. In the context of tape casting, the starting powder needs to be characterized to determine their sizes, their shapes, and their size distributions. Results on particle size and size distribution of all the starting powders used in this study will be shown in Table 4.1. The laser particle-sized analyzer, (MALVERN instruments: mastersizer-S) was used to determine the particle size analysis.

From results Table 4.1, the average particle sizes of the YSZ starting powders obtained commercially were in the suitable range for processing by tape casting. The partially stabilized (tetragonal) zirconia had the average size of 0.41  $\mu\text{m}$ , whereas the fully stabilized (cubic fluorite) zirconia for 8 and 10 mol% doped had the average particle size between 0.37 and 0.45  $\mu\text{m}$ . Previous investigation by Hellebrand [1996] <sup>[33]</sup> reported the appropriate particle size for tape casting fabrication should be within 0.3-0.5  $\mu\text{m}$ . All powders have a single modal distribution except 8 mol% doped  $\text{Y}_2\text{O}_3$  for Tosoh, spray-dried powder, has bi-modal distribution and the average particle size is 0.97  $\mu\text{m}$ . For ceria-based powders which were prepared in this study by mixed-oxide route showed bigger particle size than zirconia-based. The average particle size of ceria is 13.4  $\mu\text{m}$ , while GDC powders are approximately at 3.0-4.4  $\mu\text{m}$  with tri-modal distribution.

**Table 4.1 Particle size and size distribution of the starting powders**

Starting Powder	Average particle size ( $\mu\text{m}$ )	Size Distribution
3YSZ (MEL)	0.41	Single modal (see Appendix B)
8YSZ (MEL)	0.37	Single modal
8YSZ (Tosoh)	0.97	Bi-modal
8YSZ (Daiichi)	0.39	Single modal
10YSZ (MEL)	0.41	Single modal
10YSZ (Daiichi)	0.39	Single modal
Ceria (Alfa Aesar)	13.39	Tri-modal
GDC 10 mol% (mixed-oxide)	3.33	Tri-modal
GDC 20 mol% (mixed -xide)	4.33	Tri-modal

#### 4.1.2 X-ray diffraction Study

All YSZ powders used in this study were also characterized for mineral phase and crystal structure in order to confirm the supplier's specifications by X-ray diffraction. From the XRD patterns, the starting powders were fully stabilized (cubic fluorite phase) for 8 and 10 mol% YSZ and partially stabilized (tetragonal combined with monoclinic phase) for 3 mol% YSZ. Ceria powder from commercial supply and GDC powder from mixed-oxide route also showed the cubic phase. The X-ray spectra of all YSZ commercial powders and ceria-based powders used for fabrication of SOFC electrolytes are shown in Fig. 4.1-4.6.

The purity of the starting powders had been carefully considered in order to avoid the detrimental effects on the total conductivity. In polycrystalline ceramic the conductivity of grain boundaries and bulk contribute to overall conductivity. In case of polycrystalline YSZ, its unusually high intrinsic (bulk) conductivity of the grain boundaries is far less than the crystal, basically by a factor of  $\sim 100$ .<sup>[34]</sup> The effects of grain boundaries to the total conductivity will depend on grain size and impurity content (e.g. silica), since impurities tend to concentrate at the grain boundaries. More discussions on electrical conductivity will be found in later session.



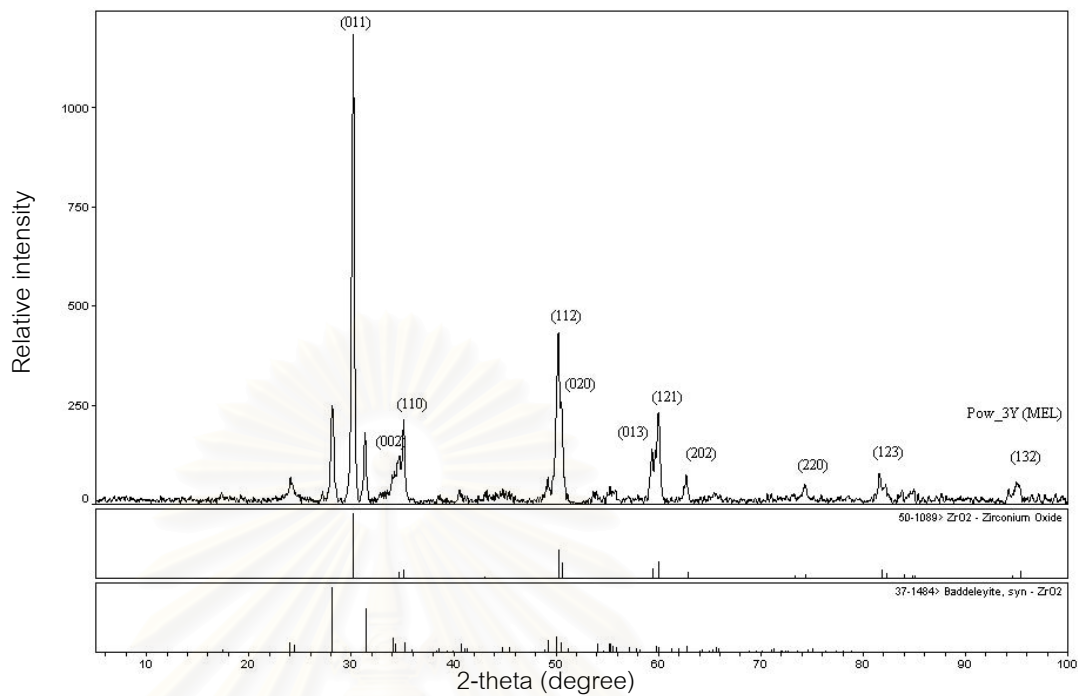


Fig. 4.1 XRD patterns of as-received 3YSZ powder (Tetragonal)

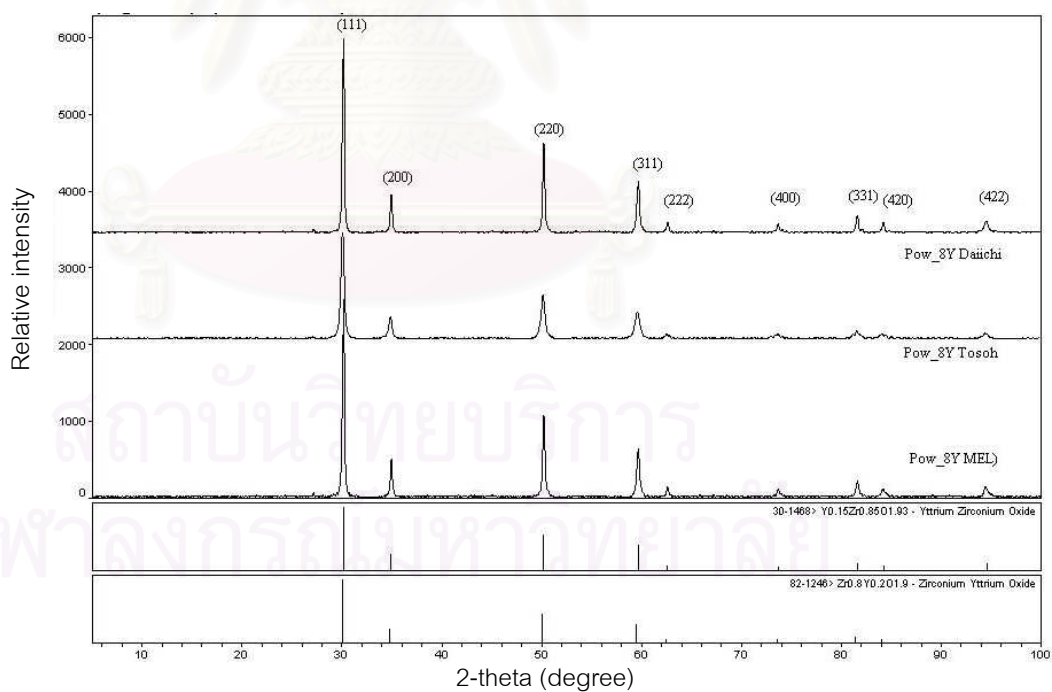


Fig. 4.2 XRD patterns of as-received 8YSZ powder from various sources (cubic fluorite)

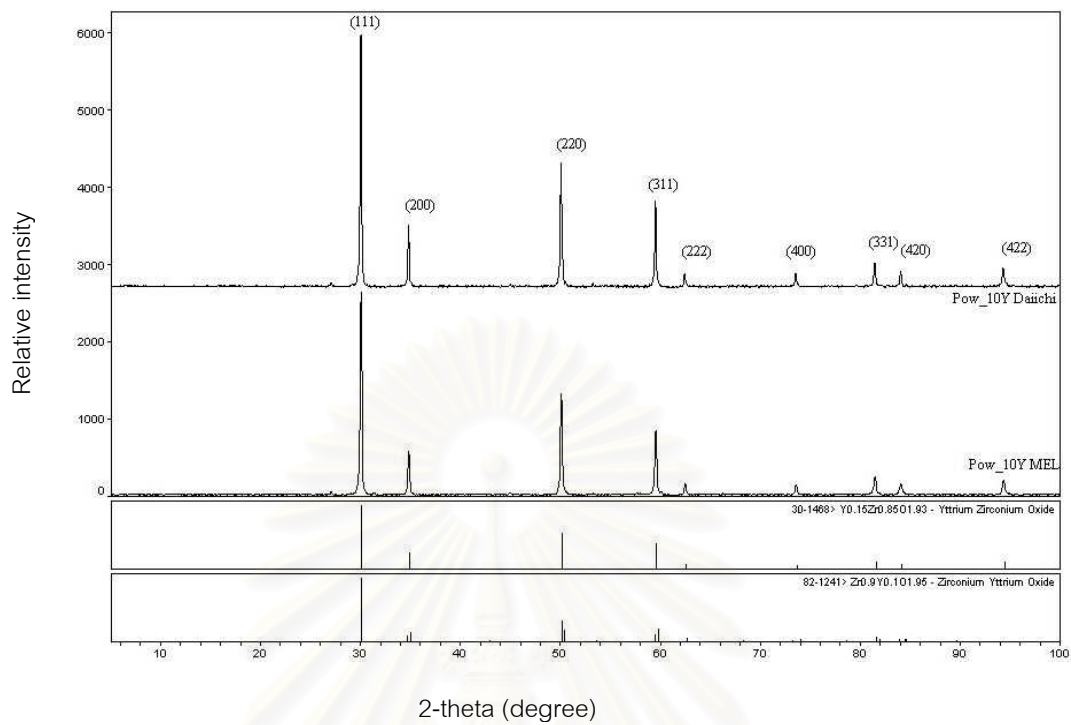


Fig. 4.3 XRD patterns of as-received 10YSZ powders from various sources(cubic fluorite)

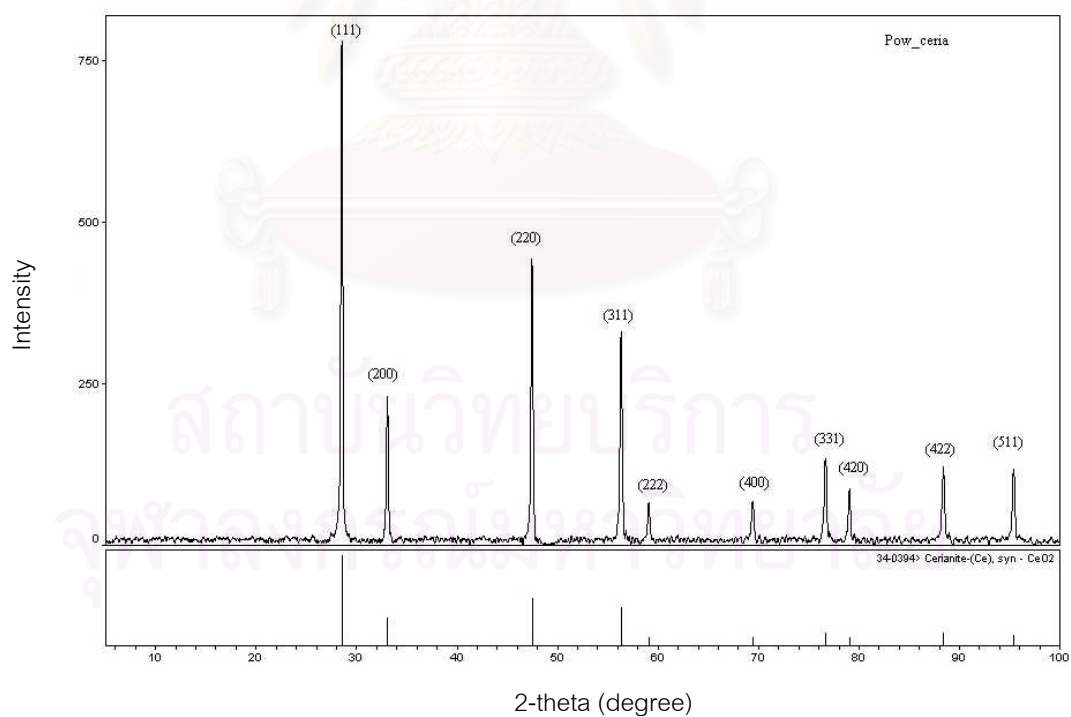


Fig. 4.4 XRD pattern of as-received Ceria powders from Alfa Aesar (cubic fluorite)

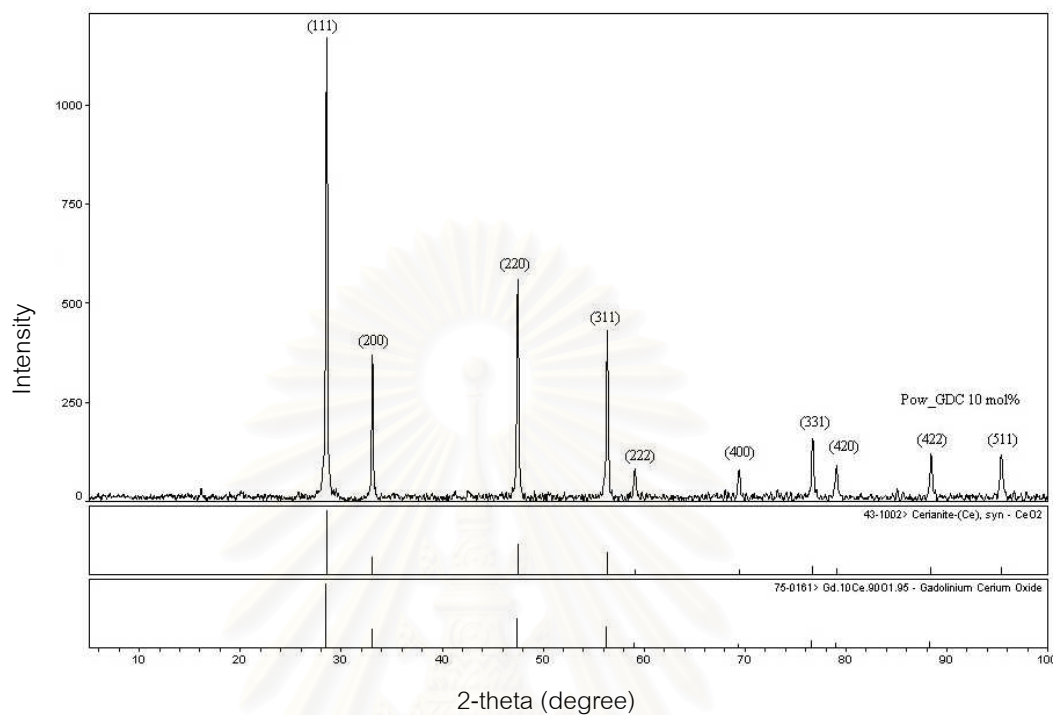


Fig. 4.5 XRD pattern of as-received GDC (10 mol%) powders from mixed-oxide route (cubic fluorite)

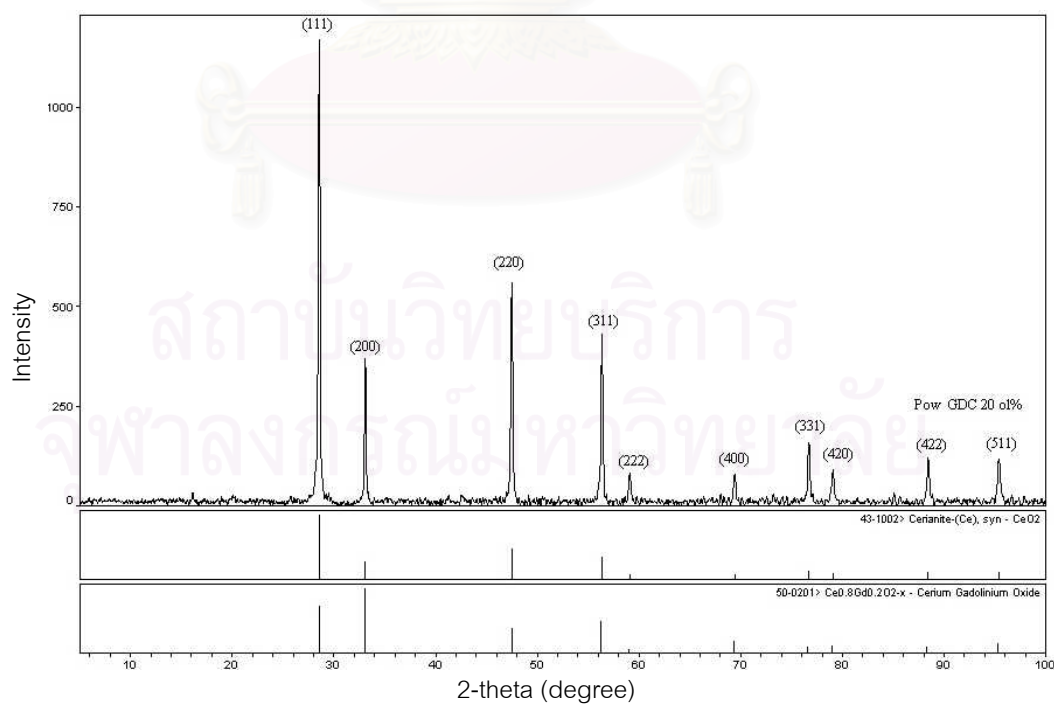


Fig. 4.6 XRD pattern of as-received GDC (20 mol%) powders from mixed-oxide route (cubic fluorite)

### 4.1.3 SEM study

In order to determine the particle shapes and identify the agglomeration of the as-received commercial powders before fabricating them by tape-casting, the high magnification SEM images were performed on the powders and results are shown in the following figures.

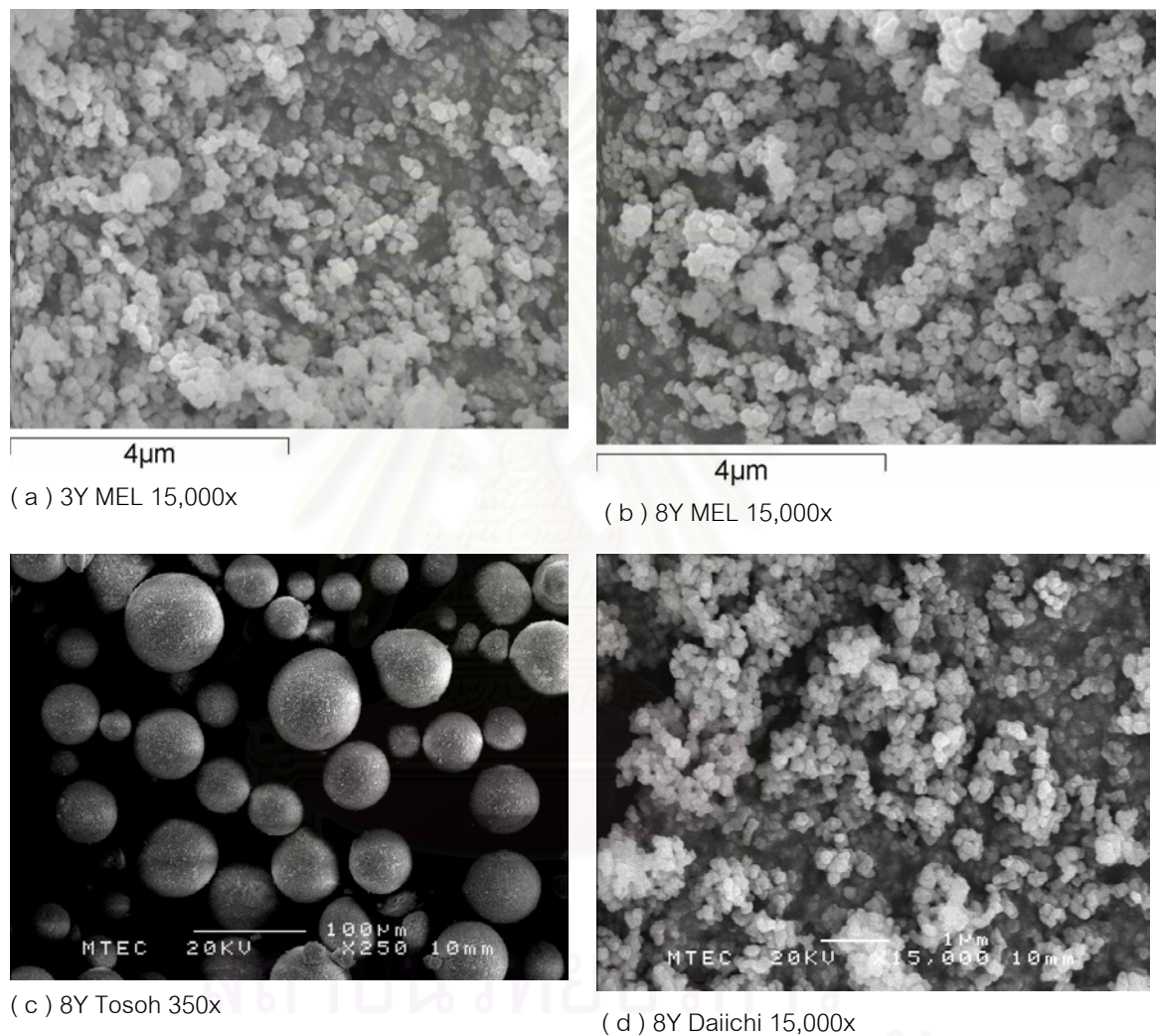


Fig. 4.7 SEM micrographs of as-received commercial powder ( a ) 3 mol% $\text{Y}_2\text{O}_3$  doped  $\text{Zr}_2\text{O}_3$  from MEL, (b) 8 mol%  $\text{Y}_2\text{O}_3$  doped  $\text{ZrO}_2$  from MEL, ( c ) 8 mol% $\text{Y}_2\text{O}_3$  doped  $\text{ZrO}_2$  from Tosoh, ( d ) 8 mol% $\text{Y}_2\text{O}_3$  doped  $\text{ZrO}_2$  from Daiichi, Japan



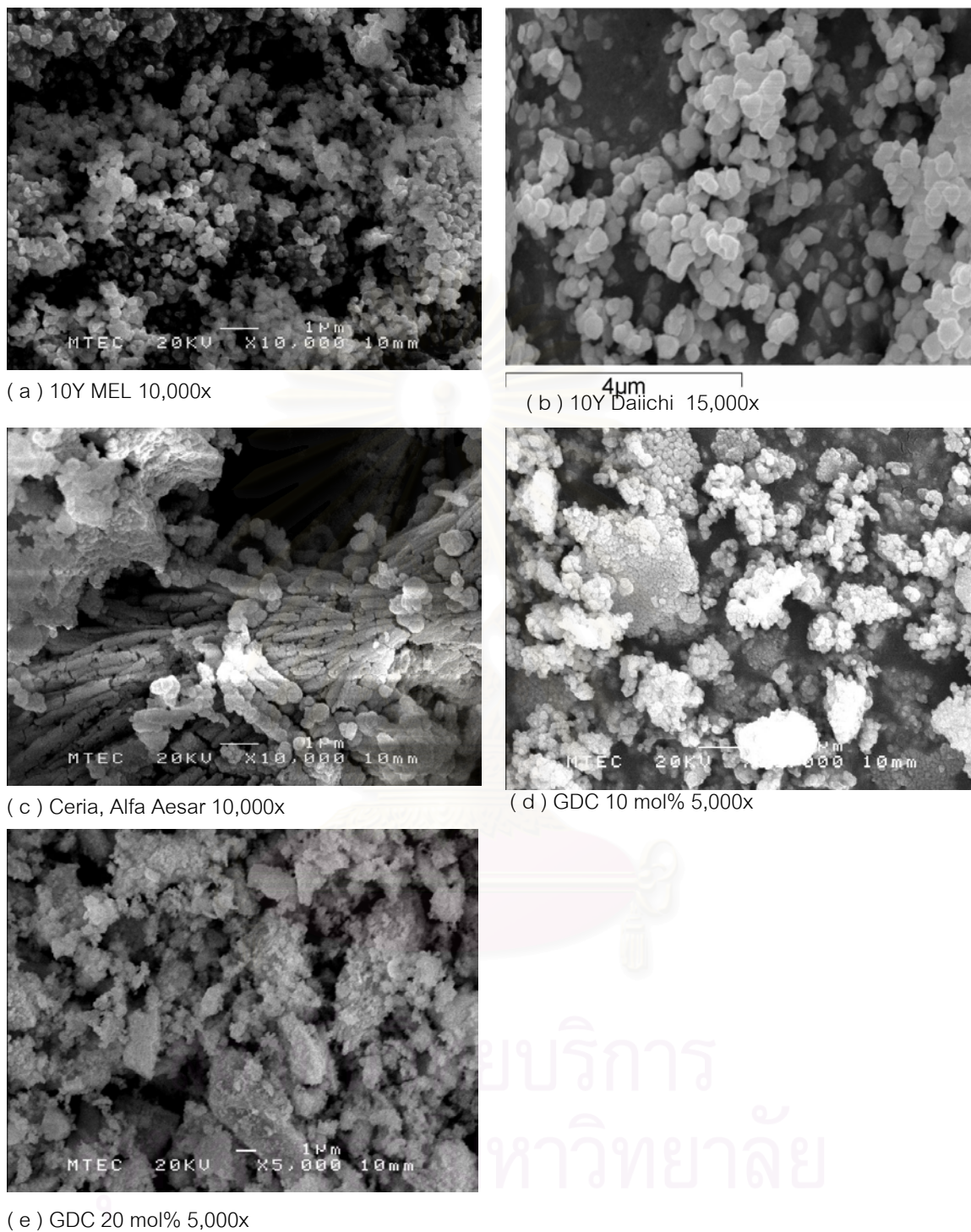


Fig. 4.8 SEM micrographs of as-received commercial powders for 10YSZ and Ceria and GDC 10-20 mol% ( a ) 10 mol% $\text{Y}_2\text{O}_3$  doped  $\text{ZrO}_2$  from MEL, ( b ) 10 mol% $\text{Y}_2\text{O}_3$  doped  $\text{ZrO}_2$  from Daiichi, ( c ) Ceria powder from Aesar, ( d ) GDC 10 mol% doped from mixed oxide route, ( e ) GDC 20 mol% doped from mixed-oxide route.

From SEM results, it is evident that all the commercial powders have rather different characteristics, MEL and Daiichi powders appeared to have uniform spherical shape in sub-micron sizes, and some powder agglomerations were clearly found. Tosoh spray-dried powder (8YSZ) has a very spherical shape and uniform size in a range of 5-100 microns. No agglomeration was found in Tosoh powder. For ceria and GDC powders, which were prepared by mixed-oxide route, the agglomerations were found to a certain extent. The average particle sizes from the image were in the range of 3-15 microns.

#### 4.2 Rheology of electrolyte slurry

Preparing a tape-casting slurry process begins with milling or mixing the ceramic powder with liquid media, which water was used throughout this study. Ball milling was used in order to break up the particle agglomerates and wetting the powders. Therefore, the slurry should contain only the ceramic powder, solvent (water, in this study) and the dispersing agents. During milling process, the dispersing agents will have enough time to occupy most of the active sites on the powder surfaces, which is required for their optimum efficiency. The milling time used in this study was about 12-16 hrs in order to achieve stable conditions and high homogeneity to provide the suitable viscosity ( $\eta < 1000$  mPa.s).

Some formulations of electrolyte slurries were chosen for the viscosity measurement in order to determine the slurry characteristics. The rheology behaviors of all selected electrolyte slurries were determined by Brookfield Viscometer, DY II<sup>+</sup> at MTEC and the results were shown in the following Table 4.2. The viscosity measurement was performed under shear rate ranging from 10-200 rpm. Table 4.2 showed the viscosity measurement reading at 160 rpm.

Table 4.2. Measurement of viscosity of electrolyte slurries by Brookfield viscometer

Batch	Powders	Viscosity (centipoise)	Characteristics of slurries
P13R	3YSZ (MEL)	298.4	Pseudo-plastic
P19R	8YSZ (MEL)	161.6	Pseudo-plastic
P21R	8YSZ (Tosoh)	168.4	Pseudo-plastic
P20R	10YSZ (MEL)	107.8	Pseudo-plastic
P9R	10YSZ (Daiichi)	55.6	Pseudo-plastic
P29	3Y+ 8YSZ (MEL)	134.1	Pseudo-plastic

The appropriate viscosity for water-based slurries used in this study was in the range of 55-300 centipoise. The viscosity varied depending upon the working principle of casting instruments and the desired thickness of the green tape. In addition, the slurry with pseudo-plastic behavior found to be well-cast in this study.

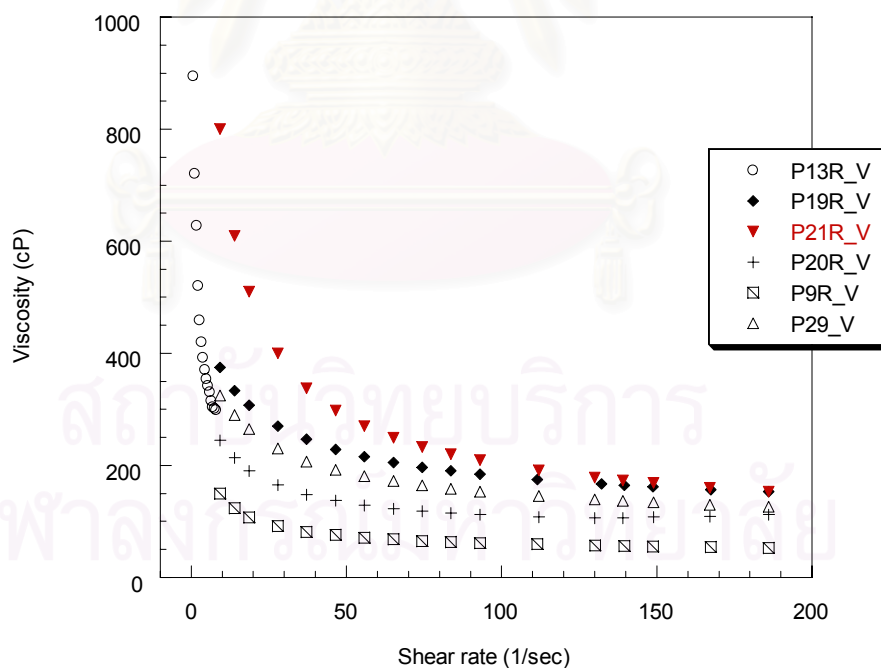


Fig. 4.9 Rheology behaviors of the electrolyte slurries



Fig. 4.9 showed the plot between viscosity and shear rate of the pseudo-plastic behavior of electrolyte slurries. The viscosity of the slurry decreased with increasing shear rate, this is called shear-thinning behavior. The slope of the viscosity versus shear rate curve is very steep—this means that small changes of shear rate influenced in a big change of viscosity.

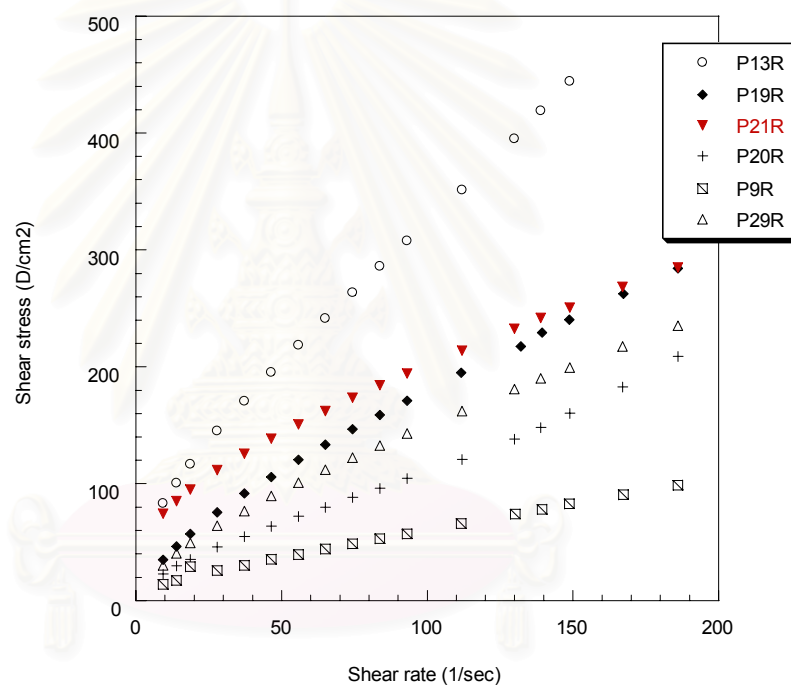


Fig. 4.10 Flow characteristics of electrolyte slurries

Fig. 4.9 and Fig. 4.10 illustrated the pseudo-plastic behavior of electrolyte slip, which is desirable in tape casting process, in order to make the slurry flowed instantly when casting but showed little or no flow after casting, therefore it could maintain the required cast shape.

### 4.3 Physical property of electrolyte green tape

The physical appearance of reproduced-batch tape-cast specimens, including the batches and compositions studied was reported in the following Table 4.3. In addition, the percentage of organic contents in each tape were determined by de-binding the green tape at 600°C for 1 hour and determine the weight loss, then back calculate the % of organic contents in the tape by this formula:

$$\% \text{Organic Content} = (\text{Wt. Loss after de-binding} / \text{Wt. of tape after de-binding}) \times 100 \quad (4.1)$$

Table 4.3. Electrolyte batches and physical appearance of the green tape

Batch/Powder Type	Physical Appearance	%Organic Content	Shrinkage at 1450°C 2h	Shrinkage at 1450°C 4h
Po(Obtained Commercial Tape)	Smooth surface, no crack, no pin hole	12.22	9.46	14.4
P13R / 3Y MEL	Smooth surface, no crack, no pin hole	15.13	13.85	14.22
P19R / 8Y MEL	Smooth surface, small crack at the edge of tape	16.13	14.65	14.82
P21R / 8Y Tosoh	Not smooth surface and have crow's foot cracking	14.35	15.03	18.18
P20R / 10Y MEL	Smooth surface, not good wetting	12.68	13.93	14.31
P9R / 10Y Daiichi	Smooth surface, not good wetting	15.87	9.20	11.34
P29 / 3Y + 8Y MEL	Smooth surface, good wetting	14.95	16.04	16.58

More data of the other batches are shown in Table B-1, Appendix B.

Table 4.3 showed the physical property of the reproduced batches, including the organic content percentage and the sintering shrinkage. In this investigation, the shrinkage of the sintered tapes were ranged from about 10 to 16% whereas the obtained commercial green tape had the value of ~10% shrinkage. Most of the tape appearance were smooth and showed good wetting property with the plastic substrate.

#### 4.4 Property and characterization of sintered electrolyte

##### 4.4.1 Phase and crystal structure study by XRD

In order to determine the phase and crystal structure of the sintered electrolyte, the green tapes were successively sintered at  $1400^{\circ}\text{C}$  for 2 hrs and  $1450^{\circ}\text{C}$  for 2 and 4 hrs, then the specimens were investigated by X-ray diffractometer. The XRD patterns of sintered specimens, 3YSZ (MEL), 8YSZ (from MEL and Tosoh), 10YSZ (MEL), Ceria and GDC 10 and 20 mol% doped were shown in the following figures. The patterns showed the pure phase of tetragonal structure for 3YSZ following JCPDS no.50-1089, and pure cubic phase for 8YSZ and 10YSZ following JCPDS no. 30-1468. The sintered ceria and GDC10-20 mol% samples (by dry pressing) were also investigated and the XRD patterns shown following the JCPDS no.43-1002, 75-0162 and 75,0163 respectively. They showed the cubic phase and did not have any evidence of impurity phase.

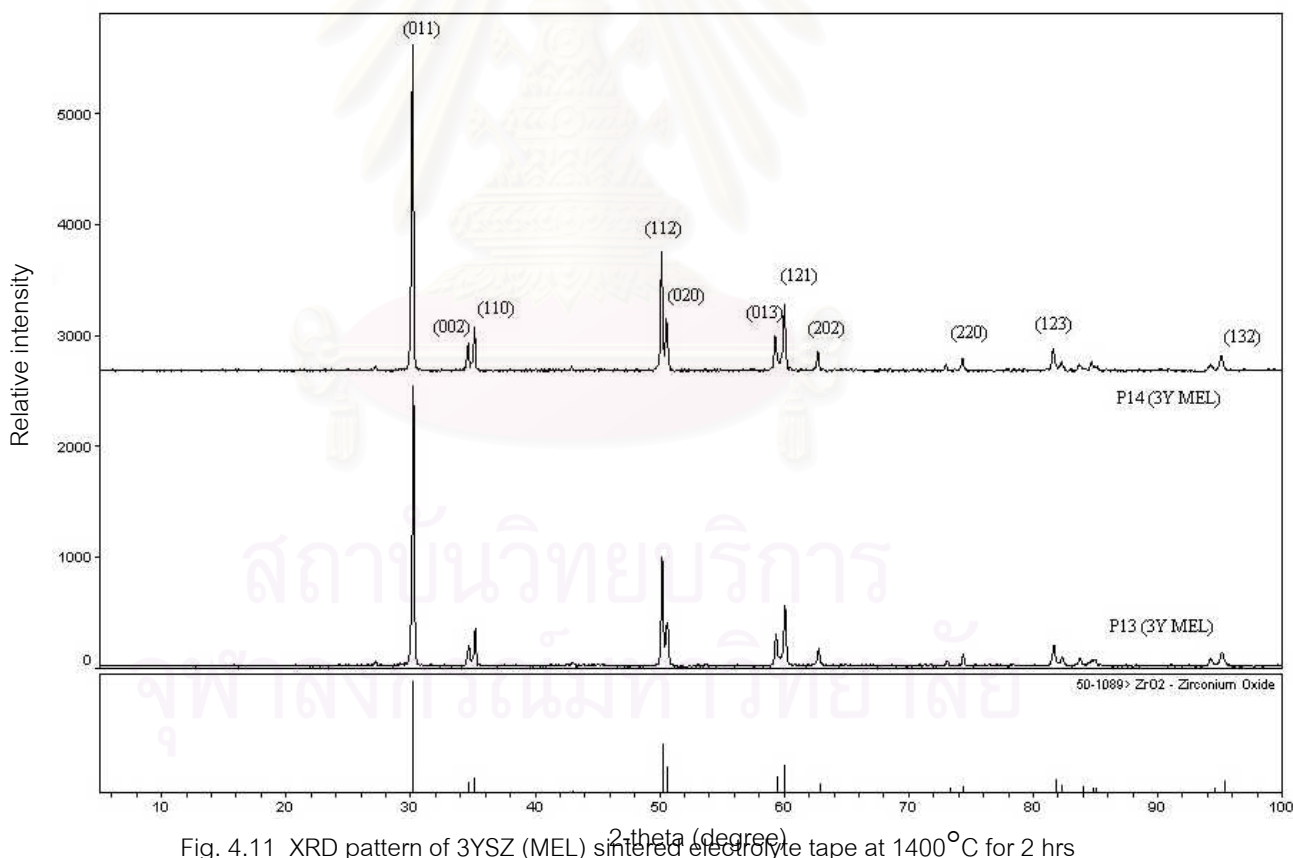


Fig. 4.11 XRD pattern of 3YSZ (MEL) sintered electrolyte tape at  $1400^{\circ}\text{C}$  for 2 hrs

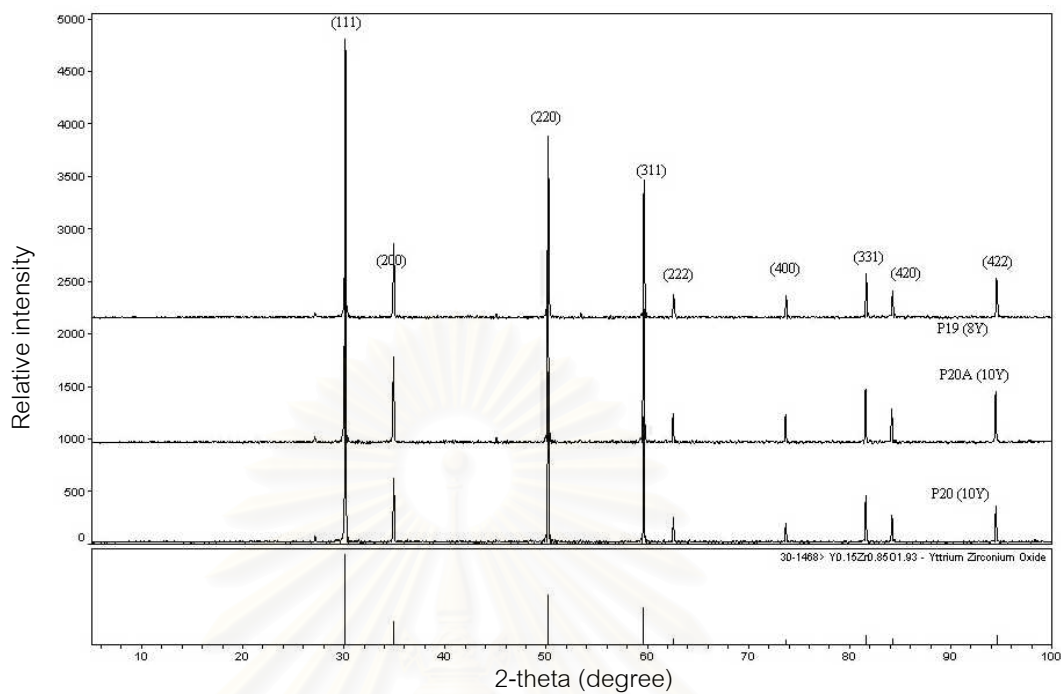


Fig.4.12 XRD patterns of 8YSZ and 10YSZ (MEL) sintered electrolyte tape at 1400°C for 2 hrs

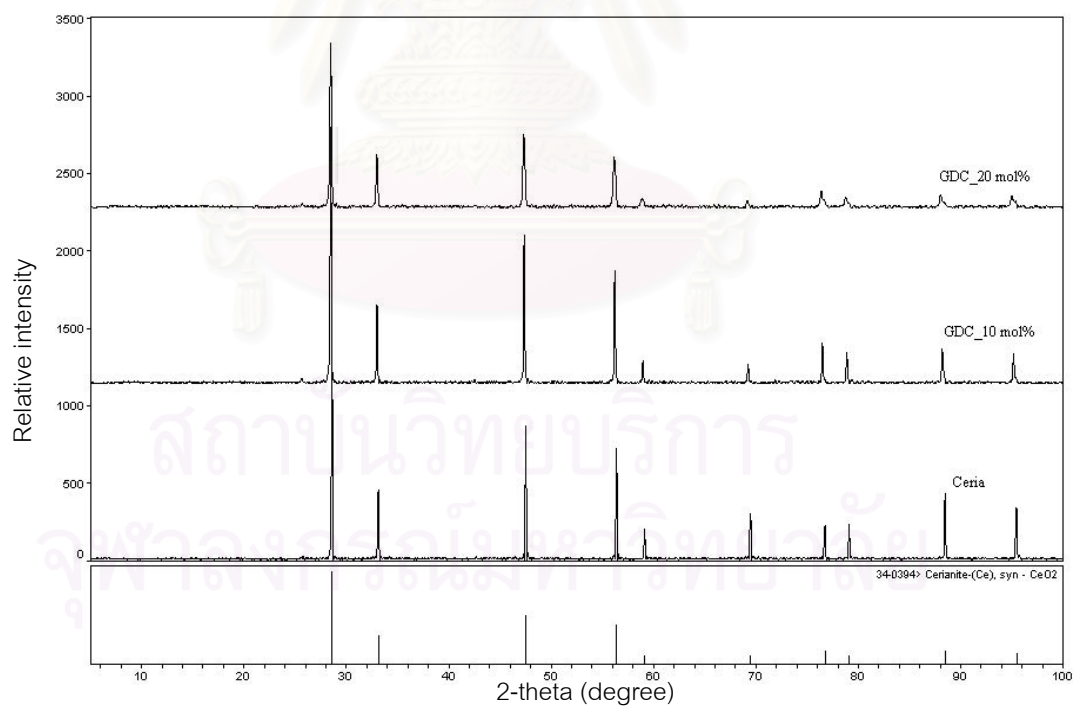


Fig. 4.13 XRD pattern of ceria-based electrolyte pellets sintered at 1450°C for 1 hour

After fabricating the electrolyte tapes, the selected batches of electrolyte, which were sintered at all three firing programs ( $1400^{\circ}\text{C}/2\text{ h}$ ,  $1450^{\circ}\text{C}/2\text{ h}$ , and  $1450^{\circ}\text{C}/4\text{ h}$ ) and were investigated phase and crystal structure. Figures below are some of the XRD patterns of the reproduced electrolytes.

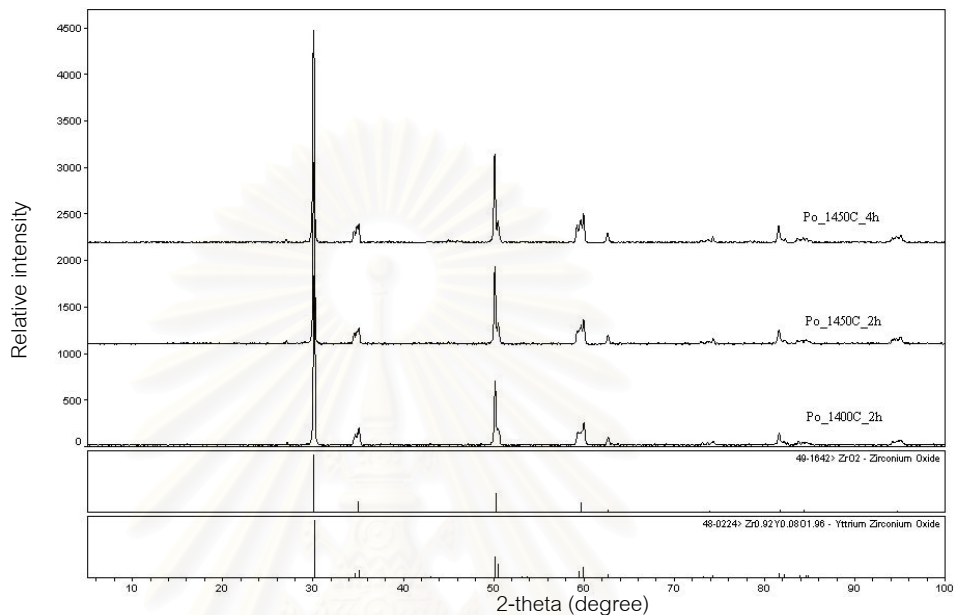


Fig. 4.14 XRD patterns of sintered electrolyte Po (obtained com. Tape) at  $1400^{\circ}\text{C}$  for 2 hrs and  $1450^{\circ}\text{C}$  for 4 hrs

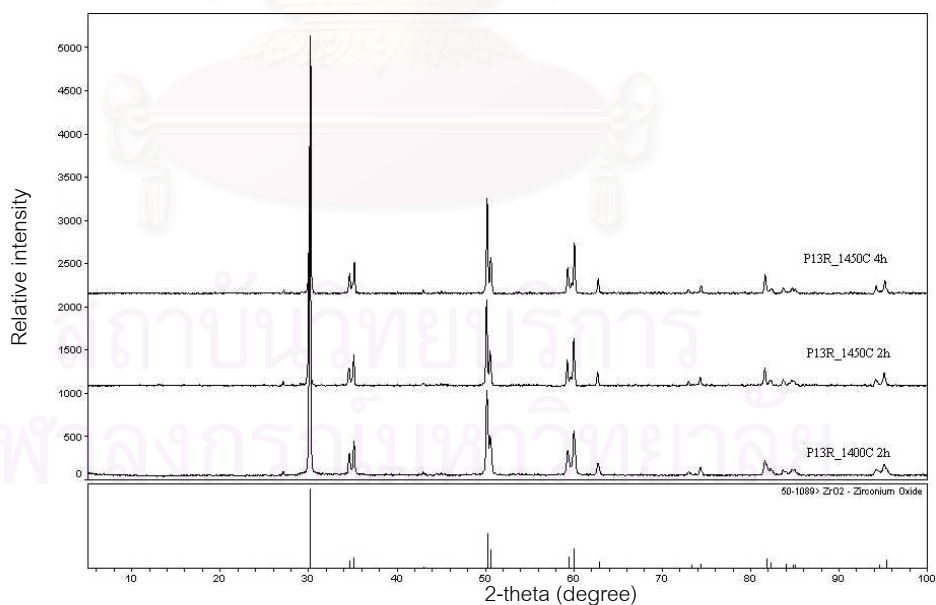


Fig. 4.15 XRD patterns of sintered electrolyte P13R (3YSZ, MEL) at  $1400^{\circ}\text{C}$  for 2 hrs and  $1450^{\circ}\text{C}$  for 4 hrs

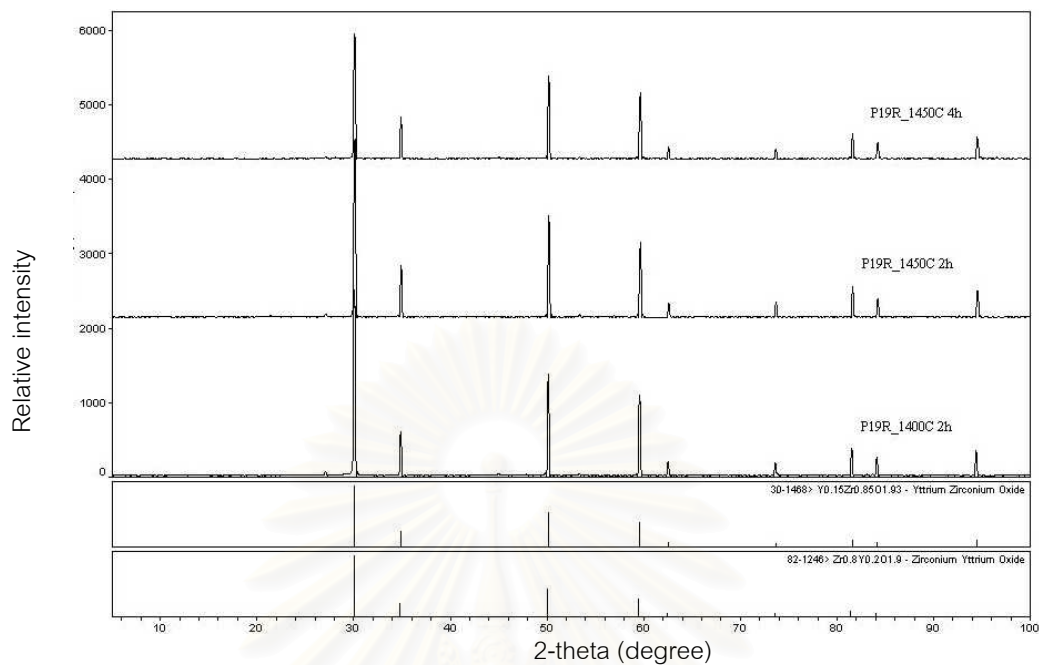


Fig. 4.16 XRD patterns of sintered electrolyte P19R (8YSZ, MEL) at 1400 and 1450°C for 2 hrs and 1450°C for 4 hrs

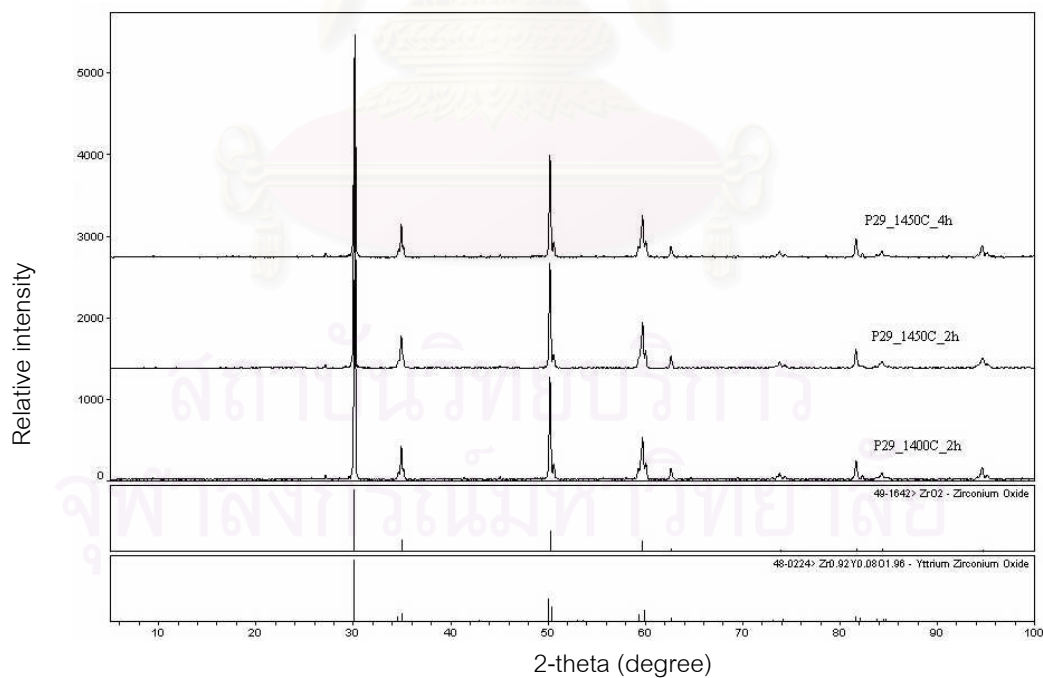


Fig. 4.17 XRD patterns of sintered electrolyte P29 (8YSZ + 3YSZ, MEL) at 1400 and 1450°C for 2 hrs and 1450°C for 4 hrs

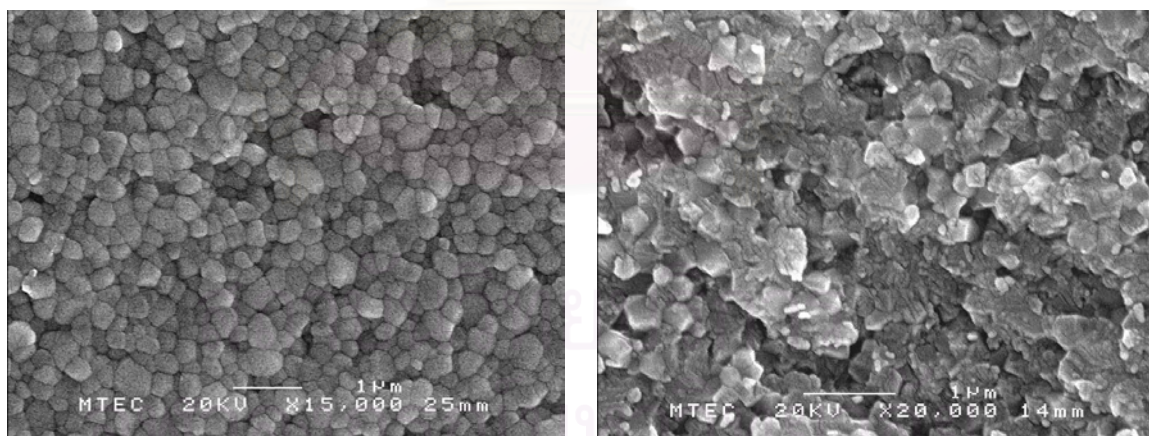


The X-ray spectra of the reproduced electrolyte tapes showed the tetragonal structure for 3YSZ and cubic structure for 8YSZ and 10YSZ as well as ceria-based electrolytes. No evidence of impurity phases were found in these XRD patterns.

#### 4.4.2 Microstructural Evaluation

To develop electrolytes for SOFC applications, study of the sintering and microstructure of the samples are very important for obtaining dense materials with higher ionic conductivity. In order to examine the microstructure of the sintered electrolyte, a field-emission scanning electron microscope (FESEM) was used. The electrolyte specimens were sintered at 1400°C for 2 hrs and gold-coated for 120 seconds before taking micrographs using the JEOL JSM-6301F microscope with a 30 KV accelerating voltage. The magnifications were varied from 5000 to 15,000x.

Fig. 4.18 showed the SEM micrographs of 3YSZ (MEL) electrolyte magnification of 15,000 and 20,000. The images showed very dense microstructure with only small porosity. The average grain size is about 0.4  $\mu\text{m}$ , the density of this specimens from calculation was 5.96  $\text{g}/\text{cm}^3$ , which was about 99.42% of theoretical density.



( a ) Surface of 3YSZ MEL

( b ) Fracture of 3YSZ

Fig. 4.18 SEM micrographs of sintered tape of 3YSZ, MEL (P13) sintered at 1400°C, 2h; ( a ) at the surface, ( b ) fractured surface



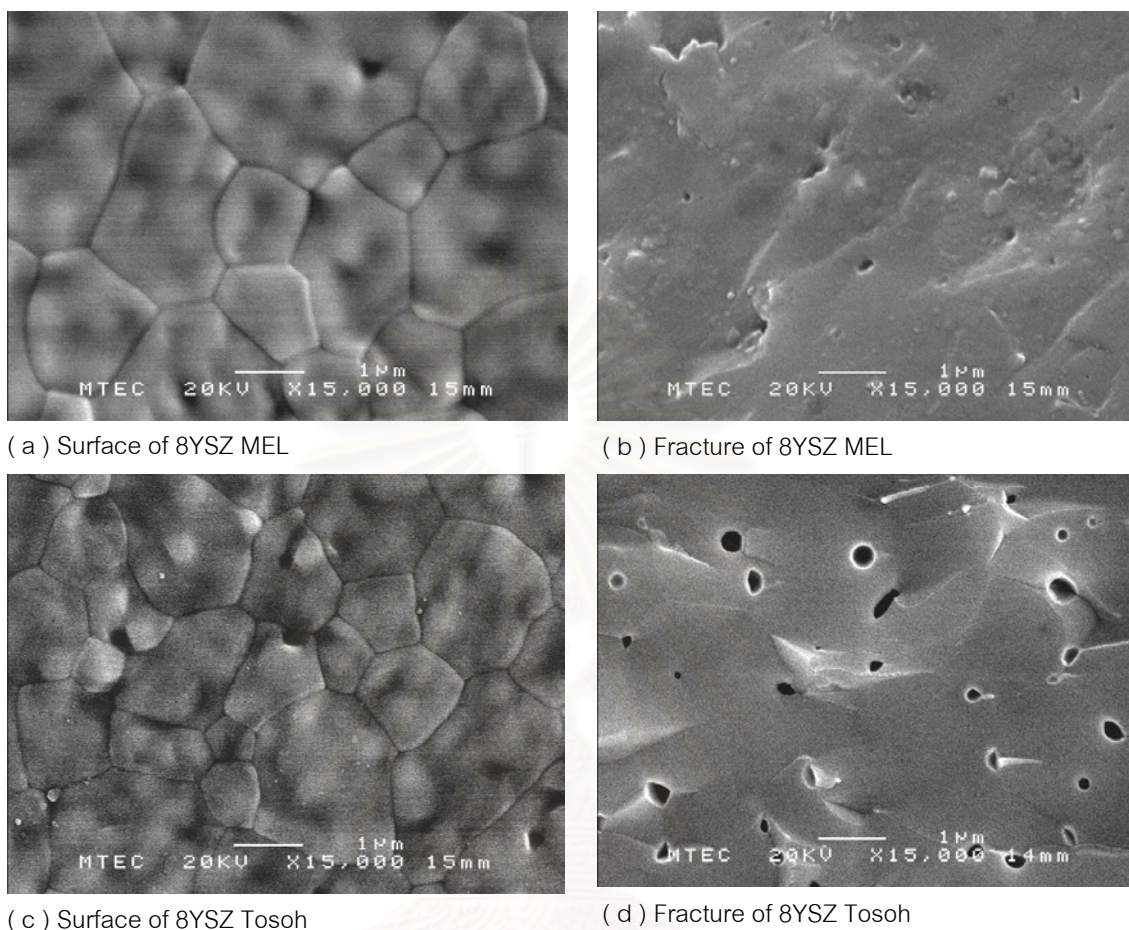


Fig. 4.19 8YSZ, MEL (P19) compared with 8YSZ, Tosoh (P21); ( a ) and ( b ) are surface and fractured surface of 8YSZ, MEL; ( c ) and ( d ) are surface and fractured surface of 8YSZ, Tosoh

Fig. 4.19 showed the SEM micrographs of 8YSZ, Tosoh electrolyte tape compared with 8YSZ, MEL electrolyte tape. The result showed that both sintered tapes ( $1400^{\circ}\text{C}$  2h) had equivalent grain size of about  $3\ \mu\text{m}$ . On the fractured surface, there were a few isolated pores at the grain boundaries. For 8YSZ from Tosoh, there were smaller pore sizes and in a less amount than MEL (8YSZ). In addition, the pore size of 8Y(MEL) electrolyte was in the range of  $\sim 0.2\text{-}0.4\ \mu\text{m}$ .

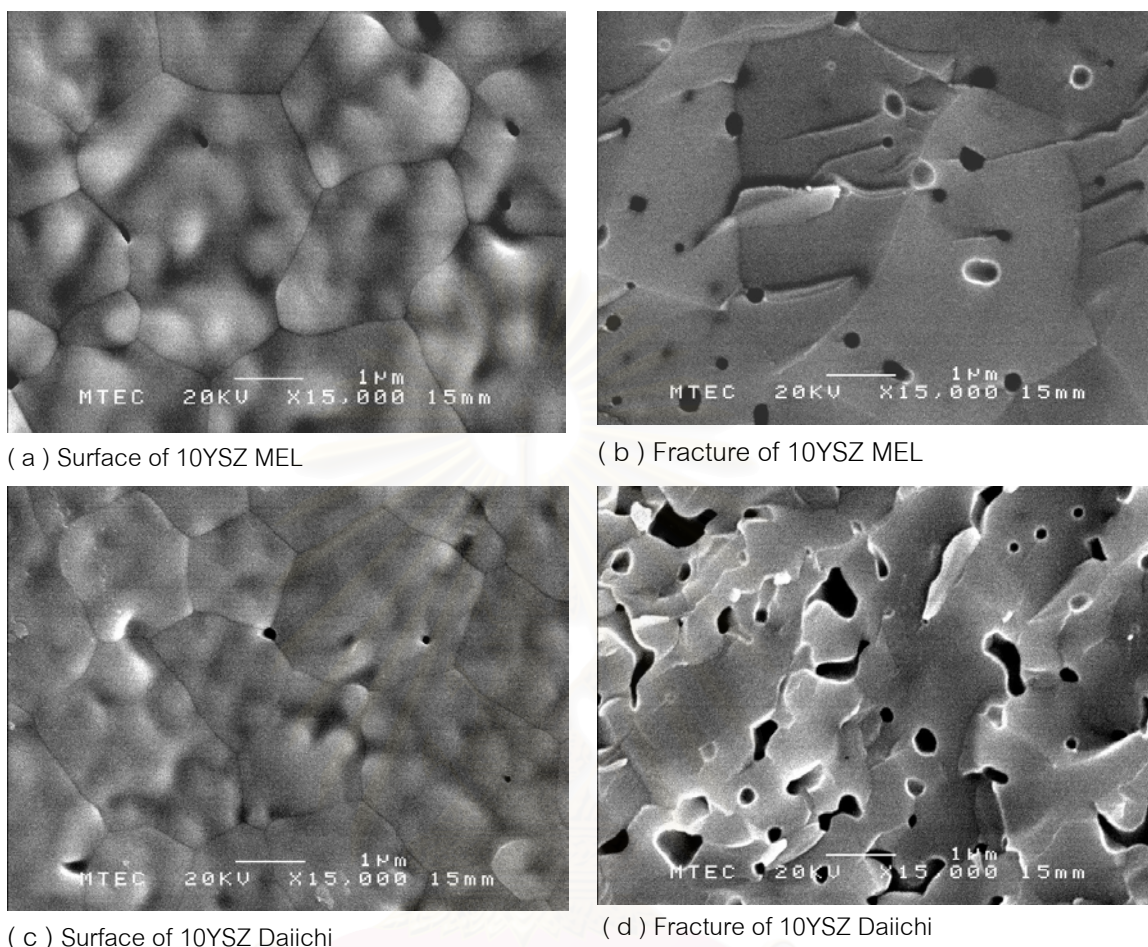


Fig. 4.20 10YSZ, MEL (P20) compared with 10YSZ, Daiichi (P9); ( a ) and ( b ) are surface and fractured surface of 10YSZ, MEL; ( c ) and ( d ) are surface and fractured surface of 10YSZ, Daiichi

Fig. 4.20 showed the SEM micrographs of 10YSZ, MEL electrolyte tapes (sintered at  $1400^{\circ}\text{C}$  for 2h) compared with 10YSZ, Daiichi electrolyte tapes. The results showed that both sintered tapes had equivalent grain sizes of about  $1\text{-}3\ \mu\text{m}$ , while 10YSZ from Daiichi electrolyte had the bigger pore sizes and some connected pore channels. The pore sizes of 10YSZ, MEL electrolyte were approximately  $0.2\text{-}0.3\ \mu\text{m}$ , while pore sizes of 10YSZ, Daiichi were about  $0.2\text{-}0.8\ \mu\text{m}$ . Moreover, both of them still had some pores at the grain boundary vertices.



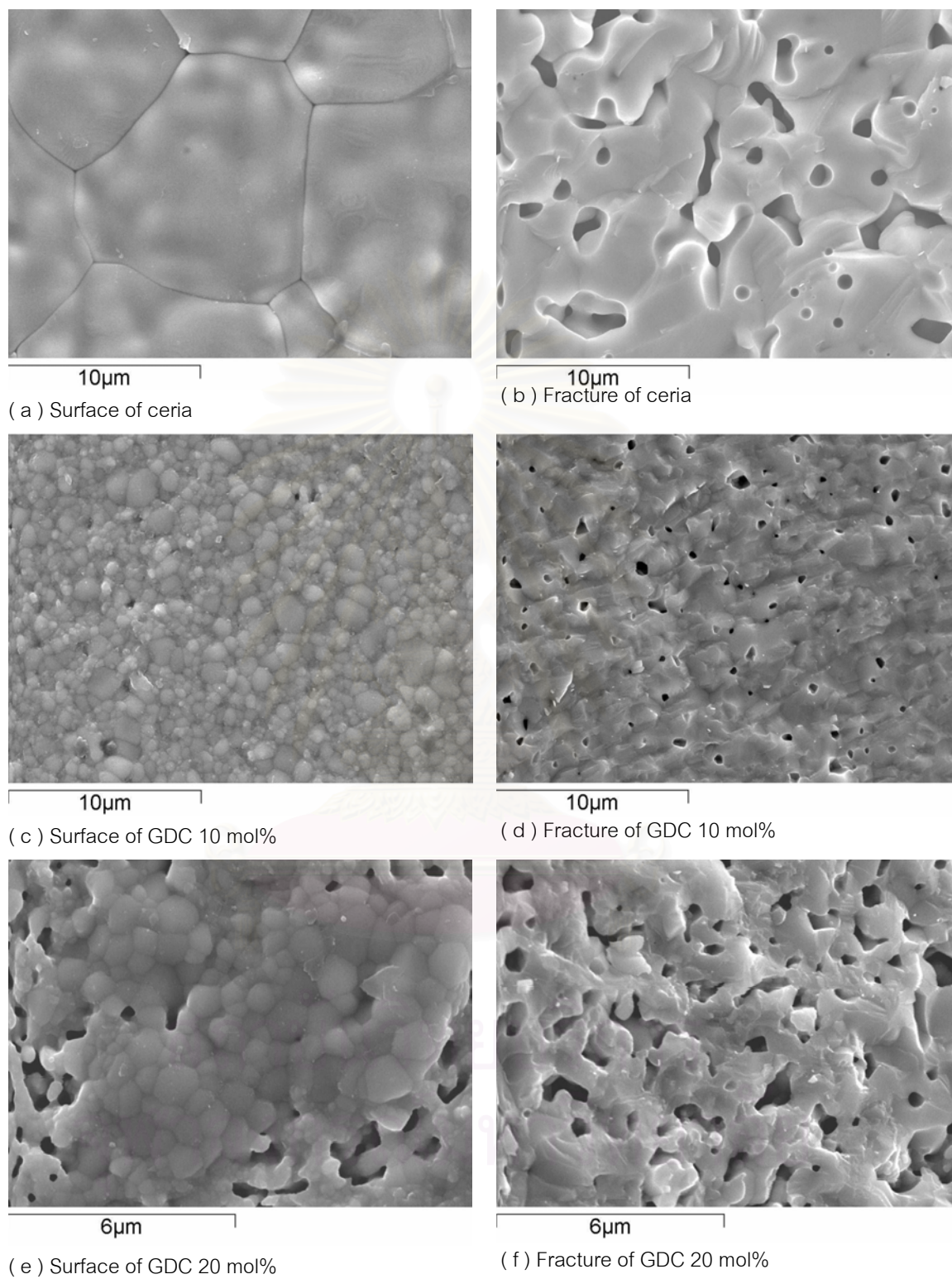


Fig. 4.21 Ceria and GDC with 10 and 20 mol% doped pressed specimens sintered at 1450 $^{\circ}\text{C}$  for 1 hour

Fig. 4.21 illustrated the microstructure of ceria and GDC pressed specimens sintered at 1450°C for 1 hour. For ceria, specimens showed the large grain size of about 10 μm and some porosity at the grain boundaries. The fractured surface had some connected and closed pores which sizes vary between 1.0 to 5.0 μm. For GDC specimens, both 10 mol% and 20 mol% dopant have the smaller grain size than pure ceria. The average grain sizes of GDC samples were in the range of 0.5 to 2.0 μm, however GDC 20 mol% seems to have more porosity than the 10mol% which corresponded to the values measured for the relative density-- 97.58% for GDC 10 mol% and 93.05% for GDC 20 mol%.

Referring to the flow chart in Fig. 3.8 chapter 3, in order to obtain better properties of the electrolyte tapes, the tape-batches with high ionic conductivity were reproduced under varying the sintering conditions in order to study the sintering effects on the total conductivity in the next session. The sintering profiles of the reproduced specimens were 1400°C for 2 hrs, 1450°C for 2 and 4 hrs. Then, the sintered electrolytes were characterized for mineral phase and crystal structure, microstructure evaluation, ionic conductivity measurement, and mechanical property measurement in the same manner as previously done.

Fig. 4.22 showed the SEM micrographs of 3YSZ, MEL (P13R) at different sintering temperatures. The microstructure illustrated the grain sizes of the dense YSZ electrolyte, which increased with increasing sintering temperature and time. The SEM results correspond with the bulk density measurement, shown in Table 4.4. This batch of 3YSZ had more than 99% theoretical density.

More SEM investigation was also performed for all batches of electrolytes prepared in this study as illustrated in Figures 4.23-4.28. The sintering conditions were also 1400°C for 2 hrs, 1450°C for 2 and 4 hours, respectively. From these SEM results, it could summarize that as the sintering temperature increased from 1400°C to 1450°C, most electrolyte samples showed higher density as the porosity was reduced. However, it is evident that some grain growth occurred as the sintering time increased from 2 hrs to 4 hrs at 1450°C. For 10YMEL samples (P20R) in Fig. 4.25, the density measurement at 1450°C for 4 hrs was found to be 97.82% theoretical which is

lower than the one sintered at 1450°C for 2 hrs (97.25% theoretical). It is believed that the longer the sintering time is the bigger the grain growth, and this can be confirmed by SEM images. In addition, similar results and explanations will also be applied to the samples P29 (3YSZ+8YSZ, MEL) as well.

From the SEM study, it can be summarized that the electrolyte batches prepared, including 3YSZ, 8YSZ, and 10YSZ were found to be well-sintered at 1450°C for 2-4 hrs and the microstructures found to be as dense as 98.2-99.7% theoretical density.



สถาบันวิทยบริการ  
จุฬาลงกรณ์มหาวิทยาลัย



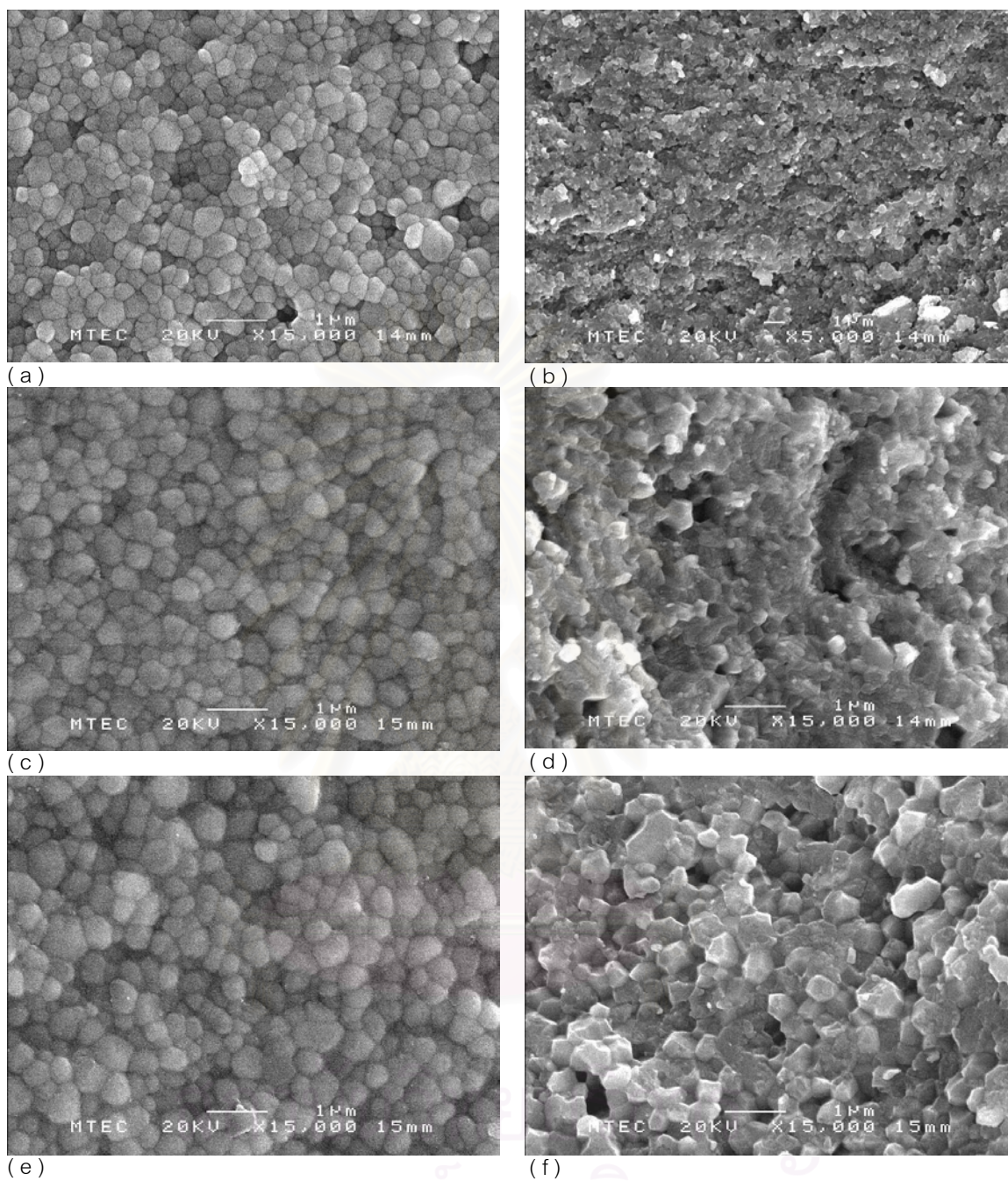


Fig.4.22 SEM micrograph of P13R; 3YSZ (MEL) electrolyte tape ( a ) surface, ( b ) fractured surface sintered at 1400 °C for 2 hrs ; ( c ) surface, ( d ) fractured surface sintered at 1450 °C for 2 hrs ; ( e ) surface, ( f ) fractured surface sintered at 1450 °C for 4 hrs

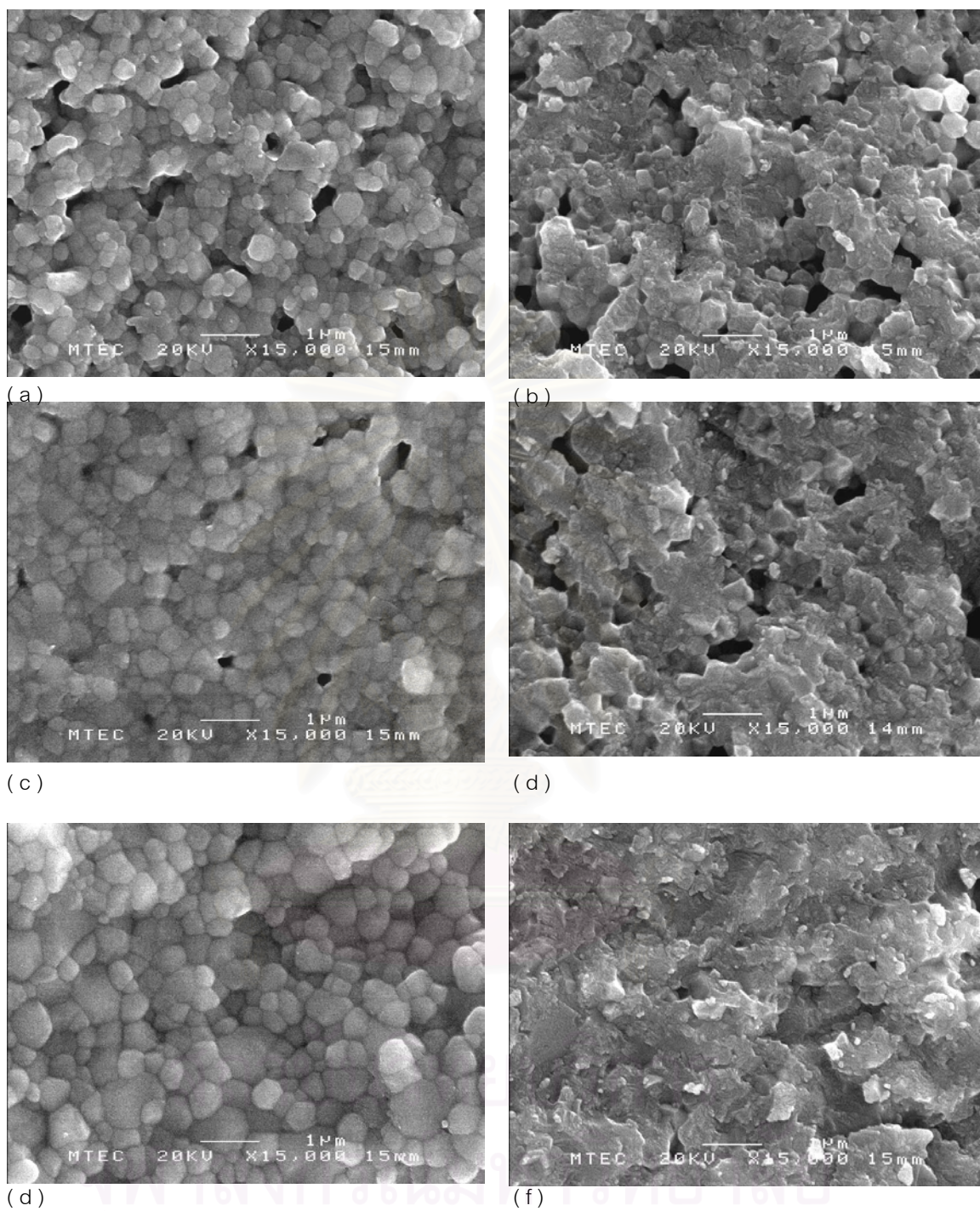


Fig.4.23 SEM micrograph of Po(obtain.commercial.Tape) ; electrolyte tape ( a ) surface, ( b ) fractured surface sintered at 1400 °C for 2 hrs ; ( c ) surface, ( d ) fractured surface sintered at 1450 °C for 2 hrs ; ( e ) surface, ( f ) fractured surface sintered at 1450 °C for 4 hrs



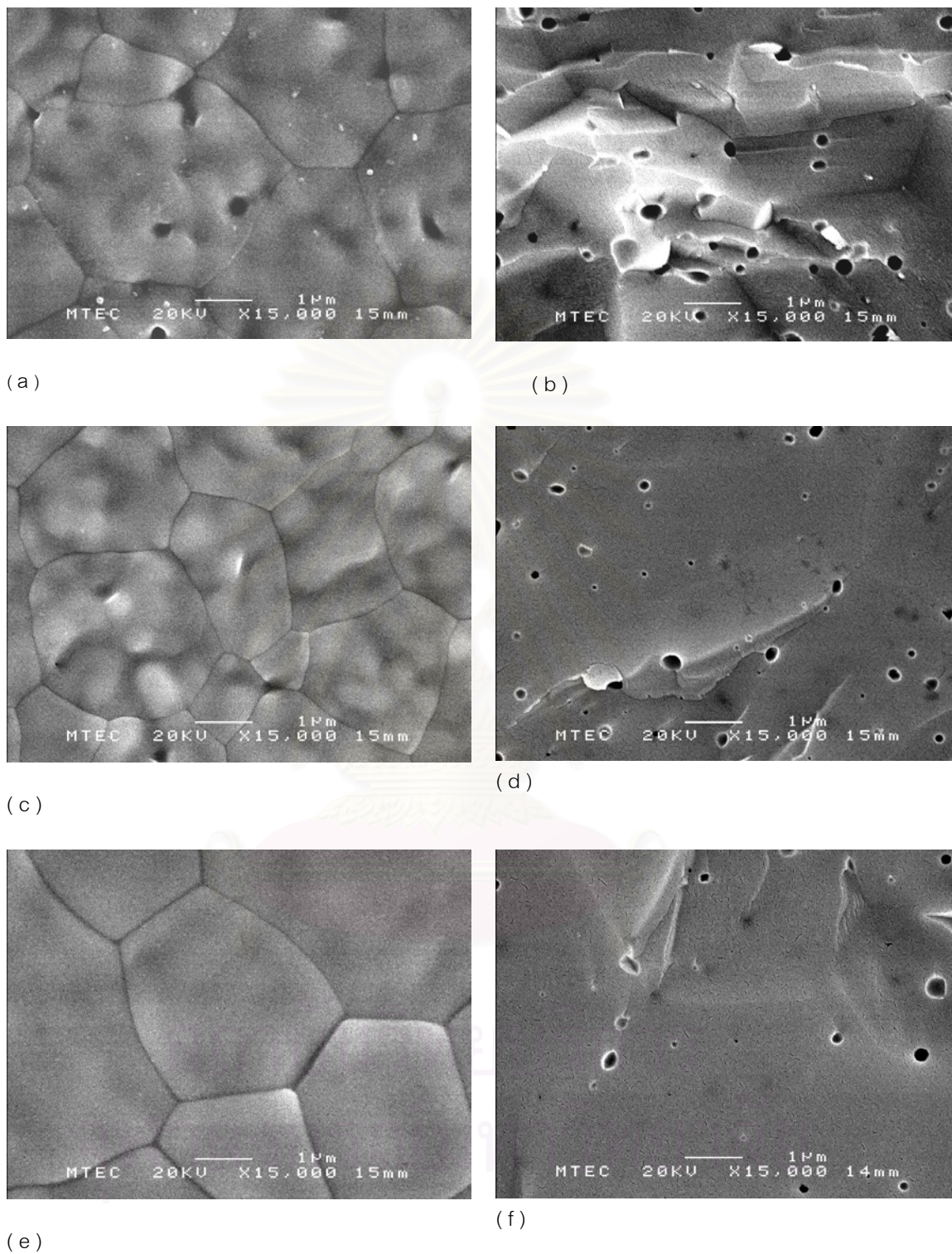


Fig.4.24 SEM micrograph of P19R; 8YSZ (MEL) electrolyte tape ( a ) surface, ( b ) fractured surface sintered at 1400 °C for 2 hrs ; ( c ) surface, ( d ) fractured surface sintered at 1450 °C for 2 hrs ; ( e ) surface, ( f ) fractured surface sintered at 1450 °C for 4 hrs

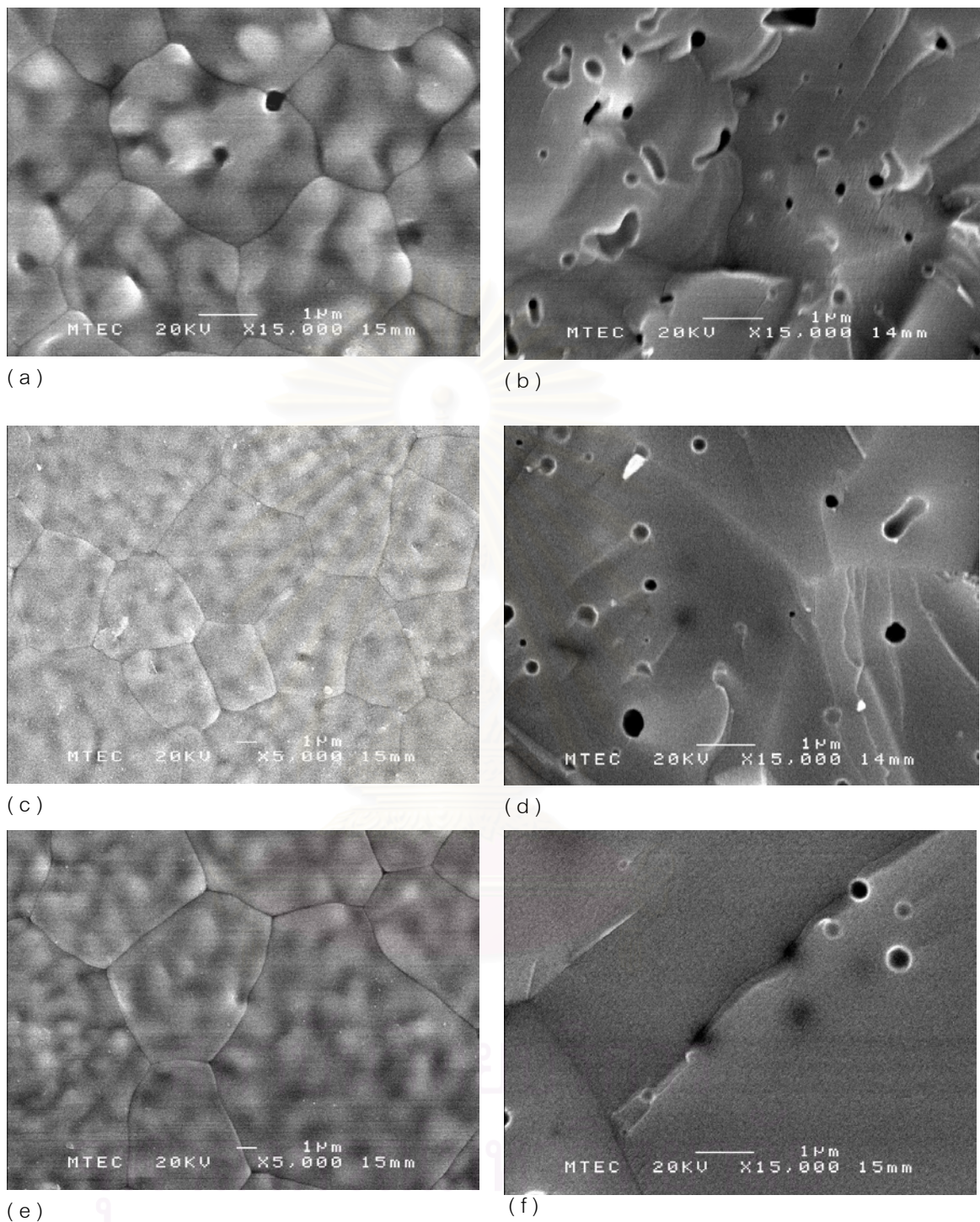


Fig.4.25 SEM micrograph of P20R; 10YSZ (MEL) electrolyte tape ( a ) surface, ( b ) fractured surface sintered at 1400°C for 2 hrs ; ( c ) surface, ( d ) fractured surface sintered at 1450°C for 2 hrs ; ( e ) surface, ( f ) fractured surface sintered at 1450°C for 4 hrs



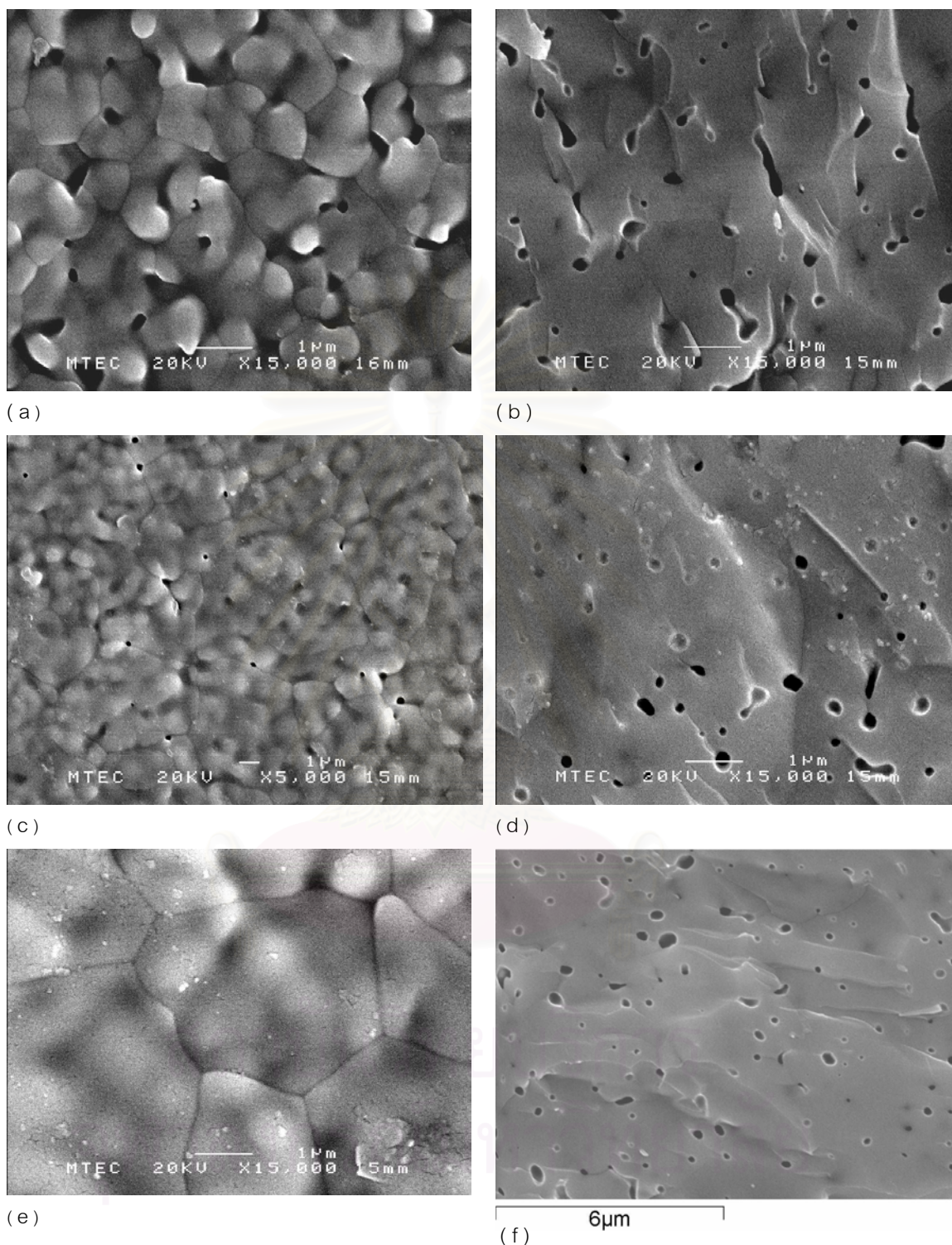
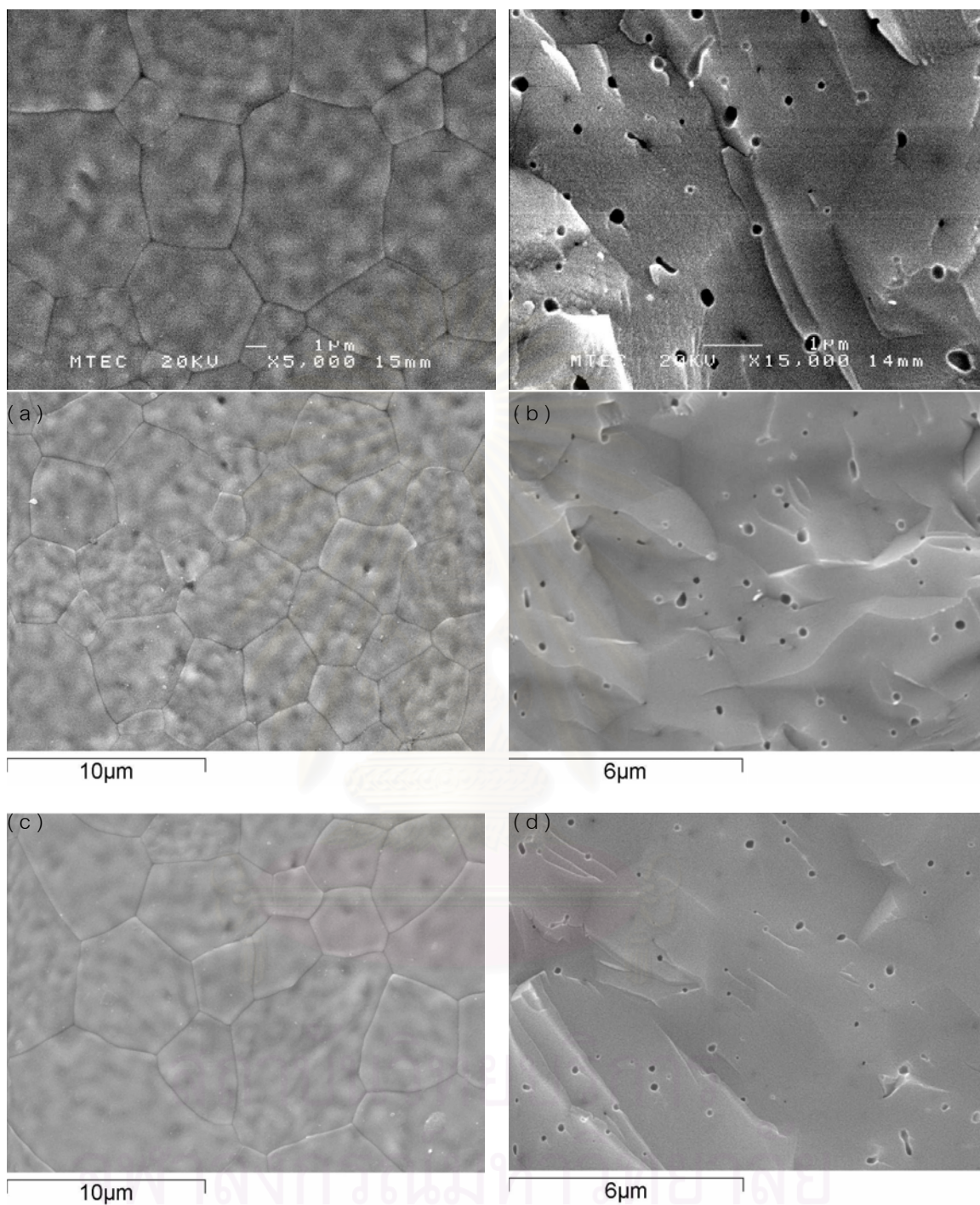


Fig.4.26 SEM micrograph of P9R; 10YSZ (Daiichi) electrolyte tape ( a ) surface, ( b ) fractured surface sintered at 1400 °C for 2 hrs ;( c ) surface, ( d ) fractured surface sintered at 1450 °C for 2 hrs ; ( e ) surface, ( f ) fractured surface sintered at 1450 °C for 4 hrs



(e) (f)  
 Fig.4.27 SEM micrograph of P21R, 8YSZ (Tosoh) electrolyte tape ( a ) surface, ( b ) fractured surface sintered at  $1400^{\circ}\text{C}$  for 2 hrs ;( c ) surface, ( d ) fractured surface sintered at  $1450^{\circ}\text{C}$  for 2 hrs ; ( e ) surface, ( f ) fractured surface sintered at  $1450^{\circ}\text{C}$  for 4 hrs



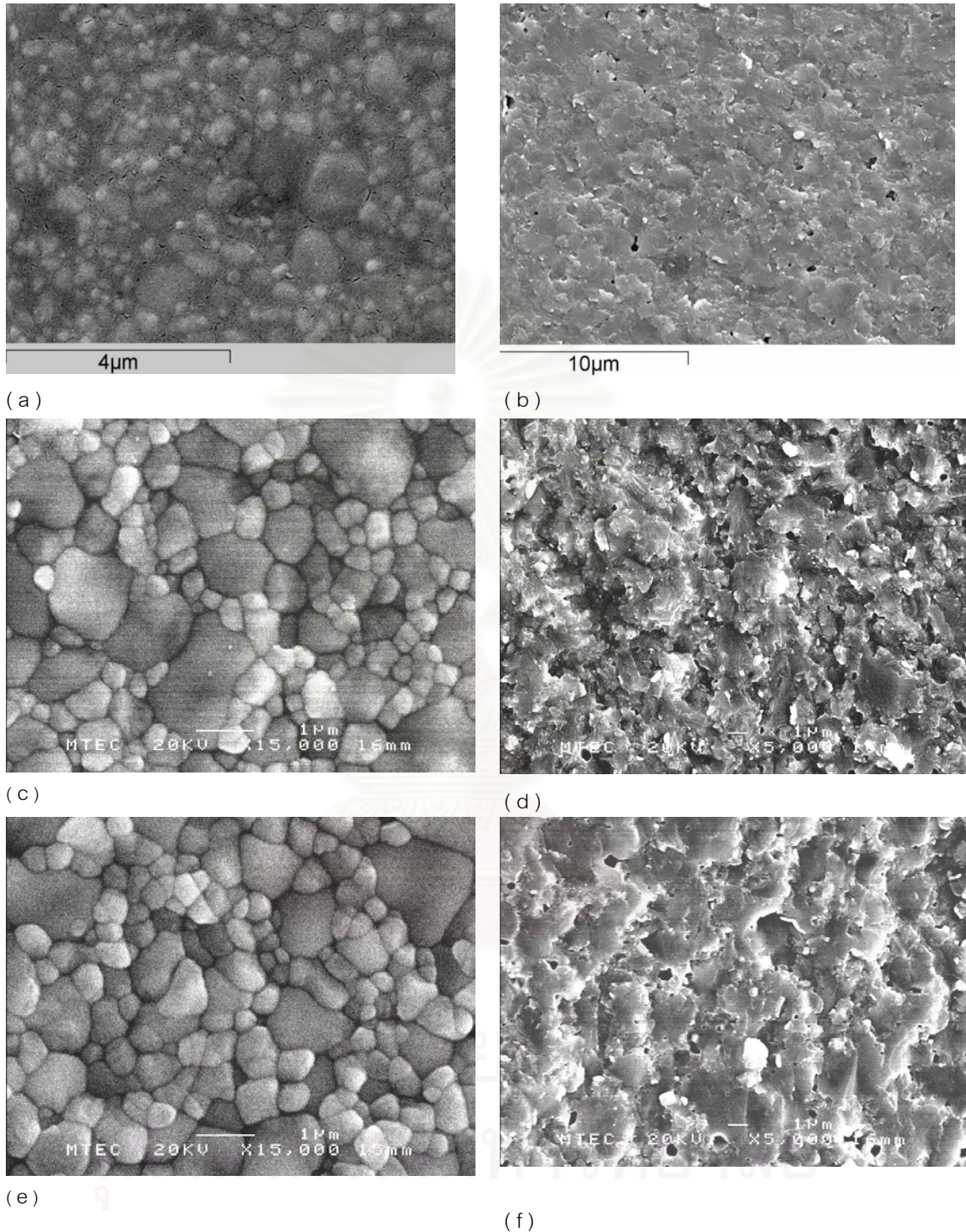


Fig.4.28 SEM micrograph of P29 (3Y+ 8YSZ), MEL electrolyte tape ( a ) surface, ( b ) fractured surface sintered at 1400 °C for 2 hrs ; ( c ) surface, ( d ) fractured surface sintered at 1450 °C for 2 hrs ; ( e ) surface, ( f ) fractured surface sintered at 1450 °C for 4 hrs

The bulk densities and relative densities of electrolyte specimens sintered at different temperatures were measured by Archimedes method shown in Table 4.4.

Table 4.4 The bulk density and the relative density measured by Archimedes method

Batch/ Powder Type	Sintering condition	Density (g/cm <sup>3</sup> )	Relative density (%)
P13R/ 3YSZ (MEL)	1400°C, 2h	5.96	99.42
	1450°C, 2h	5.96	99.42
	1450°C, 4h	5.94	99.00
Po (8YSZ) (Obtained commercial Tape)	1400°C, 2h	5.71	96.77
	1450°C, 2h	5.79	98.28
	1450°C, 4h	5.87	99.49
P19R/ 8YSZ (MEL)	1400°C, 2h	5.76	97.59
	1450°C, 2h	5.80	98.29
	1450°C, 4h	5.85	99.07
P21R/ 8YSZ (Tosoh)	1400°C, 2h	5.82	98.71
	1450°C, 2h	5.79	98.16
	1450°C, 4h	5.86	99.25
P20R/ 10YSZ (MEL)	1400°C, 2h	5.73	96.99
	1450°C, 2h	5.86	99.25
	1450°C, 4h	5.78	97.82
P9R/ 10YSZ (Daiichi)	1400°C, 2h	5.61	95.18
	1450°C, 2h	5.70	96.63
	1450°C, 4h	5.77	97.90
P29/ 3YSZ+ 8YSZ (MEL)	1400°C, 2h	5.89	99.83
	1450°C, 2h	5.87	99.49
	1450°C, 4h	5.88	99.66
P18/ Ceria (tape) Pellet	1400°C, 2h	6.37	88.37
	1450°C, 1h	6.46	89.51
GDC 10mol%, pellet	1450°C, 1h	7.00	97.58
GDC 20mol%, pellet	1450°C, 1h	6.72	93.05

The theoretical density of <sup>[50]</sup> 3 mol%Y <sub>2</sub> O <sub>3</sub> doped ZrO <sub>2</sub> is	6.0	g/cm <sup>3</sup> ,
8 mol%Y <sub>2</sub> O <sub>3</sub> doped ZrO <sub>2</sub>	5.9	g/cm <sup>3</sup> ,
CeO <sub>2</sub>	7.216	g/cm <sup>3</sup>
Ce <sub>0.9</sub> Gd <sub>0.1</sub> O <sub>2-y</sub>	7.173	g/cm <sup>3</sup> ,
Ce <sub>0.8</sub> Gd <sub>0.2</sub> O <sub>2-y</sub>	7.220	g/cm <sup>3</sup>

The relative density is the ratio of the real density to the theoretical density. The data showed that within the measuring temperature, the densities of electrolyte samples increased as the sintering temperature is raised.<sup>[32]</sup> For the electrolyte component of solid oxide fuel cell, the denser, the better.

The higher density means more gas-tight—the enhancement of the electrolyte density by the reduction of the amount and size of pores in it. From Table 4.4 indicated that the density of all zirconia-based electrolyte samples increased with increasing the sintering temperature and times. P13R sample, partially stabilized ZrO<sub>2</sub> (3YSZ, MEL) achieved more than 99% of the theoretical density. For fully stabilized ZrO<sub>2</sub> (8Y and 10Y) samples could obtain ~97% relative density. However, CeO<sub>2</sub>-based materials were difficult to be densified<sup>[16]</sup> by dry-pressing method, therefore their relative density was approximately as low as 93%. From these results, it could be summarized that the density of sintered tapes increased with sintering temperature and times, however, some sintered tape (P13R: 3YMEL) showed the decrease of density at the sintering temperature of 1450°C with increasing time from 2 to 4 hrs. This might be due to the grain growth at longer time soaking, as clearly illustrated in the SEM micrographs (Fig. 4.22)

From the previous study of T.S. Zhang et al.,<sup>[16]</sup> the addition of 1wt.% cobalt oxide led to a nearly fully-dense ceria electrolyte. However, Co-oxide doping has a detrimental result to the total ionic conductivity of the electrolyte. For the electrolyte component, only the dense electrolyte can protect the contact between the fuel gas and oxygen gas and the performance of fuel cell can be improved.

#### 4.4.3 Electrical Property Measurement

The total conductivity of which the major contribution was from the ionic conductivity, of sintered tapes was measured by means of two-probed impedance spectroscopy (Solartron Model SI1260). The sintered specimens were gold-painted and placed into the sample holder in the



tube furnace and the measurements were taken under air atmosphere. The measurements were taken every 25°C interval started at 275°C during the specimens were heated from room temperature to 600°C. Fig.4.23 showed some examples of impedance spectra of electrolyte tape.

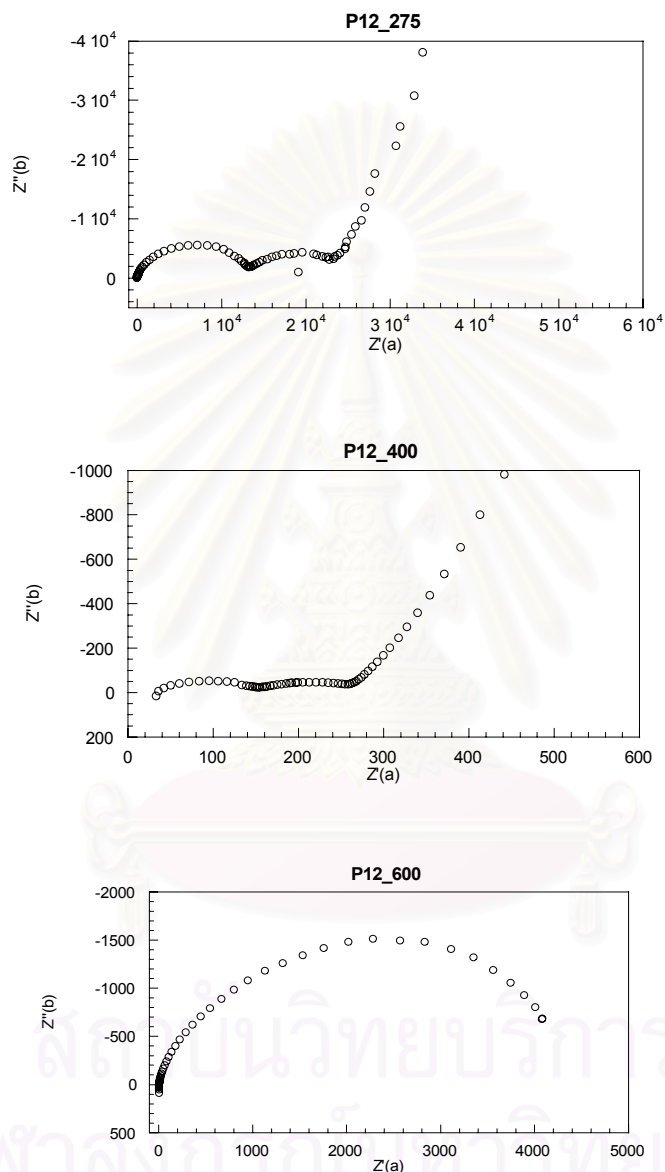


Fig. 4.29 Examples of impedance spectra plots of P12 (10YSZ) electrolyte sintered at 1450°C for 2 hr, recorded at 275°C, 400°C, and 600°C in air. The X-axis represented the imaginary part ( $Z'$ ), and Y-axis represented the real part ( $Z''$ ) of resistance, which units in Ohm

The complex impedance measurements were commonly used to determine the ionic conductivity of stabilized zirconia. An example plot of the imaginary part ( $Z''$ ) versus the real part ( $Z'$ ) for equivalent circuits over a wide range of frequencies resulted in 3 semi-circles as shown in Fig. 4.29. The rest of the complex impedance plots for other electrolyte batches could be found in Appendix B. The high frequency semi-circle (first from left) represented the bulk resistance and capacitance of the interior of the grains; the intermediate frequency semicircle provides the grain boundary resistance and capacitance; and the low frequency semicircle provides the information on the oxygen-ion transfer at the electrodes. In real measurement, the circular arcs rather than semicircles are often observed because the structure of the actual grain boundaries is more complicated than predicted in the equivalent circuit. It should be noted that the influence of grain boundaries on conductivity varies depending on temperature.<sup>[3]</sup> Therefore, the complex impedance plot (number and size of semi-circles) may also vary with temperatures. Previous study reported the conductivity of yttria-doped zirconia, 9YSZ about  $0.14 \text{ S cm}^{-1}$  at  $1000^\circ\text{C}$ .<sup>[47]</sup>

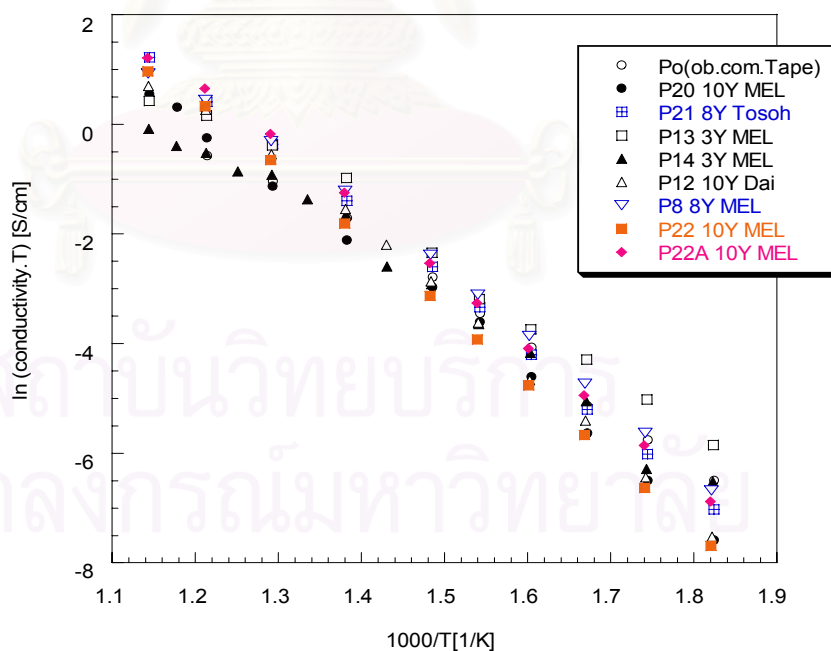


Fig.4.30 The Arrhenius plots of YSZ based electrolyte tapes after sintering at  $1400^\circ\text{C}$  for 2 hrs

The Arrhenius plots in Fig.4.30 showed the ionic conductivity of 3-10 mol% YSZ electrolytes from the various sources of suppliers after sintering at 1400°C for 2 hrs versus temperature in air. The electrolyte samples, 10YSZ MEL(P22A) and 8YSZ Tosoh (P21) had the highest ionic conductivity compared to the others. The values at 600°C were 0.041 S/cm and 0.039 S/cm, respectively. Table 4.5 listed the ionic conductivity and activation energy of YSZ electrolytes at 600°C.

The four best formulations of YSZ electrolyte prepared in this study were chosen to be plotted in Fig. 4.31 in order to emphasize clearly that the batch 10YSZ (MEL) was the one that had the highest ionic conductivity between 450-600°C. However, at lower than 400°C the batch P13 (3YSZ, MEL) seemed to show the better electrical conductivity. Therefore, it can be concluded that if the operating temperature of SOFC stack is at 600°C, the suitable electrolyte system regarding results in this study shall be 10YSZ (MEL), which showed the highest ionic conductivity of about  $4.07 \times 10^{-3}$  S/cm (@ 600°C). The activation energy of 12.20 kJ/mol was calculated for the batch 10YSZ/MEL from the slope of the Arrhenius plot.

Table 4.5 Ionic conductivity and activation energy of YSZ electrolytes at 600°C

Batch / Material Sintered 1400°C / 2hrs	$\sigma_{600^\circ\text{C}}$ [S/cm]	Activation energy, 275-600°C [kJ/mol]
Po (obtain.com.Tape)	$0.68 \times 10^{-3}$	10.19
P13 / 3YSZ, MEL	$1.78 \times 10^{-3}$	9.76
P14 / 3YSZ, MEL	$1.09 \times 10^{-3}$	10.05
P8 / 8YSZ, MEL	$3.03 \times 10^{-3}$	11.40
P20 / 8YSZ, MEL	$1.98 \times 10^{-3}$	11.82
P21 / 8YSZ, Tosoh	$3.97 \times 10^{-3}$	12.25
P22 / 10YSZ, MEL	$3.15 \times 10^{-3}$	12.99
P22A / 10YSZ, MEL	$4.07 \times 10^{-3}$	12.20
P12 / 10YSZ, Daiichi	$2.39 \times 10^{-3}$	12.50

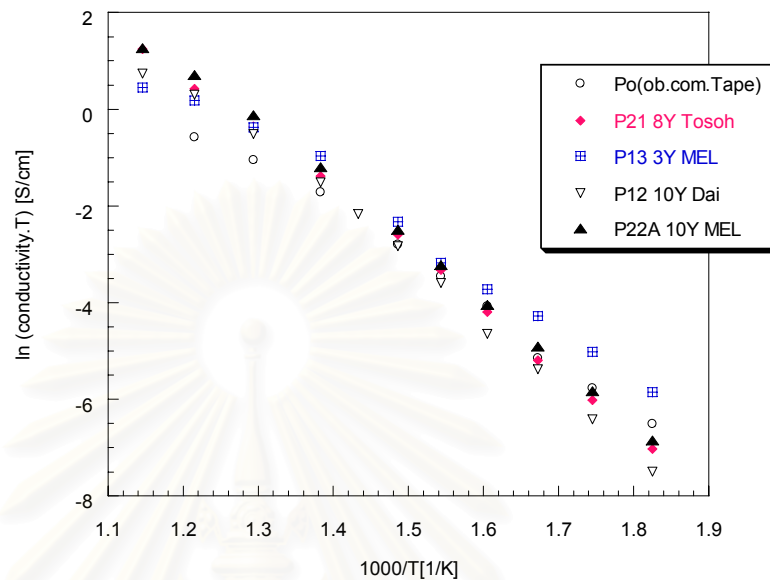


Fig.4.31 The Arrhenius plots of the 4 best formulations of YSZ based electrolyte tapes after sintering at 1400°C for 2 hrs, comparing to the obtained commercial tape.

From this plot, it could be summarized that at the sintering temperature of 1400°C for 2 hour, the tape batch P22A (10Y MEL) showed the highest ionic conductivity at 600°C and over the high temperature range of 450-600°C. At lower than 450°C to 275°C, the 3Y MEL showed the better performance. All batches prepared in this study showed superior ionic conductivity results compared to the obtained commercial tape (Po).

สถาบันวิทยบริการ  
จุฬาลงกรณ์มหาวิทยาลัย

#### 4.4.3.1 Effect of Dopant to Electrical Conductivity

- Effect of Dopant on  $ZrO_2$  Electrolyte System

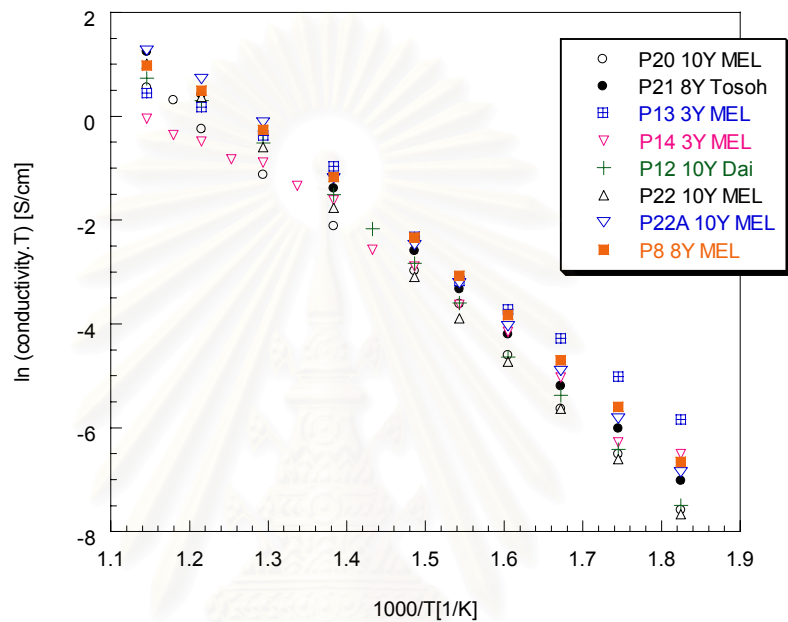


Fig. 4.32 Arrhenius plots of YSZ electrolytes with various mol% of dopants

The purpose of this investigation was to study the influence of the dopant on the ionic conductivity of the electrolyte tapes. The conductivity of  $ZrO_2$  electrolyte tapes doped with 3-10 mol% of  $Y_2O_3$  were measured and Fig. 4.32 showed the ionic conductivity varies with mol% of dopants, i.e. 3YSZ, 8YSZ and 10YSZ. The 10mol% YSZ seemed to have the highest conductivity between 450- 600°C while the conductivity was a little lower than 8YSZ and 3YSZ at lower temperatures (275-450°C).

- Effect of Doping of  $\text{CeO}_2$  system

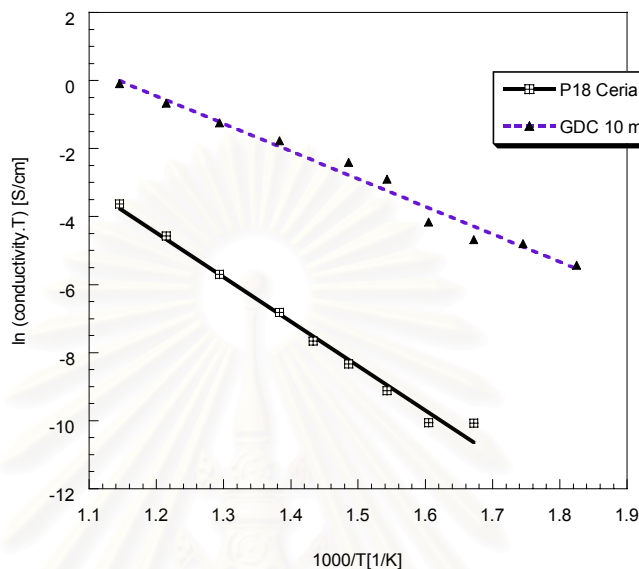


Fig. 4.33 Arrhenius plots of various ceria-based electrolytes in the function of effect of doping

For ceria system, the 10 mol% of  $\text{Gd}_2\text{O}_3$  was doped into ceria as shown in Fig. 4.33. The purpose of study was to explore other system of electrolyte apart from zirconia. The Arrhenius plot clearly showed that 10 mol% of  $\text{Gd}_2\text{O}_3$  or GDC had much higher electrical conductivity than that of pure ceria. In summary, the dopant definitely improves the ionic conductivity of both ceria and YSZ electrolyte systems.

#### 4.4.3.2 Effect of Sintering Conditions on Electrical Conductivity

Previous studies <sup>[32]</sup> reported that at higher sintering temperature the electrolyte specimens were found to have higher density, larger crystal grain sizes, and lower activation energy. This session aimed to verify that statement by varying both sintering temperatures ( $1400^\circ\text{C}$  and  $1450^\circ\text{C}$ ) and time (2 and 4 hrs) as shown in figures 4.34-4.37.

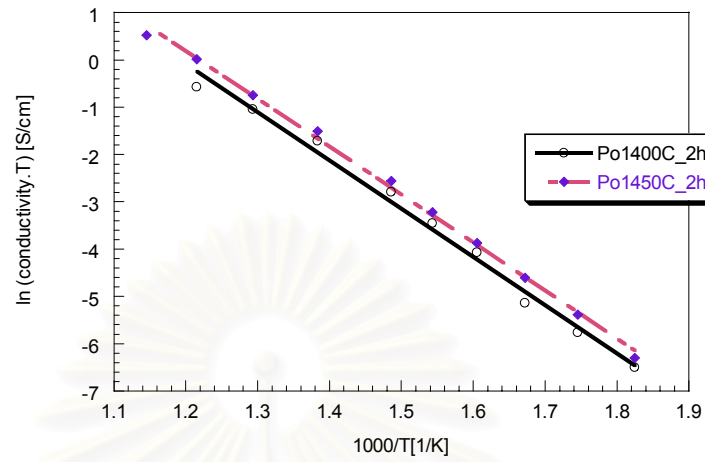


Fig. 4.34 Arrhenius plots of the ionic conductivity for Po (obtain commercial tape) as the function of different sintering temperatures

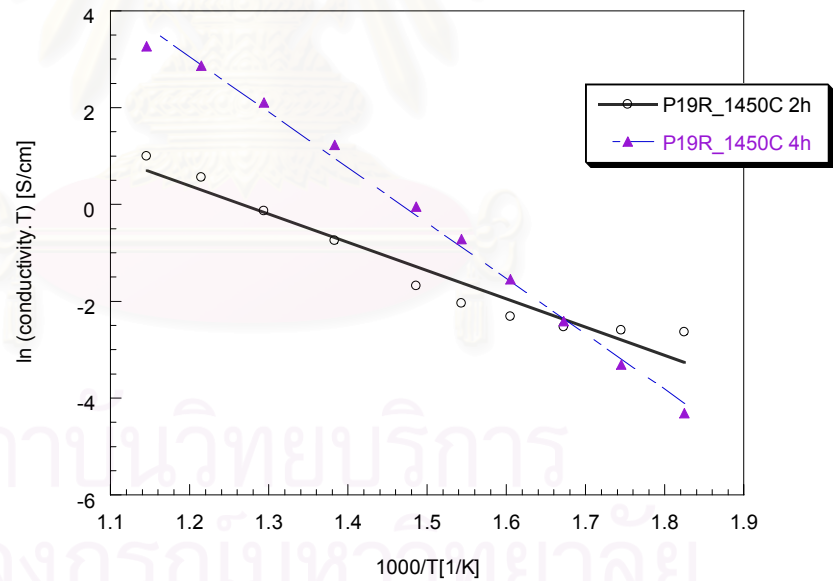


Fig. 4.35 Arrhenius plots of the ionic conductivity for P19R (8Y, MEL) as the function of different sintering time



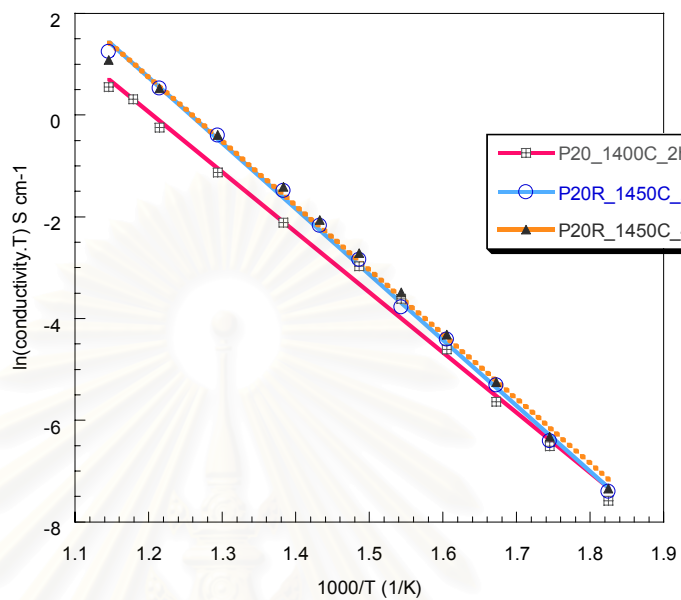


Fig. 4.36 Arrhenius plots of the ionic conductivity for P20R (10Y, MEL) as the function of different sintering temperature and time

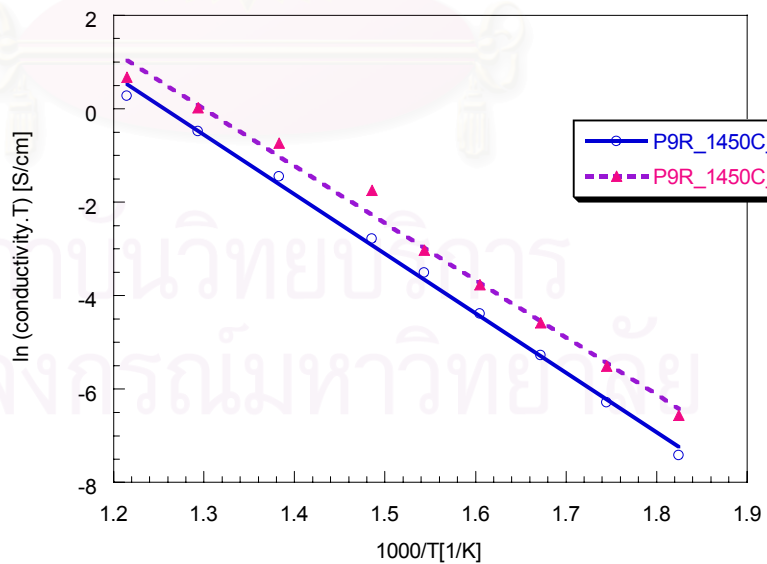


Fig. 4.37 Arrhenius plots of the ionic conductivity for P9R (10Y, Daiichi) as the function of different sintering temperatures

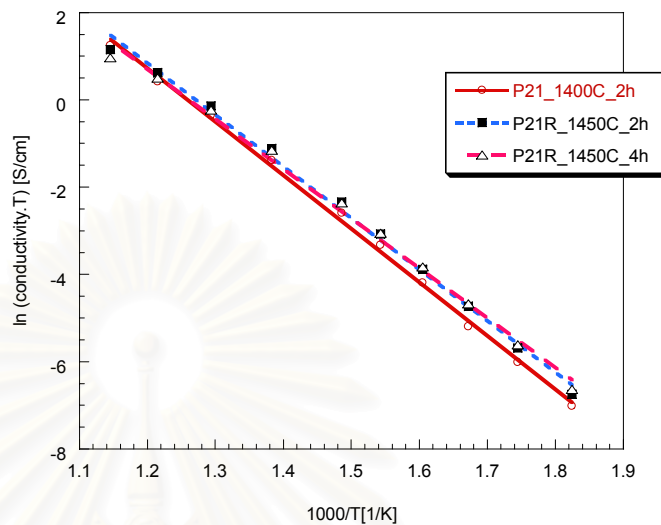


Fig. 4.38 Arrhenius plots of the ionic conductivity for P21R (8YSZ, Tosoh) as the function of different sintering temperature

According to these plots, it seems that higher sintering temperature leads to higher electrical conductivity, which may be due to denser specimens. Apart from the sintering temperatures, the longer sintering time shows the higher electrical conductivity as well.

#### 4.4.4 Mechanical properties Measurement

The mechanical properties of materials for solid oxide fuel cells are increasingly significant, especially for planar design.<sup>[30]</sup> Since many stack configurations are now being scaled up for their long-term reliability. The mechanical property of electrolyte component for SOFC plays a very important role. In this study, a three-point bending strength was measured at room temperature with a cross-head speed of 0.5 mm/ min. The measurement was done only on the sintered electrolyte specimens, which showed the satisfied electrical conductivity results. Table 4.6 listed the flexural strength of reproduced electrolyte batches as the function of different sintering conditions.

Table 4.6 The flexural strength of electrolyte sample at different sintering temperature

Batch	Sintering condition	Average Flexural Strength $\sigma_{avg}$ (MPa)
P13R / 3YSZ (MEL)	1400°C 2h	678
	1450°C 2h	649
	1450°C 4h	378
19R / 8YSZ (MEL)	1400°C 2h	120
	1450°C 2h	88
	1450°C 4h	88
20R / 10YSZ (MEL)	1400°C 2h	184
	1450°C 2h	93
	1450°C 4h	133
P9R / 10YSZ (Daiichi)	1400°C 2h	154
	1450°C 2h	159
	1450°C 4h	94
P29 / 3YSZ+ 8YSZ (MEL)	1400°C 2h	502
	1450°C 2h	233
	1450°C 4h	233
Po(obtain.com.Tape)	1400°C 2h	221

From Table 4.6 shows that the sintering conditions played an important role to the flexural strength of the electrolyte tapes (YSZ materials)— the flexural strength of the specimens trended to decrease with increasing of the temperature and time of firing condition.

The previous study of K. Oe et al.<sup>[35]</sup>, found that the bending strength of 8YSZ, Tosoh, electrolyte increased with the addition of 0.38  $\mu\text{m}$  alumina up to 30 mol%. Therefore, to improve the mechanical property of the electrolyte materials, we may need to consider doping with high strength materials such as TZP (tetragonal zirconia phase).

#### 4.4.5 Thermal Expansion Measurement

A dilatometer (Anter Unitherm Model 1161), at the Department of Science Service, MOST) was used to measure the thermal expansion coefficient of the electrolyte specimens which were 3-10 mol% of  $Y_2O_3$ -doped from Tosoh, Daiichi and MEL. In addition, the ceria-based materials consisted of pure ceria powder from Alfa Aesar, and  $Gd_2O_3$  doped ceria with 10 and 20 mol% by mixed oxide route were also measured. The mismatch of the thermal expansion coefficient of SOFCs components (i.e. electrolyte and electrodes) is one of the usual reasons for incompatibility between solid oxide fuel cell components. The thermal expansion coefficients were measured in the temperature ranges of 50-1000°C at a heating rate of 3°C/min. Table 4.7 showed the average thermal expansion values of the specimens at the temperature of 1000°C. The plots between the thermal expansion coefficients and temperatures in degree Celsius were illustrated in Fig.4.38.

Table 4.7 Thermal expansion coefficients (TEC) of the electrolyte samples at 1000°C

Electrolyte sample	Source	Avg. of TEC, $\times 10^{-6}/^{\circ}C$	Temperature, $^{\circ}C$
3YSZ	MEL, UK.	11.39	1000
8YSZ	MEL, UK.	10.73	1000
8YSZ	Tosoh, Japan	10.68	1000
10YSZ	MEL, UK.	10.67	1000
10YSZ	Daiichi, Japan	10.99	1000
Ceria	Alfa Aesar, USA	12.76	1000
$Ce_{0.9}Gd_{0.1}O_{1.95}$ (GDC-10)	Mixed oxide route	12.93	1000
$Ce_{0.8}Gd_{0.2}O_{1.90}$ (GDC-20)	Mixed oxide route	12.54	1000

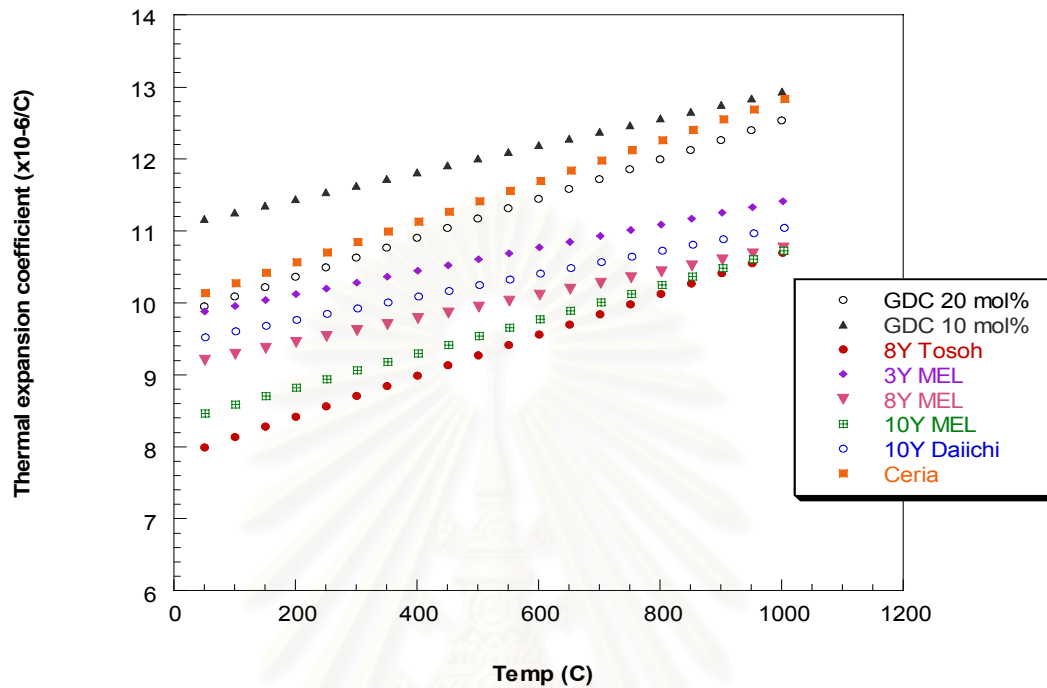


Fig.4.39 Thermal expansion coefficients of SOFC electrolyte materials at the temperature range of 50-1000°C (from various sources)

Fig.4.39 showed the thermal expansion behavior of electrolyte materials for SOFCs. The graphs can be divided into three groups; ceria-based had the highest thermal expansion coefficient (TEC) at 1000°C around  $12.5\text{-}13 \times 10^{-6}/^{\circ}\text{C}$ , 3YSZ tetragonal structure group had TEC about  $11.4 \times 10^{-6}/^{\circ}\text{C}$  and 8 and 10 mol%  $\text{Y}_2\text{O}_3$  stabilized  $\text{ZrO}_2$ , cubic fluorite structure group has TEC around  $10.7\text{-}11 \times 10^{-6}/^{\circ}\text{C}$ . The ceria-based electrolytes exhibited higher thermal expansion coefficients than YSZ by about 15%.

The TEC values for electrode materials<sup>[3]</sup> for SOFCs are reported as the followings:

Anode (NiO/YSZ) TEC  $11.5 \times 10^{-6}/^{\circ}\text{C}$

Cathode (LSM-based) TEC  $11 \times 10^{-6}/^{\circ}\text{C}$

Therefore, it can be concluded that YSZ and ceria systems are appropriate to be used as electrolyte component coupled both regular anode and cathode materials.



## Chapter 5

### Conclusions

From this study the following conclusions can be drawn:

1. The electrolyte system of yttria-stabilized zirconia (YSZ) with varying mol% of  $Y_2O_3$  from 3-10 mol% were chosen to study and successfully fabricate by tape-casting technique. The other systems such as ceria and  $Gd_2O_3$ -doped ceria were also studied in comparison and have the preliminary results.
2. Regarding to the environmentally friendly, the water-based tape casting technique was used to fabricate the SOFC electrolyte and the optimized composition was composed of ceramic powder 62 wt.%, organic binder 18 wt.%, and water 20 wt.%. The average particle size of the YSZ powder suitable for tape-casting fabrication was in the range of 0.3-0.5 microns
3. The optimized sintering temperature and time in order to get the highest electrical conductivity and the highest density (>99.07% of theoretical density for the electrolyte batches was at 1450°C for 4 hours.
4. From the XRD results, the electrolyte specimens both YSZ and ceria systems after sintering at 1400 and 1450°C for 2-4 hrs showed the single phase of cubic for 8-10 mol% YSZ, and tetragonal phase for 3 mol% YSZ. The ceria system also showed the single cubic phase.
5. From SEM results, the grain size and shape showed a uniform and dense microstructure after sintering at 1400 and 1450°C for 2-4 hrs. As the sintering temperature increased, most of the samples have higher density as the porosity reduced, while some batches showed lower density due to the grain growth.

6. The highest electrical conductivity of the electrolyte specimens found to be as high as  $30.11 \times 10^{-3}$  S/cm for 8YSZ (MEL) after sintering at  $1450^{\circ}\text{C}$  for 4 hrs. The activation energy was calculated to be 11.46 kJ/mol.
7. The mechanical property of the sintered electrolyte tape prepared in this study was reported as the flexural strength and the values were in the range of 100-180 MPa for 8-10 mol% YSZ (cubic phase), and 400-680 MPa for 3 mol% YSZ (tetragonal phase).
8. The thermal expansion coefficients of the electrolyte system prepared in this study are reported as the followings: for 8-10 mol% YSZ (cubic) at  $1000^{\circ}\text{C}$   $\sim 10.7\text{-}11 \times 10^{-6}/^{\circ}\text{C}$ , for 3YSZ (tetragonal structure)  $\sim 11.4 \times 10^{-6}/^{\circ}\text{C}$ , and ceria based (cubic fluorite structure), around  $12.5\text{-}13.0 \times 10^{-6}/^{\circ}\text{C}$ .

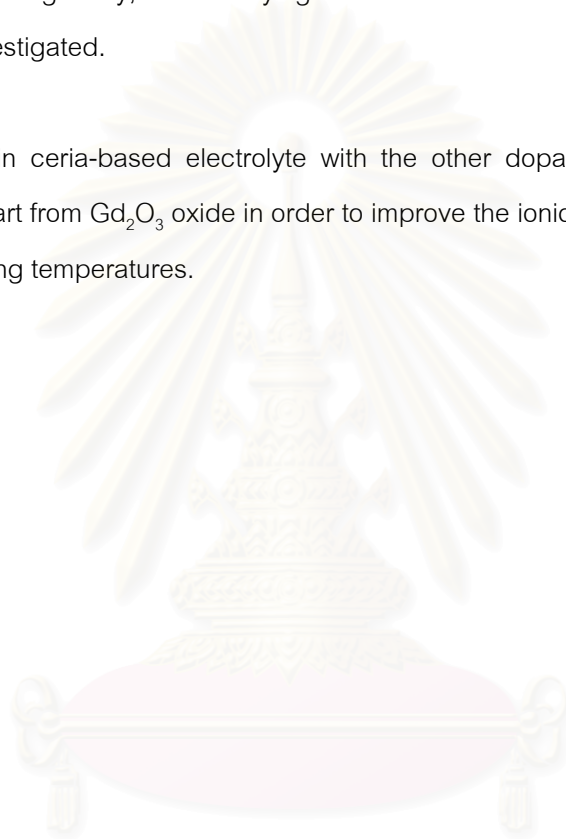


สถาบันวิทยบริการ  
จุฬาลงกรณ์มหาวิทยาลัย

## Chapter 6

### Future work

1. The tape-casting batches for GDC 10-20 mol% should be further studied, since from this study the specimens were prepared by dry-pressing and measure the electrical conductivity. For the tape-casting slurry, more studying and modification of the water-base suspension need to be investigated.
2. Further study in ceria-based electrolyte with the other dopants such as Sm, Sc may be considered apart from  $Gd_2O_3$  oxide in order to improve the ionic conductivity and lowering the SOFCs operating temperatures.



สถาบันวิทยบริการ  
จุฬาลงกรณ์มหาวิทยาลัย

## References

- [1] Singhal, S.C. Advances in solid oxide fuel cell technology. Solid State Ionics 135 (2000): 305-313.
- [2] Minh, N.Q. Ceramic Fuel Cells. J.Am. Ceram. Soc., 76[3] (1993): 563-88.
- [3] Minh, N.Q., Takahashi, T. Science and technology of ceramic fuel cell. Netherlands: Elsevier Science B.V., 1995.
- [4] Tietz, F., Buchkremer, H.P., and Stover, D. Components manufacturing for solid oxide fuel cells. Solid State Ionics 152-153 (2002): 373-381.
- [5] Song, C. Fuel processing for low-temperature and high-temperature fuel cells Challenges, and opportunities for sustainable development in the 21 st century. Catalysis Today 77 (2002): 17-49.
- [6] Stambouli, A.B., and Traversa, E. Solid oxide fuel cells (SOFCs) ; a review of an environmentally clean and efficient source of energy. Renewable and Sustainable Energy Reviews 6 (2002) 433-455. Solid State Ionics 168 (2004): 153-165.
- [7] Geoffrey, A., Tompsett, and Sammes, N.M. Ceria-Yttria-Stabilized Zirconia Composite Ceramic systems for Application as Low-Temperature Electrolyte. J.Am.Ceram.Soc., 80 [12] (1997): 3181-86.
- [8] Haile, S.M. Fuel cell materials and components. Acta Materialia 51 (2003): 5981-6000.
- [9] Singhal, S.C., and Kendall, K. High Temperature Solid Oxide Fuel Cells: Fundamentals, Design and Application. Great Britain: Elsevier., 2003.
- [10] Ivers-Tiffée, E., Weber, A., and Herbstritt, D. Materials and technologies for SOFC-components. Journal of the European Ceramic Society. 21 (2001): 1805-1811.
- [11] Badwal, S.P.S., and Foger, K. Solid Oxide Electrolyte Fuel Cell Review. Ceramics International 22 (1996): 257-265.
- [12] Yamamoto, O. Solid oxide fuel cells : fundamental aspects and prospects. Electrochimica Acta. 45 (2000): 2423-243.
- [13] Wen, T.L., Wang, D., Tu, H.Y., Chen, Z., Lu, Z., Nie, H., and Huang, W. Material research for planar SOFC stack. Solid State Ionics 148 (2002): 513-519.

- [14] Zhu, B. Advantages of intermediate temperature solid oxide fuel cells for tractionary applications. Journal of Power Sources 93 (2001): 82-86.
- [15] Ma, J., Zhang, T.S., Kong, L.B., Hing, P., and Chan, S.H.  $Ce_{0.8}Gd_{0.2}O_{2-\delta}$  ceramics derived from commercial submicron-sized  $CeO_2$  and  $Gd_2O_3$  powders for use as electrolytes in solid oxide fuel cells. Journal of Power Sources 132 (2004): 71-76.
- [16] Sammes, N.M., and Cai, Z. Ionic conductivity of ceria/ yttria stabilized zirconia electrolyte materials. Solid State Ionics 100 (1997): 39-44.
- [17] Skinner S.J., and Kilner, J. A. Oxygen ion conductivity. Materialstoday 30 (2003).
- [18] Tsoga, A., Naoumidis, A., and Stover, D. Total electrical conductivity and defect structure of  $ZrO_2-CeO_2-Y_2O_3-Gd_2O_3$  solid solutions. Solid State Ionics 135 (2000): 403-409.
- [19] Huijsmans, J.P.P., Berkel, F.P.F., and Christie, G.M. Intermediate temperature SOFC – a promise for 21<sup>st</sup> century. Journal of Power Sources 71 (1998): 107-110.
- [20] Zhang, T.S., Ma, J., Chan, S.H., Hing, P., and Kilner, J.A. Intermediate-temperature ionic conductivity of ceria-based solid solutions as a function of gadolinia and silica contents. Solid State Sciences 6 (2004): 565-572.
- [21] Zhu, B., Yang, X.T., Xu, J., Zhu, Z.G., Ji, S.J., Sun, M.T., and Sun, J.C. Innovative low temperature SOFCs and advanced materials. Journal of Power Sources 118 (2003): 47-53.
- [22] Will, J., Mitterdorfer, A., Kleinlogel, C., Perednis, D., and Gauckler, L.J. Fabrication of thin electrolytes for second-generation solid oxide fuel cells. Solid State Ionics 131 (2000): 79-96.
- [23] Mistler, R.E., and Twiname, E.R. Tape casting theory and practice. USA: The American Ceramic Society, 2000.
- [24] Cahn, R.W., Haasen, P., Kramer, E.J. Materials Science and Technology. Weinheim.New York.Basel.Cambridge.Tokyo, 1996.
- [25] Hotza, D., and Greil, P. Review : aqueous tape casting of ceramic powders. Materials Science and Engineering A202 (1995): 206-217.
- [26] Bitterlich, B., Lutz, C., and Roosen, A. Rheological characterization of water-based slurries for the tape casting process. Ceramics international 28 (2002): 675-683.

- [27] Aungkavattana, P. Mixed-conducting oxide electrode for solid oxide fuel cell. Master's Thesis, Department of Materials Science and Engineering, The Graduate School, The Pennsylvania State University, 1992.
- [28] Gibson, I.R., Dransfield, G.P., and Irvine, T.S. Influence of Yttria Concentration upon Electrical Properties and Susceptibility to Aging of Yttria-stabilised Zirconias. Journal of the European Ceramic Society 18 (1998): 661-667.
- [29] Ramanarayanan, T.A., Singhal, S.C., and Wachsman, E.D. High Temperature Ion Conducting Ceramics. The Electrochemical Society Interface (2001).
- [30] Selcuk, A., and Atkinson, A. Strength and Toughness of Tape-Cast Yttria-stabilized Zirconia. J. Am. Ceram. Soc. 83[8] (2000): 2009-35.
- [31] Snijkers, F., Wilde, A., Mullens, S., and Luyten, J. Aqueous tape casting of yttria stabilised zirconia using natural product binder. Journal of the European Ceramic Society 24 (2004): 1107-1110.
- [32] Liu, J., Liu, W., Lu, Z., Pei, L., Jia, L., He, L., and Su, W. Study on the properties of YSZ electrolyte made by plaster casting method and the applications in solid oxide fuel cells. Solid State Ionics 118 (1999): 67-72.
- [33] Zhang, T.S., Ma, J., Kong, L.B., Hing, P., Leng, Y.J., Chan, S.H., and Kilner, J.A. Sinterability and ionic conductivity of coprecipitated  $Ce_{0.8}Gd_{0.2}O_{2-\delta}$  powders treated via a high-energy ball-milling process. Journal of Power Sources 124 (2003): 26-33.
- [34] Moulson, A.J. & Herbert, J.M. Electroceramics. England: Second edition. John Wiley & Sons inc., 2003.
- [35] Oe, K., Kikkawa, K., Kishimoto, A., Nakamura, Y., and Yanagida, H. Toughening of ionic conductive zirconia ceramics utilizing a non-linear effect. Solid State Ionics 91 (1996): 131-136.





Appendices

สถาบันวิทยบริการ  
จุฬาลงกรณ์มหาวิทยาลัย



Appendix A

สถาบันวิทยบริการ  
จุฬาลงกรณ์มหาวิทยาลัย


50-1089		Wavelength= 1.54051				
ZrO2		2 $\theta$	Int	h	k	l
Zirconium Oxide		30.269	100	0	1	1
		34.810	8	0	0	2
		35.254	12	1	1	0
		43.137	1	0	1	2
Rad.: CuK $\alpha$	$\lambda$ : 1.54051	50.375	43	1	1	2
	Filter: Ni	50.709	22	0	2	0
	Beta	59.608	14	0	1	3
	d-sp: Diff.	60.203	24	1	2	1
Cut off:	Int.: Diffract.	62.965	7	2	0	2
	l/lor.:	73.462	3	0	0	4
Ref: Malek, J., Benes, L., Mitsuhashi, T., Powder Diffraction, 12. 96 (1997)		74.535	5	2	2	0
		81.968	11	1	2	3
Sys.: Tetragonal	S.G.: P4 <sub>2</sub> /nmc (137)	82.472	6	0	3	1
a: 3.5984(5)	b:	84.192	4	1	1	4
c: 5.152(1)	A:	84.914	3	2	2	2
C: 1.4317		85.220	3	1	3	0
$\alpha$ :	$\beta$ :	94.711	3	0	2	4
$\gamma$ :	Z: 2	95.473	9	1	3	2
mp:						
Ref: Ibid.						
Dx: 6.134	Dm:					
	SS/FOM: F <sub>18</sub> = 55(.0136 . 24)					


Integrated intensities. An ammonia solution was added to a solution of Zr O Cl<sub>2</sub> to form a gel. The partially dried gel was slowly heated to 600 C under nitrogen, then quenched to room temperature. I-Phase. Tetragonal phase is stable between 1170 C and 2370 C. Pattern taken on metastable phase at room temperature. O2 Zr type. Silicon. Unit cell data determined by Rietveld or profile fit analysis. PSC: UP6. See ICSD 85322 (PDF 88-1007). Mwt: 123.22. Volume[CD]: 66.71.

ICDD . 2003 JCPDS-International Centre for Diffraction Data. All rights reserved  
PCPDFWIN v. 2.4

37-1484		Wavelength= 1.5405981									
ZrO2		2 $\theta$	Int	h	k	l	2 $\theta$	Int	h	k	l
Zirconium Oxide		17.419	3	0	0	1	65.700	6	0	2	3
		24.048	14	1	1	0	65.884	4	1	3	2
		24.441	10	0	1	1	68.912	1	2	3	1
Baddeleyite, syn		28.175	100	1	1	1	69.620	<1	3	2	1
Rad.: CuK $\alpha$	$\lambda$ : 1.540598	31.468	68	1	1	1	70.190	<1	3	2	2
	Filter: Graph Mono	34.160	21	2	0	0	71.071	2	2	2	3
	d-sp: Diff.	34.983	11	0	2	0	71.300	4	4	0	1
Cut off: 17.7	Int.: Diffract.	35.309	13	0	0	2	71.950	1	4	0	0
	l/lor.: 2.6	35.900	2	2	0	1	72.104	1	2	3	2
Ref: McMurdie, H et al., Powder Diffraction, 1. 275 (1986)		38.396	1	[ 2	1	0 ]	72.450	<1	0	4	0
		38.541	4	1	2	0	72.642	<1	3	1	2
Sys.: Monoclinic	S.G.: P2 <sub>1</sub> /a (14)	39.411	<1	0	1	2	73.580	<1	3	1	3
a: 5.3129(4)	b: 5.2125(4)	39.990	<1	2	1	1	74.682	2	0	0	4
c: 5.1471(5)	A: 1.0193	40.725	12	1	1	2	75.046	4	1	4	0
C: 0.9875		41.150	5	2	0	1	76.410	1	1	1	4
$\alpha$ :	$\beta$ : 99.218(8)	41.374	5	1	2	1	77.392	<1	3	3	0
$\gamma$ :	Z: 4	44.826	7	2	1	1	78.079	<1	4	0	1
mp:		45.522	6	2	0	2	78.866	1	0	3	3
Ref: Ibid.		48.949	2	2	1	2					
Dx: 5.817	Dm:	49.266	18	2	2	0					
	SS/FOM: F <sub>30</sub> = 111(.0073 . 37)	50.116	22	0	2	2					
Color: Colorless		50.559	13	2	2	1					
Peak height intensity. The mean temperature of the data collection was 25.5°. Sample was obtained from Titanium Alloy Manufacturing Co. (1990) and was heated to 1300° for 48 hours. CAS #: 1314-23-4. Spectrographic analysis showed that this sample contained less than 0.01% each of Al, Hf and Mg and between 0.1 and 0.01% each of Fe, Si and Ti. Pattern reviewed by Holzer, J., McCarthy, G., North Dakota State Univ., Fargo, North Dakota, USA, ICDD Grant-in-Aid (1990). Agrees well with experimental and calculated patterns. Additional weak reflections [indicated by brackets] were observed. $\sigma(I_{obs}) = \pm 0.01$ . There are a number of polymorphic forms of Zr O <sub>2</sub> stable at different temperatures and pressures. The structure of Zr O <sub>2</sub> (baddeleyite) was determined by McCullough and Trueblood (1) and confirmed by Smith and Newkirk (2). O <sub>2</sub> Zr type. Also called: zirconium dioxide, Baddeleyite, syn, zirkite, zirconia, Zr O <sub>2</sub> . Silver, fluorophlogopite used as an internal stands. PSC: mP12. To replace 13-307 and 36-420 and validated by calculated pattern 24-1165. See ICSD 18190 (PDF 72-1669); 15983 (PDF 72-597); 26488 (PDF 74-815); See ICSD 60903 (PDF 78-50). Mwt: 123.22. Volume[CD]: 140.70.											

ICDD . 2003 JCPDS-International Centre for Diffraction Data. All rights reserved  
PCPDFWIN v. 2.4

30-1468		Wavelength= 1.541780				*
Y0.15Zr0.85O1.93		d(A)	Int	h	k	l
Yttrium Zirconium Oxide		2.968	100	1	1	1
		2.571	25	2	0	0
		1.818	55	2	2	0
		1.550	40	3	1	1
		1.484	6	2	2	2
Rad.: CuK $\alpha$	$\lambda$ : 1.541780	Filter: Graph Mono	d-sp:			
Cut off:	Int.: Diffract.	1/ICor.: 1.70				
		1.285	5	4	0	0
Ref: Pfoertsch, McCarthy, Penn State University, University Park, Pennsylvania, USA, ICDD Grant-in-Aid, (1977)		1.179	10	3	3	1
		1.149	6	4	2	0
		1.049	10	4	2	2
		.9891	6	5	1	1
		.9086	3	4	4	0
Sys.: Cubic		S.G.: Fm $\bar{3}m$ (225)				
a: 5.139(1)	b:	c:	A:	C:		
$\alpha$ :	$\beta$ :	$\gamma$ :	Z: 4	mp:		
Ref: Ibid.						
Dx: 5.959	Dm:	SS/FOM: F $_{11}$ = 60(.0167 , 11)				
Color: Light grayish brown						
Zr O2 + Y2 O3 fired at 1400 C for 6 days with one intermediate regrinding. Composition of common "yttria-stabilized zirconia" solid state electrolyte. Silicon used as an external stand. PSC: cF11.72. Mwt: 121.75. Volume[CD]: 135.72.						
 © 2003 JCPDS-International Centre for Diffraction Data. All rights reserved PCPDFWIN v. 2.4						

82-1246		Wavelength= 1.54060				C
Zr0.8Y0.2O1.9		2 $\theta$	Int	h	k	l
Zirconium Yttrium Oxide		30.046	999*	1	1	1
		34.832	211	2	0	0
		50.084	452	2	2	0
		59.516	289	3	1	1
		62.451	47	2	2	2
Rad.: CuK $\alpha$	$\lambda$ : 1.54060	Filter:	d-sp: Calculated			
Cut off: 17.7	Int.: Calculated	1/ICor.: 9.72				
Ref: Calculated from ICSD using POWD-12++, (1997)		73.540	46	4	0	0
Ref: Yashima, M et al., Acta Crystallogr., Sec. B: Structural Science, 50, 663 (1994)		81.433	86	3	3	1
		84.020	50	4	2	0
Sys.: Cubic		S.G.: Fm $\bar{3}m$ (225)				
a: 5.14728(9)	b:	c:	A:	C:		
$\alpha$ :	$\beta$ :	$\gamma$ :	Z: 4	mp:		
Ref: Ibid.						
Dx: 5.901	Dm:					
Peak height intensity, R-factor: 0.024. Ca F2 type, PSC: cF11.60. Mwt: 121.16. Volume[CD]: 136.37.						
 © 2003 JCPDS-International Centre for Diffraction Data. All rights reserved PCPDFWIN v. 2.4						



82-1241		Wavelength= 1.54060				C
ZrO.9Y0.101.95		2 $\theta$	Int	h	k	l
Zirconium Yttrium Oxide		30.135	999*	1	0	1
		34.719	77	0	0	2
		35.044	134	1	1	0
		43.004	5	1	0	2
		50.159	312	1	1	2
		50.400	178	2	0	0
		53.636	1	2	0	1
		59.420	104	1	0	3
		59.850	200	2	1	1
		62.654	48	2	0	2
		68.363	1	2	1	2
		73.273	15	0	0	4
		74.047	33	2	2	0
		78.629	1	1	0	4
		81.595	61	2	1	3
		81.971	34	3	0	1
		83.885	20	1	1	4
		84.445	18	2	2	2
		84.631	20	3	1	0
		89.647	1	3	0	2

Peak height intensity. R-factor: 0.030. 02 Zr type. PSC: IP5.90. See PDF 82-1243 and PDF 82-1242. Mwt: 122.19. Volume[CD]: 67.60.

 . 2003 JCPDS-International Centre for Diffraction Data. All rights reserved  
PCPDFWIN v. 2.4

34-0394		Wavelength= 1.5405981				*
CeO2		2 $\theta$	Int	h	k	l
Cerium Oxide		28.555	100	1	1	1
		33.082	30	2	0	0
		47.479	52	2	2	0
		56.335	42	3	1	1
		59.087	8	2	2	2
		69.402	8	4	0	0
		76.700	14	3	3	1
		79.070	8	4	2	0
		88.412	14	4	2	2
		95.397	11	5	1	1
		107.265	4	4	4	0
		114.730	13	5	3	1
		117.318	6	6	0	0
		128.393	9	6	2	0
		137.972	6	5	3	3
		141.568	5	6	2	2

Sys.: Cubic S.G.: Fm $\bar{3}$ m (225)  
a: 5.41134(12) b: c: A: C:  
 $\alpha$ :  $\beta$ :  $\gamma$ : Z: 4 mp:  
Ref: Ibid.  
Dx: 7.215 Dm: SS/FOM: F<sub>16</sub> = 130(.0077 . 16)

Color: Light gray, yellowish brown  
Peak height intensity. Pattern taken at 26(1) C. CAS #: 1306-38-3. This yttria stabilized phase was prepared at NBS, Gaithersburg, Maryland, USA, by Drago, Domingues (1982) from co-precipitation of the oxides. The powder was calcined at 620 C and then formed into a billet without binder, isostatically pressed, and then hot-pressed in an alumina die for 30 minutes at 1350 C with an applied stress of 28 MPa. The structure of fluorite was determined by Bragg (1914). Ca F<sub>2</sub> type. Fluorite Group, oxide Subgroup. Also called: ceria. Silver used as an internal stand. PSC: cF12. To replace 4-593. See ICSD 28753, 28785 and 29046 (PDF 75-120, 75-151 and 75-390). Mwt: 172.12. Volume[CD]: 158.46.

 . 2003 JCPDS-International Centre for Diffraction Data. All rights reserved  
PCPDFWIN v. 2.4

43-1002		Wavelength= 1.54056					C
CeO2		2 $\theta$	Int	h	k	l	
Cerium Oxide		28.549	100	1	1	1	
		33.077	27	2	0	0	
		47.483	46	2	2	0	
Cerianite-(Ce), syn		56.342	34	3	1	1	
		59.090	6	2	2	2	
Rad.: CuK $\alpha$ 1	$\lambda$ : 1.54056	Filter: Mono	d-sp: Calculated				
Cut off: 15.0	Int.: Calculated	l/lor.: 13.20					
Ref: Grier, D., McCarthy, G., North Dakota State University, Fargo, North Dakota, USA, ICDD Grant-in-Aid, (1991)		69.416	6	4	0	0	
		76.704	12	3	3	1	
		79.077	7	4	2	0	
		88.428	10	4	2	2	
		95.405	9	5	1	1	
Sys.: Cubic		S.G.: Fm $\bar{3}m$ (225)					
a: 5.41134	b:	c:	A:	C:			
$\alpha$ :	$\beta$ :	$\gamma$ :	Z: 4	mp:			
Ref: Ibid.							
Dx: 7.215	Dm:	SS/FOM: F <sub>10</sub> = 573(.0017 . 10)					

Peak height intensity. Calculation of diffractometer peak intensities done with MICRO-POWD v. 2.2 (D. Smith and K. Smith) using default instrument broadening function (NBS Table), diffracted beam monochromator polarization correction, and atomic scattering factors corrected for anomalous dispersion. Cell parameters from 34-394. Atomic positions from Wyckoff for fluorite structure with Ce in 4a and O in 8c. Isotropic thermal parameters estimated as 1.0 for each atom. Ca F2 type, Fluorite Group, oxide Subgroup. PSC: cf12. See ICSD 61595 (PDF 78-694); See ICSD 72155 (PDF 81-792). Mwt: 172.12. Volume[CD]: 158.46.

 . 2003 JCPDS-International Centre for Diffraction Data. All rights reserved  
PCPDFWIN v. 2.4

75-0161		Wavelength= 1.54060					C
Gd <sub>10</sub> Ce <sub>9001.95</sub>		2 $\theta$	Int	h	k	l	
Gadolinium Cerium Oxide		28.512	999*	1	1	1	
		33.040	279	2	0	0	
		47.423	446	2	2	0	
		56.268	328	3	1	1	
		59.011	60	2	2	2	
Rad.: CuK $\alpha$ 1	$\lambda$ : 1.54060	Filter:	d-sp: Calculated				
Cut off: 17.7	Int.: Calculated	l/lor.: 14.44					
Ref: Calculated from ICSD using POWD-12+, (1997)		69.319	52	4	0	0	
		76.592	103	3	3	1	
Ref: Brauer, G., Gradinger, H., Z. Anorg. Allg. Chem., 276, 209 (1954)		78.962	65	4	2	0	
		88.296	84	4	2	2	
Sys.: Cubic		S.G.: Fm $\bar{3}m$ (225)					
a: 5.418	b:	c:	A:	C:			
$\alpha$ :	$\beta$ :	$\gamma$ :	Z: 4	mp:			
Ref: Ibid.							
Dx: 7.226	Dm:						

Peak height intensity. PSC: cf11.80. No R value given. At least one TF missing. Mwt: 173.03. Volume[CD]: 159.04.

 . 2003 JCPDS-International Centre for Diffraction Data. All rights reserved  
PCPDFWIN v. 2.4



50-0201		Wavelength= 1.54056				
Ce <sub>0.8</sub> Gd <sub>0.2</sub> O <sub>2-x</sub>		2 $\theta$	Int	h	k	l
Cerium Gadolinium Oxide		28.530	72	1	1	1
		33.055	100	2	0	0
		47.425	38	2	2	0
		56.255	49	3	1	1
		58.965	5	2	2	2
Rad.: CuK $\alpha$ $\lambda$ : 1.54056 Filter: d-sp: Diff.		69.300	18	4	0	0
Cut off: Int.: Diffract. I/Corr.:		76.575	8	3	3	1
Ref: Tompsett, G., Sammes, N., Univ. of Waikato, Dept. of Technology, Hamilton, New Zealand, Private Communication, (1998)		78.935	10	4	2	0
		88.239	9	4	2	2
		95.220	14	5	1	1
		107.024	2	4	4	0
Sys.: Cubic S.G.: Fm $\bar{3}$ m (225)		114.430	8	5	3	1
a: 5.4205(1) b: c: A: C:		117.005	5	6	0	0
$\alpha$ : $\beta$ : $\gamma$ : Z: 4 mp:		127.966	8	6	2	0
Ref: Sammes, N., Cai, Z., Solid State Ionics, 100, 39 (1997)		137.459	3	5	3	3
		140.977	4	6	2	2
Dx: Dm: SS/FOM: F <sub>16</sub> = 54(.0185 . 16)						
Color: Brown						
(Ce O <sub>2</sub> ) <sub>0.8</sub> (Gd O <sub>1.5</sub> ) <sub>0.2</sub> was synthesized using a reverse strike coprecipitation technique. Ce (N O <sub>3</sub> ) <sub>3</sub> and Gd (N O <sub>3</sub> ) <sub>3</sub> were dissolved in the correct stoichiometric proportions in distilled water. 0.05M oxalic acid was used as the precipitant and the precipitation reaction was carried out by adding the nitrate solution to the precipitant which was adjusted to pH 6.7-6.9 using ammonia solution. The precipitate was continually stirred at 750 rpm. The precipitate was filtered, washed in triply distilled water and ethanol and dried at 50 C in an oven, followed by calcining at 700 C for 1 hour. The powder was mixed in isopropyl alcohol and milled using yttria stabilized zirconia milling media for 24 hours. The mixed powders were dried and remilled for a further 24 hours. After drying at 50 C for 1 hour, the powder was pressed into pellets at 30 MPa using a uniaxial die press and at 200 MPa using a Standstead FPG2347 isostatic press. The samples were then sintered at 1600 C for 10 hours with a heating and cooling rate of 3 C per minute. Ce <sub>0.8</sub> Gd <sub>0.2</sub> O <sub>2-x</sub> , x indicates that the structure is likely oxygen defective. PSC: cF?. Mwt: 0.00. Volume[CD]: 159.26.						



© 2003 JCPDS-International Centre for Diffraction Data. All rights reserved  
PCPDFWIN v. 2.4

82-1246		Wavelength= 1.54060				
Zr <sub>0.8</sub> Y <sub>0.2</sub> O <sub>1.9</sub>		2 $\theta$	Int	h	k	l
Zirconium Yttrium Oxide		30.046	999*	1	1	1
		34.832	211	2	0	0
		50.084	452	2	2	0
		59.516	289	3	1	1
Rad.: CuK $\alpha$ $\lambda$ : 1.54060 Filter: d-sp: Calculated		62.451	47	2	2	2
Cut off: 17.7 Int.: Calculated I/Corr.: 9.72		73.540	46	4	0	0
Ref: Calculated from ICSD using POWD-12+, (1997)		81.433	86	3	3	1
Ref: Yashima, M et al. Acta Crystallogr., Sec. B: Structural Science, 50, 663 (1994)		84.020	50	4	2	0
Sys.: Cubic S.G.: Fm $\bar{3}$ m (225)						
a: 5.14728(9) b: c: A: C:						
$\alpha$ : $\beta$ : $\gamma$ : Z: 4 mp:						
Ref: Ibid.						
Dx: 5.901 Dm:						
Peak height intensity, R-factor: 0.024, Ca F2 type, PSC: cF11.60, Mwt: 121.16, Volume[CD]: 136.37.						



© 2003 JCPDS-International Centre for Diffraction Data. All rights reserved  
PCPDFWIN v. 2.4

75-0162 Wavelength= 1.54060

Gd.20Ce.8001.90	d(A)	Int	h	k	l
Gadolinium Cerium Oxide	3.1309	999*	1	1	1
	2.7115	283	2	0	0
	1.9173	440	2	2	0
	1.6351	326	3	1	1
	1.5654	60	2	2	2
Rad.: CuKα1 λ: 1.54060 Filter: d-sp: Calculated	1.3557	51	4	0	0
Cut off: 17.7 Int.: Calculated I/Cor.: 14.35	1.2441	103	3	3	1
Ref: Calculated from ICSD using POWD-12++, (1997)	1.2126	64	4	2	0
Ref: Brauer, G., Gradinger, H., Z. Anorg. Allg. Chem., 276, 209 (1954)	1.1069	83	4	2	2

Sys.: Cubic S.G.: Fm $\bar{3}$ m (225)  
 a: 5.423 b: c: A: C:  
 $\alpha$ :  $\beta$ :  $\gamma$ : Z: 4 mp:  
 Ref: Ibid.

Dx: 7.244 Dm:

Peak height intensity. PSC: cF11.60. No R value given. At least one TF missing. Mwt: 173.94. Volume[CD]: 159.48.

 . 2003 JCPDS-International Centre for Diffraction Data. All rights reserved  
 PCPDFWIN v. 2.4

75-0163 Wavelength= 1.54060 C

Gd.30Ce.7001.85	d(A)	Int	h	k	l
Gadolinium Cerium Oxide	3.1338	999*	1	1	1
	2.7140	286	2	0	0
	1.9190	436	2	2	0
	1.6366	322	3	1	1
	1.5669	61	2	2	2
Rad.: CuKα1 λ: 1.54060 Filter: d-sp: Calculated	1.3570	50	4	0	0
Cut off: 17.7 Int.: Calculated I/Cor.: 14.26	1.2452	101	3	3	1
Ref: Calculated from ICSD using POWD-12++, (1997)	1.2137	65	4	2	0
Ref: Brauer, G., Gradinger, H., Z. Anorg. Allg. Chem., 276, 209 (1954)	1.1079	82	4	2	2

Sys.: Cubic S.G.: Fm $\bar{3}$ m (225)  
 a: 5.428 b: c: A: C:  
 $\alpha$ :  $\beta$ :  $\gamma$ : Z: 4 mp:  
 Ref: Ibid.

Dx: 7.262 Dm:

Peak height intensity. PSC: cF11.40. No R value given. At least one TF missing. Mwt: 174.86. Volume[CD]: 159.93.

 . 2003 JCPDS-International Centre for Diffraction Data. All rights reserved  
 PCPDFWIN v. 2.4



Appendix B

สถาบันวิทยบริการ  
จุฬาลงกรณ์มหาวิทยาลัย

Table B-1 Batches and physical appearance of the green tape

Batch/Powder Type	Physical Appearance	%Organic Content
P13/ 3YSZ, MEL	Have small particle on the surface, and small crack at the edge of tape	16.56
P14/ 3YSZ, MEL	Have small particle on the surface	13.45
P17B/ 8YSZ, MEL	Smooth surface and good wetting	13.20
P18/ Ceria	Smooth surface with some crack	13.53
P19/ 8YSZ, MEL	Smooth surface and no crack,	12.51
P20/ 10YSZ, MEL	Smooth surface and good wetting, no crack, no pin-hole	12.90
P20A/ 10YSZ, MEL	Smooth surface and no crack, but not poor wetting	13.07
P21/ 8YSZ, Tosoh	Smooth surface but have a large crack and poor wetting	13.01
P22/ 10YSZ, MEL	Smooth surface and well wetting	13.76
P22A / 10YYSZ, MEL	Smooth surface and well wetting	7.85
P23/ 8YSZ, Tosoh	Not smooth surface, poor wetting and large crack	15.71
P24/ Ceria	Poor wetting and rough surface	12.55
P25/ 10YSZ, MEL	Smooth surface but poor wetting	15.62

สถาบันวิทยบริการ  
จุฬาลงกรณ์มหาวิทยาลัย

## Biography

Miss Patthamaporn Timakul was born in Surathani in November 1976. After graduating with a Bachelor's Degree in Science (Electronic Physics) from the Faculty of Science and Technology, Thammasat University in 2000, she worked as a processing engineer in an IC assembly company for two years. She continued her further study for Master's Degree in the field of Ceramic Technology at Chulalongkorn University in 2002 and graduated in October, 2004.



สถาบันวิทยบริการ  
จุฬาลงกรณ์มหาวิทยาลัย